



Modeling cold cloud processes
with the regional climate model
REMO

Susanne Pfeifer



Hinweis

Die Berichte zur Erdsystemforschung werden vom Max-Planck-Institut für Meteorologie in Hamburg in unregelmäßiger Abfolge herausgegeben.

Sie enthalten wissenschaftliche und technische Beiträge, inklusive Dissertationen.

Die Beiträge geben nicht notwendigerweise die Auffassung des Instituts wieder.

Die "Berichte zur Erdsystemforschung" führen die vorherigen Reihen "Reports" und "Examensarbeiten" weiter.

Notice

The Reports on Earth System Science are published by the Max Planck Institute for Meteorology in Hamburg. They appear in irregular intervals.

They contain scientific and technical contributions, including Ph. D. theses.

The Reports do not necessarily reflect the opinion of the Institute.

The "Reports on Earth System Science" continue the former "Reports" and "Examensarbeiten" of the Max Planck Institute.



Anschrift / Address

Max-Planck-Institut für Meteorologie
Bundesstrasse 53
20146 Hamburg
Deutschland

Tel.: +49-(0)40-4 11 73-0
Fax: +49-(0)40-4 11 73-298
Web: www.mpimet.mpg.de

Layout:

Bettina Diallo, PR & Grafik

Titelfotos:

vorne:

Christian Klepp - Jochem Marotzke - Christian Klepp

hinten:

Clotilde Dubois - Christian Klepp - Katsumasa Tanaka

Modeling cold cloud processes
with the regional climate model
REMO

Dissertation zur Erlangung des Doktorgrades der Naturwissenschaften
im Fachbereich Geowissenschaften der Universität Hamburg
vorgelegt von

Susanne Pfeifer
aus Kassel

Hamburg 2006

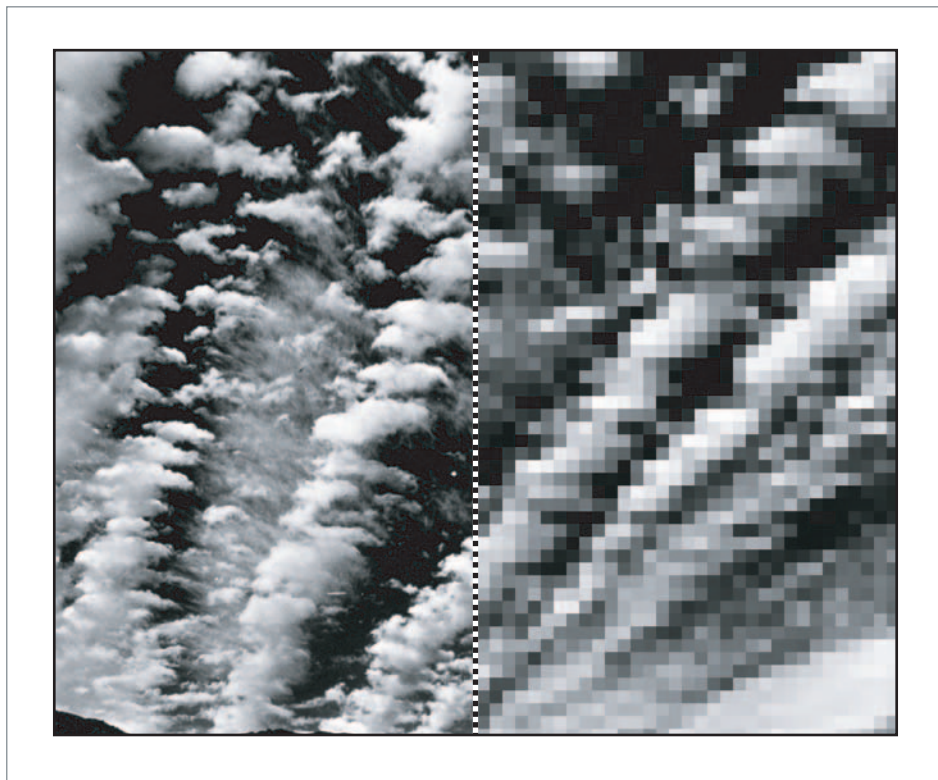
Susanne Pfeifer
Max-Planck-Institut für Meteorologie
Bundesstrasse 53
20146 Hamburg
Germany

Als Dissertation angenommen
vom Fachbereich Geowissenschaften der Universität Hamburg

auf Grund der Gutachten von
Prof. Dr. Hartmut Graßl
und
und Dr. Daniela Jacob

Hamburg, den 13. Januar 2006
Professor Dr. Helmut Schleicher
Dekan des Fachbereiches Geowissenschaften

Modeling cold cloud processes
with the regional climate model **REMO**



Susanne Pfeifer

Hamburg 2006

The picture on the titlepage is based on a photograph taken from the NOAA photo collection, available online (<http://www.photolib.noaa.gov/>). It shows bands of altocumulus clouds with cirrus filaments in the center over the Death Valley, US and was taken in the 1960's by Mr. Willard S. Wood.

Contents

Abstract	3
1 Introduction	7
2 Fundamentals	11
2.1 Clouds in nature	11
2.2 Cloud modeling	14
3 The regional climate model REMO	21
3.1 General characteristics	21
3.2 Clouds in REMO	22
3.2.1 Large-scale cloud scheme	22
3.2.2 Sub-grid scale cloud scheme	28
4 Modifications of the cloud parameterization in REMO	33
4.1 Changes to the large-scale cloud scheme	33
4.2 Changes to the sub-grid scale cloud scheme	43
5 Validation and application of the new cloud scheme	47
5.1 Experimental setup	47
5.2 North Atlantic Cyclone Caroline	50
5.3 Simulation of European climate	57
5.3.1 Liquid water and ice	59
5.3.2 Precipitation	69
5.3.3 Integrated water vapor	77
5.3.4 Total cloud fraction	81

5.3.5	Mean sea level pressure	84
5.3.6	Temperature	87
5.4	Sensitivity studies	92
5.4.1	Influence of driving fields and resolution	92
5.4.2	Sensitivity to changes of the microphysical parameters	98
6	Conclusions	105
7	Outlook	109
	References	111
	List of Abbreviations	119
	Acknowledgments	121

Abstract

The parameterization of clouds in weather prediction and climate models is one of the largest sources for the uncertainty of the simulation results. Improvement of the model's cloud parameterization is therefore a challenging but also promising aspect of model development. The cloud parameterization of the regional climate model REMO has been modified in the following two aspects: Firstly, an improved scheme for the parameterization of large-scale clouds has been adopted from the global model ECHAM5 and implemented into REMO. In contrast to the previous large-scale cloud scheme, prognostic equations are now solved for cloud ice and cloud liquid water separately. Secondly, the parameterization of sub-grid scale clouds in REMO, which is based on the Tiedtke convection scheme, has been extended by introducing a new convection type suited to cover convective events in cold air outbreaks over relatively warm surfaces. The new cloud parameterization has been tested in one multi-year climate simulation for the European region and in a case study of the North Atlantic Cyclone *Caroline*. Main results for the cyclone *Caroline* are a higher percentage of postfrontal precipitation and therefore a better agreement of simulated precipitation rates to precipitation rates derived from SSM/I satellite observations. For the European climate, the inclusion of the modified cloud microphysics resulted in slightly lower winter surface temperatures, less winter cloud cover, a reduction in winter precipitation and an increase in summer precipitation, accompanied by higher intensities of the convective component of the precipitation in summer. Additional changes are occurring in the simulation of cloud phase. The former diagnostic equation for cloud liquid and ice fraction used in REMO produced too much supercooled water at temperatures between $-5\text{ }^{\circ}\text{C}$ and $-25\text{ }^{\circ}\text{C}$. This became evident by comparing simulated values to observations as well as in comparison to diagnostic ice fractions used in other climate models. With the new prognostic treatment of cloud ice and cloud liquid water, the ice fraction is simulated more realistically. The increase in summer precipitation led to a worsening in the simulated precipitation amounts when comparing with precipitation observations from the *Global Precipitation Climatology Centre*. This can be reduced by imposing a lower value of the critical relative humidity, which controls the onset of condensation in the large-scale cloud scheme. Sensitivity studies on the influence

of horizontal grid resolution and on the driving fields have been carried out. In addition, the resolution dependency of the autoconversion rate in large-scale clouds, which is taken into account by applying a resolution dependent tuning factor has been tested for the higher resolution of the regional model.

Zusammenfassung

Die Parametrisierung von Wolken in Wettervorhersage- und Klimamodellen stellt eine der wesentlichen Unsicherheitsquellen in den Modellsimulationen dar. Die Verbesserung der Wolkenprozesse im Modell ist daher ein interessanter und vielversprechender Aspekt der Modellentwicklung. In dieser Arbeit wurde die Parametrisierung von Wolken im regionalen Klimamodell REMO weiterentwickelt: zum Einen wurde eine verbesserte Parametrisierung großskaliger Wolken vom globalen Klimamodell ECHAM5 übernommen und in REMO implementiert. Anders als in der bisherigen Parametrisierung großskaliger Wolken werden nun Wolkenflüssigwasser und Wolkeneis separat durch prognostische Gleichungen berechnet. Zum Anderen wurde das in REMO verwendete Tiedkte Konvektionsschema zur Beschreibung subskaliger Wolken um einen neuen Konvektionstypen erweitert, der eine verbesserte Simulation von Konvektion in Kaltluftausbrüchen ermöglicht. Die neuen Wolkenparametrisierung wurde in einer langjährigen Simulation des europäischen Klimas sowie einer Fallstudie zur Nordatlantischen Zyklone *Caroline* getestet. Für die Zyklone *Caroline* ergab sich eine Zunahme des postfrontalen Niederschlags und damit eine bessere Übereinstimmung des simulierten Niederschlages mit SSM/I Satellitenbeobachtungen. Für das Europäische Klima führten die Änderungen in der Wolkenparametrisierung zu einer leichten Abnahme der Oberflächentemperaturen im Winter, zu einem leichten Rückgang von Bewölkung und Niederschlag im Winter, sowie zu einer leichten Zunahme des Sommerniederschlags, einhergehend mit einer Intensivierung des konvektiven Anteil des Sommerniederschlags. Deutliche Änderungen zeigen sich in der simulierten Wolkenphase. Die ursprünglich in REMO verwendete diagnostische Berechnung von Wolkenflüssigwasser- und Wolkeneisanteil der Wolke führte zu einer Überschätzung des Anteils unterkühlten Wassers bei Temperaturen zwischen $-5\text{ }^{\circ}\text{C}$ und $-25\text{ }^{\circ}\text{C}$. Durch die prognostische Behandlung von sowohl Wolkeneis als auch Wolkenflüssigwasser im Modell kann nun die Wolken-

phase realistischer simuliert werden. Die Zunahme des Sommerniederschlags führte zu einer größeren Abweichung der simulierten Niederschläge von Beobachtungen des *Global Precipitation Climatology Centre*. Diese kann jedoch kompensiert werden durch Anpassung der kritischen relativen Feuchte, die das Einsetzen der Kondensation im Schema für großskalige Wolken kontrolliert. Sensitivitätsstudien wurden zur Abhängigkeit der Wolkenparametrisierungen und speziell der Autokonversionsrate von der horizontalen Gitterauflösung und von der Wahl der antreibenden Felder durchgeführt.

1 Introduction

Clouds play an important role in the climate system. By absorption and scattering, they regulate the amount of incoming solar radiation reaching the earth's surface as well as the amount of thermal radiation leaving our atmosphere. They transport moisture and energy (via latent heat released in the condensation process) vertically (associated with convection and large-scale ascent or subsidence) as well as horizontally, when clouds are advected with atmospheric flow. Through phase changes of the in-cloud water components, they modify temperature and moisture in their environment. Clouds, cloud systems and cloud related processes occur on spatial scales ranging from the microscale (e.g. optical properties of single ice crystals and cloud droplets) to the macroscale (large cloud systems, e.g. North Atlantic Cyclones) and on temporal scales from hours to days. Modeling all this in an appropriate way is a challenging task and *"It is generally recognized that inadequate parameterization of clouds is one of the greatest sources of uncertainty in the prediction of weather and climate"* (GEWEX Cloud System Study (GCSS, [15])).

To improve cloud modeling and to bring together the scientific efforts in this field of work, several projects have been established in the last years, some of them still ongoing. The GEWEX (Global Energy and Water Cycle Experiment) Cloud System Study (GCSS) e.g. focuses on the development of better parameterizations of cloud systems within climate and numerical weather prediction models, having a main focus on climate applications. The activity of the GCSS resulted in various publications and regular meetings. As cloud modeling development is not possible without data from cloud observation, projects are specifically devoted to the improvement and enhancement of cloud observation from space. Most prominent is the International Satellite Cloud Climatology Project, *"which was established in 1982 as part of the World Climate Research Programme (WCRP) to collect weather satellite radiance measurements and to analyze them to infer the global distribution of clouds, their properties, and their diurnal, seasonal and interannual variations"*

(ISCCP, [24]). Validation and improvement of the models is strongly enhanced by the availability of global observational cloud data from satellites.

Huge progress in the representation of clouds in global and regional climate models has been achieved in the last decades, attributed on the one hand to large cooperative projects as those mentioned above, on the other hand also to increasing computer power which made it possible to include computer-time consuming calculations even for long-term climate simulations.

An example for the extensive use of computer power is the inclusion of *cloud resolving models* as cloud parameterizations in global circulation models; an approach which has been suggested under the keyword *superparameterization* by W. Grabowsky in 2001 [17]. New approaches also have been suggested for the parameterization of convection in general circulation models. E.g. Lin and Neelin recently presented their considerations for stochastic convective parameterization (Lin and Neelin, 2002 [38]).

Despite of all achievements, there are still key issues that can be identified as problematic in cloud parameterization. Jakob (2002 [28]) identified amongst others the following processes as being parameterized in "*unsatisfactory*" ways:

- Ice clouds: Ice clouds are important parts of cloud modeling not only because of their strong influence on radiative properties of clouds as well as on the precipitation formation in a given cloud, but also because of the fact that parameterization of ice clouds is limited by the still very little knowledge of their occurrence, their microphysical and radiative effects. Better knowledge of the global distribution of ice clouds hopefully will emerge from satellite data from e.g. CloudSat, which is scheduled for launch in summer 2005 [11].
- Convective clouds: Major problems identified in the context of convective clouds are the representation of microphysical processes in convection and the coupling of the convection parameterizations to the large-scale cloud processes. Following Jakob, those deficiencies are responsible for the fact that largest errors, e.g. in the simulation of net solar radiation at the top of the atmosphere in the ECMWF global model occurred in regions of strongest convective activity.

In this work, the cloud parameterization used in the regional climate model REMO has been modified for the better representation of cold cloud processes. This encompasses on the one hand the inclusion of cloud ice as prognostic variable. In this context, additional cloud microphysical processes concerning phase changes between ice and liquid water in the cloud as well as modifications of precipitation formation in the model have been adopted from the global climate model ECHAM5. On the other hand, the convection scheme in REMO has been extended to allow for the representation of convection in cold air outbreaks associated with extratropical cyclones.

This work is organized as follows: after a short overview of cloud properties and cloud modelling approaches given in chapter 2, the regional climate model REMO is described in chapter 3. This has been done with special focus on the cloud parameterization used in REMO. Chapter 4 explains in detail the changes which were made to the cloud parameterization. The application and validation of the modified REMO model is presented in chapter 5, followed by some concluding remarks in chapter 6 and an outlook given in chapter 7.

2 Fundamentals

2.1 Clouds in nature

Clouds occur on average over 67.5% of the earth's surface (Rossow and Schiffer, 1999 [55]). They cover a spatial range from less than a kilometer to 1000s of kilometers in the horizontal, they mainly form in the troposphere, from the surface to up to 18 km, then penetrating even into the lowest stratosphere (see table 2.1).

Clouds affect the energetics of the atmosphere in several ways: Clouds play an important role in the atmospheric water cycle. They remove water from the atmosphere via precipitation and they influence heat and moisture by the release of latent heat during condensation. The second effect of clouds in the atmosphere is their influence on the atmosphere's radiation budget by scattering, absorption and emission of radiation. In the shortwave spectral range, clouds are important as they directly backscatter solar radiation. This effect is quantified by the cloud albedo defined as the fraction of solar irradiance backscattered. The albedo of an individual cloud is dependent on cloud properties such as cloud liquid water and ice content, cloud droplet sizes and cloud thickness and also on the zenith angle of the sun. Therefore, cloud albedo varies from about 10% up to 90%. In the global average cloud albedo amounts to approximately 20 % of the total incoming radiation (von Storch et al, 1999 [65]). In the longwave, the thermal spectrum of radiation, clouds (except for thin cirrus clouds) are often approximated to absorb and emit radiation like a black body. The characteristic of clouds to re-emit thermal radiation back to the earth's surface and thus trapping the radiation in the troposphere often is referred to as clouds' contribution to the greenhouse effect of the atmosphere.

Clouds form by rising air, which is thereby expanding and cooling. The cooler the air is, the less moisture it can hold so that the rising air eventually reaches its dew-point temperature where condensation starts. The reasons for the lifting of the air can be surface heating as it is the case for convective clouds, topographic barriers as in the

	Range [km]		
Étage	Polar Regions	Temperate Regions	Tropical Regions
High	3-8	5-12	6-18
Middle	2-4	2-7	2-8
Low	0-2	0-2	0-2

Table 2.1: Altitude range of cloud Étages (source: Jacobson, 1999 [27])

case for orographic clouds, or the forced large-scale lifting of air by frontal air masses. Independent of the formation process, clouds form when the rising air reaches the lifting condensation level (LCL). Cloud droplet formation substantially depends on the availability of cloud condensation nuclei, small aerosol particles which allow water vapor to condense on their surface. This process, which is called *heterogenous nucleation* requires a much smaller degree of supersaturation than the *homogenous nucleation*, i.e. the formation of cloud droplets without the help of external particles, and is therefore the dominant way of cloud droplet formation. As moist air is cooled by adiabatic ascent, the relative humidity approaches 100% and hygroscopic aerosol particles begin to serve as condensation nuclei. Supersaturation of the air resulting from further ascent then is depleted by condensation on the nuclei. In this early stage, the dominant growth process of droplets is condensation until they reach the minimum size for other processes to become important. This critical size is given by $r \approx 18\mu\text{m}$ (Rogers and Yau, 1989 [53]). Warm clouds containing only droplets smaller than this are relatively stable with respect to growth by coalescence and will therefore have low probability of rain formation. In clouds with a broader size spectrum of cloud droplets containing also larger droplets, cloud droplets grow mainly by collision and coalescence. Cloud droplets are moving inside the clouds, carried by air currents. When they collide and stick together, this is called the coalescence process. This process is enhanced for larger drops that collect smaller drops when falling through lower layers of the cloud. Cloud droplets that are large enough to overcome drag and updrafts in the cloud finally precipitate. Some typical sizes for the particles included in cloud and precipitation processes are sketched in figure 2.1.

Heterogenous nucleation is also possible for the direct formation of ice crystals. Ice nuclei are however relatively infrequent compared to cloud condensation nuclei. For

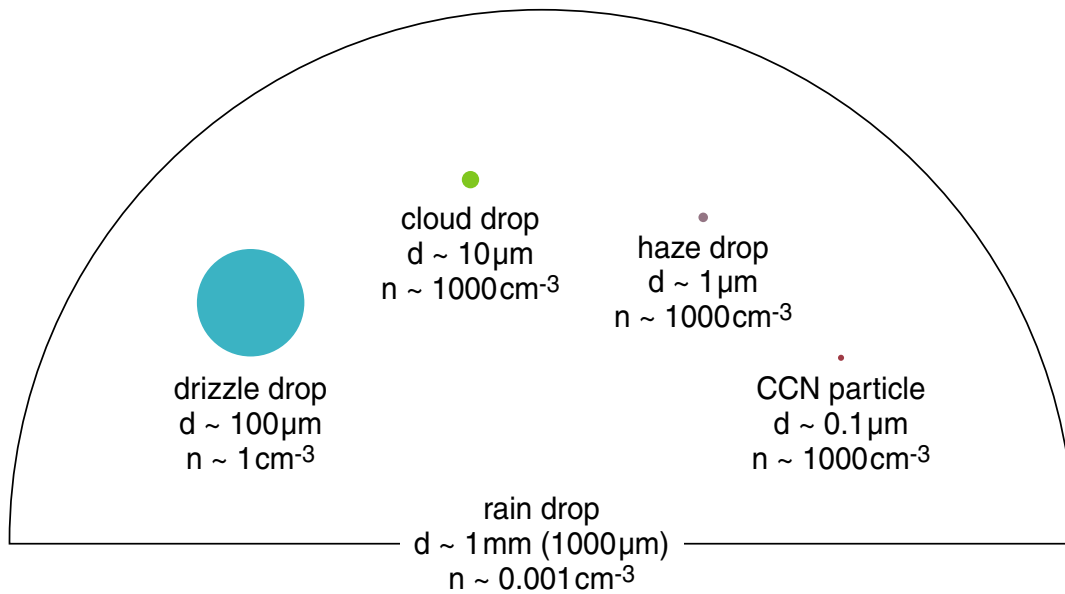


Figure 2.1: Typical sizes of the particles included in cloud and precipitation processes. Diameter d [μm] and number concentration n [cm^{-3}]. Source: <http://www.ems.psu.edu/lno/Meteo437/>

this reason, clouds at temperatures between $-40\text{ }^{\circ}\text{C}$ and $0\text{ }^{\circ}\text{C}$ often consist of supercooled cloud droplets. Only when the temperature drops below approximately $-40\text{ }^{\circ}\text{C}$, the cloud droplets freeze to form ice crystals without the presence of ice nuclei. A glaciation of supercooled cloud droplets at higher temperatures is assumed to occur when they collide with ice nuclei. This process is called *contact freezing*. Once cloud droplets and ice particles coexist in a cloud, the so called *Bergeron-Findeisen* process (see e.g. Stickley, 1940 [64]) becomes important. This process describes the fact that in an environment with cloud droplets and ice crystals, the ice crystals grow at the expense of the cloud droplets, because the supersaturation needed to condense water vapor on the surface of an ice crystal is lower than the supersaturation which is needed to condense water vapor on a liquid cloud droplet. In this way, the cloud air might be undersaturated with respect to water whereas at the same time, the moisture inside the cloud exceeds saturation with respect to ice. As a result, ice crystals grow, while the supercooled liquid water droplets evaporate.

One hypothesis to explain the multiplication of ice crystals (i.e. the existence of more ice crystals than ice nuclei) in clouds is the *Hallet-Mossop* process, which

states that a rime-splintering of ice crystals leads to the production of secondary ice (see e.g. Pruppacher and Klett, 1997 [47]).

Cloud droplet sizes vary from a few micrometers to more than $100\mu m$ (0,1 mm) for the larger ones, with average diameters usually around $10\mu m$. Typical cloud droplet concentrations are in the order of several hundred droplets per cubic centimeter (Rogers and Yau, 1989 [53]). Continental clouds tend to have smaller droplets with higher droplet concentrations, whereas marine clouds are characterized by bigger droplets and smaller droplet numbers. The reason lies in the larger amount of aerosols that can act as condensation nuclei in the continental airmasses compared to the maritime airmasses with less cloud condensation nuclei (see e.g. Schwarz, 1996 [61]).

2.2 Cloud modeling

The adequate representation of clouds and cloud affecting processes in an atmospheric (climate) model is a challenging task. The variety of models of different complexity and the numerous applications also of different complexity give reason to the question of how precise the models have to be, which processes are indispensable and which can be omitted for special applications without loss of accuracy.

An important limitation of the cloud parameterization of a given climate model is the model's horizontal and vertical grid resolution: Clouds in the order of magnitude of the model's grid scale can explicitly be resolved by the model. The effects of subgrid-scale processes are unresolved and have to be parameterized. Global as well as regional climate models (with horizontal grid spacings in the range of 10 to 500 km) parameterize the effects of convection and cloud microphysics as well as the radiative properties of clouds. Their cloud schemes are usually divided into two parts: the *large-scale* cloud scheme which accounts for cloud processes on scales larger than the model resolution and the *sub-grid scale* cloud scheme (*convection scheme*) for unresolvable processes that have to be parameterized. The large-scale cloud scheme simulates clouds explicitly on the grid scale and represents basically the removal of supersaturation on grid scales. Sub-grid scale or convection schemes account for clouds even though grid scale saturation is not reached. This implicit cloud treatment differs from the explicit cloud mode by the fact that the properties

of sub-grid scale clouds differ from the properties of the grid box they are located in while for explicit clouds, the properties of the cloud and the grid variables are similar. Nevertheless, sub-grid scale clouds depend on the ambient conditions and exert influence on their surrounding and must therefore be related to the grid scale variables. This is usually done in the following three steps:

1. Triggering, that means the activation of the convection scheme: Convective instability is usually determined by lifting an air parcel dry-adiabatically until it reaches the lifting condensation level. If it is still positively buoyant with respect to its surrounding, convection is activated.
2. Determining the strength of the convection depending on the large scale variables: This is called the *closure* problem. Closure assumptions can be based on either the adjustment of the profiles of temperature and moisture in convectively unstable layers to prescribed reference profiles, on moisture budgets that have to be in equilibrium or e.g. on the convective available potential energy CAPE, which has to be removed by convection.
3. Assessing the influence of convection on the surrounding air: Convection influences the environment by transporting heat and moisture vertically, by mixing of cloud air with environmental air (entrainment and detrainment processes) and by the release of precipitation. Those processes are expressed by cloud models belonging to the convection scheme.

These sub-grid scale cloud schemes can be omitted only when the grid resolution is fine enough to resolve single convective clouds. The resolution needed is vividly discussed, the upper limit is however a resolution of at least 2 km to explicitly resolve convection (e.g. Molinari and Dudek, 1991 [39]). With increasing resolution, parts of the convective motions are explicitly solved by model dynamics, whereas other parts still have to be parameterized so that for regional climate models, convection schemes different from those currently used in global models have been formulated. Molinari and Dudek (1991 [39]) proposed to use the implicit approach for convection (i.e. traditional convection schemes as in use in global models) only for model resolutions coarser than 50 km. They suggested the use of the fully explicit approach (i.e. no separate sub-grid scale cloud scheme) only for grid spacings below

3 km and a *hybrid* approach for all resolutions between 20 and 50 km. The hybrid approach is mainly characterized by including convective source terms in grid scale prediction equations for cloud water, cloud ice, rain water and so on. In their paper, they stated that for the range of horizontal resolutions between 3 km and 20 km "*it remains uncertain whether a general solution exists*". Unlike Molinari and Dudek, Hammerstrand (1998 [21]) concluded that traditional convection schemes designed for model resolutions of around 100 km can also be used without loss of accuracy when the model resolution is 10 to 20 km.

To overcome the problems of convection parameterization and to allow for explicit representation of small-scale clouds even in models with coarse grid resolution, a new approach to enhance cloud parameterization in Global Circulation Models has recently been developed: the so called superparameterization, which has first been suggested by Wojciech Grabowski (2001 [17]). The idea is to include *Cloud System Resolving Models* as cloud parameterizations inside the GCM grid boxes. Main benefit of this approach is that it becomes possible to explicitly simulate e.g. deep convection, fractional cloudiness (down to a scale of a few kilometers), spatial distribution of precipitation intensities and so on. This approach is however limited by the increasing computational costs. Running a GCM with this superparameterization increases the computational costs by a factor of 10^2 to 10^3 (Randall et al., 2003 [48]), which is not acceptable for most applications despite increasing computer power. The *Cloud System Resolving Models* (CSRMs) are 2D or 3D models that resolve cloud scale motions. Used as stand-alone model, they usually have horizontal resolutions of at least about 2 km. Horizontal domain sizes are chosen according to the subject of interest. The investigation of a convective cloud system, containing both cumulus scale and mesoscale circulations, would require domain sizes with side lengths of about 400 km, whereas the simulation of a single convective cell may require a domain size of only 5 to 10 km with a grid spacing of only meters to a few tens of meters (Krueger, 2000 [33]). Models on such scales then are called *Cloud Resolving Models* (CRMs) or just *Cloud Models* (CMs). In CSRMs and CRMs, phenomena smaller than the resolved scale (such as turbulence) still have to be parameterized, whereas effects of scales larger than the respective domain size have to be specified as large scale forcing of the simulated processes. As it is the case for all limited area models, possible inaccuracies of the large scale forcing may

significantly affect CSRM and CRM results.

Depending on the question of interest, a model can be set up with different levels of complexity and specialization. Simulations of long-term climate for example may require a scheme that reliably produces regional mean values of precipitation, cloud cover and cloud liquid water without needing the full complex cloud microphysics, which would in addition make the model more expensive in terms of computer time needed to do the calculations. Model studies of local convective systems might however be essentially dependent on the correct representation of every hydrometeor species and its interactions with the environment.

In terms of microphysics, the "cloud parameterization hierarchy", which agrees rather well with the "computer time cost hierarchy", ranges from one-moment bulk schemes over two-moment bulk schemes to bin schemes. Each of these schemes can additionally consider different numbers of hydrometeor species (liquid water, ice, rain, snow, hail, graupel, etc.). One-moment bulk schemes calculate changes only in the mixing ratios of the considered hydrometeor species. In the case of two-moment bulk schemes, in addition to the mixing ratios, number concentrations of the hydrometeor species are computed, without allowing changes in the shape of the size distribution of the hydrometeors, which - in case of cloud droplets - mostly is assumed to follow either log-normal or gamma distributions. The bulk approach for the number concentration of any hydrometeor is illustrated schematically in figure 2.2. Shown is the number concentration of the hydrometeor species versus the diameter of the hydrometeors. The *bulk* approach uses an analytical function (blue line) to fit the observed distribution (red curve). Changes of the distribution are approximated by computing parameter changes in the analytical function. The *bin* approach separates the size distribution of the hydrometeors into a number of size classes, the bins. Changes of the number concentration of the hydrometeor spectrum are then computed by estimating the change of the number of particles in each bin. This approach is sketched in figure 2.3.

By incorporating more hydrometeor species, an increasing number of cloud microphysical processes can be considered in the cloud parameterizations. Phase changes between the in-cloud water components require e.g. cloud ice and cloud liquid water to be considered. The different characteristics of e.g. maritime and continental clouds resulting from the unequal availability of aerosols which can serve as cloud

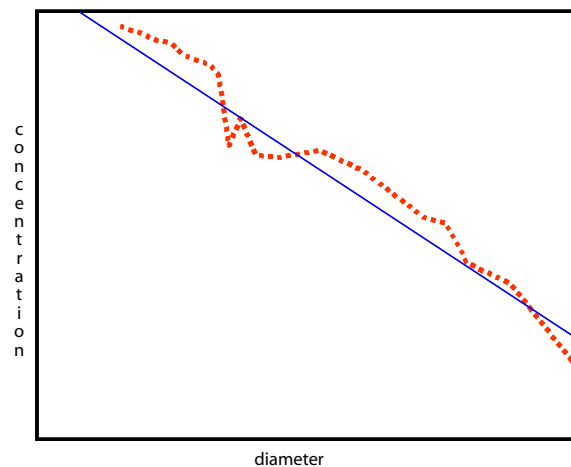


Figure 2.2: schematical illustration of the bulk approach. Red curve: size distribution of a hydrometeor species, blue line: analytical function to fit the distribution

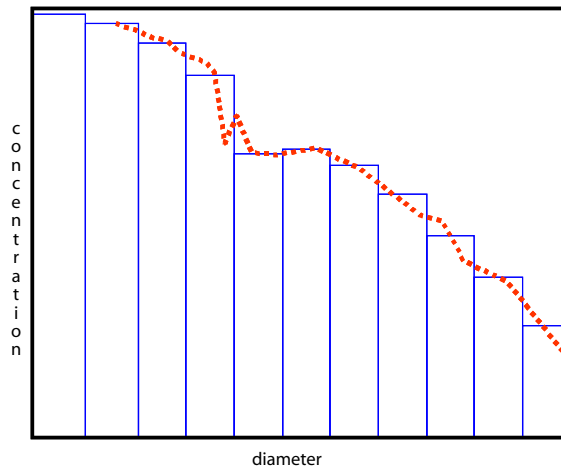


Figure 2.3: As figure 2.2 but for the bin approach. Red curve: size distribution of a hydrometeor species, rectangles: sub-classes (bins)

condensation nuclei can only be captured by a cloud microphysical parameterization including number concentrations of cloud droplets. The formation of precipitation, which for a given liquid water mixing ratio strongly depends on the size and number concentration of the cloud droplets, can thus be described in more detail by the use of a two-moment bulk scheme or a bin scheme. The evolution of the cloud droplet spectrum from the activation of cloud condensation nuclei through the onset of cloud droplets by condensation to the self collection by large drops can best be described by the use of a bin microphysical scheme.

A *scale problem* arises also in the context of the parameterized cloud microphysics. As mentioned above, parameterization of cloud microphysics is necessary on all model scales currently used in climate simulation. Huge efforts have been made during the last years to give parameterizations of cloud microphysics a more physical basis by the use of cloud resolving models, by the evaluation of data gained at extensive measurement campaigns and by the analysis of artificial clouds in cloud chambers. Equations governing processes as coalescence of cloud droplets, collision of cloud droplets, freezing processes and so on that have been achieved in this way are then applied in models on different scales. This raises the question if it is possible to upscale those small-scale processes (which are formulated on a grid fine enough to

resolve one single cloud into multiple vertical layers and into multiple in-cloud grid boxes) to the particular grid resolution (which could be as coarse as having a whole cloud inside one grid box). It is subject of discussion, whether the general assumptions (concerning e.g. the probability of collision of single cloud droplets) underlying the process formulations developed on the *grid-in-the-cloud* scale are still valid for application on the *cloud-in-the grid* scale (e.g. Brenguier, 2005 [9]).

Another difficulty in the modeling of clouds is their interaction with various processes that is not always well known or is difficult to describe in the context of a climate model. As an example, the relationship between clouds, aerosols and radiation should be mentioned. Further fields of interest for cloud modelers are e.g. the link between clouds and atmospheric chemistry as well as the cloud electricity.

3 The regional climate model REMO

3.1 General characteristics

The regional climate model REMO is a hydrostatic, three-dimensional atmospheric model, that has been developed in the context of the Baltic Sea Experiment (BALTEX) at the Max-Planck-Institute for Meteorology in Hamburg. It is based on the Europa Model, the former numerical weather prediction model of the German Weather Service and is described in Jacob (2001, [25]) and Jacob et al (2001, [26]). REMO uses the physical package of the global circulation model ECHAM4 (Roeckner et al. 1996, [14]) and is used in standard horizontal resolutions of $\frac{1}{2}^\circ$ and $\frac{1}{6}^\circ$ with 20 vertical levels. The model time step is 240 seconds for the $\frac{1}{2}^\circ$ horizontal resolution and 100 seconds for the $\frac{1}{6}^\circ$ horizontal resolution. Prognostic variables are the horizontal wind components, surface pressure, temperature, specific humidity and cloud liquid water. The vertical levels in REMO are represented in a hybrid coordinate system. Hybrid coordinates are following the surface orography in the lower levels and become independent from surface orography in higher atmospheric model levels. Three examples for the location of the atmospheric levels in pressure coordinates are given in figure 3.1 for surface pressures of 980hPa, 1010hPa and 1040hPa, respectively. The definition of the vertical levels determines that the lower atmospheric levels are better resolved than the higher atmosphere. For the three shown surface pressures, the 100hPa-thick atmospheric layer close to the surface is resolved by 4 to 5 model layers, providing good resolution of boundary layer processes. Higher up in the atmosphere, model levels have larger spacing, resulting in interval values of between 50 and 70 hPa.

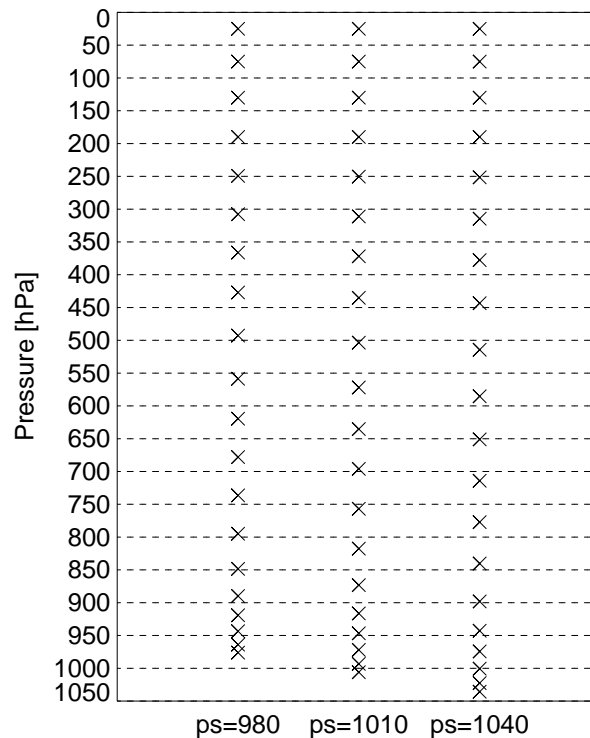


Figure 3.1: Height in pressure coordinates for hybrid coordinates of model levels with surface pressures of 980hPa, 1010hPa and 1040hPa, respectively. Crosses indicate the center of the respective model layer.

3.2 Clouds in REMO

As REMO is a hydrostatic mesoscale model with a limitation of the grid resolution to values of about 10 km, it is not possible to explicitly simulate cloud processes on all time and space scales. The simulation of clouds therefore is divided into the large-scale cloud scheme accounting for clouds developing on scales that can be described directly by the prognostic variables of the model and in the sub-grid scale scheme (also called *convection* scheme) for clouds on smaller scales (see section 2.2).

3.2.1 Large-scale cloud scheme

The stratiform cloud scheme in REMO, taken from the MPI Global Model ECHAM4, is based on the approach of Sundqvist (1978 [66]) and described in detail in the

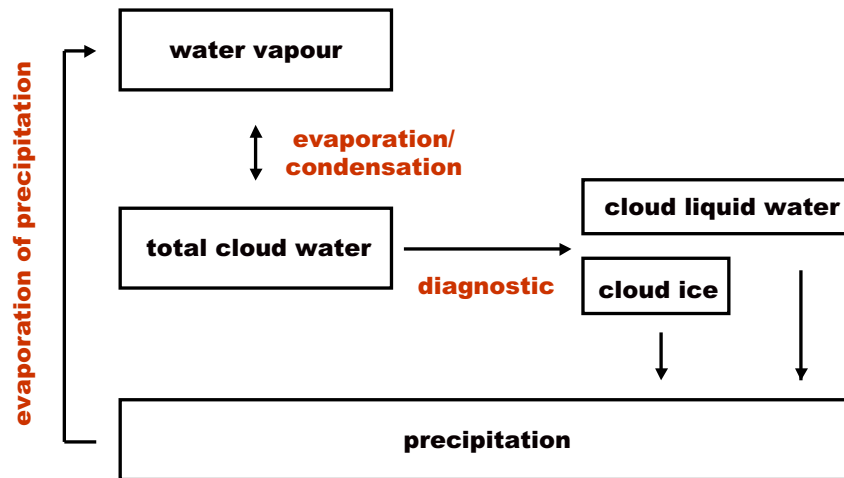


Figure 3.2: Schematical view of the standard cloud microphysics in REMO.

technical report of the *Deutsches Klimarechenzentrum* (German Climate Computing Center DKRZ, 1994 [14]) and in the description of the ECHAM model version 4 (Roeckner et al., 1996 [51]). The cloud scheme is illustrated in figure 3.2.

Sub-grid cloud formation is included in the large scale cloud scheme by incorporating fractional cloud cover (parameterized as a non-linear function of grid-mean relative humidity) for each grid box. This is done by defining a profile of the so called *critical relative humidity*, which has to be exceeded for the condensation process to begin. This profile is set to the value of 99% for the lowest model levels and is decreasing to a value of 80% in higher levels of the atmosphere. Prognostic variables related to cloud formation are water vapor and total cloud water. For these variables, budget equations are solved, taking into account the following sources and sinks:

- condensation of water in the cloudy part of the grid box
- evaporation of cloud water
- evaporation of cloud water transported into the cloudfree part of the grid box
- formation of precipitation by coalescence of cloud droplets and sedimentation of ice crystals
- evaporation of precipitation falling into the unsaturated part of a grid box

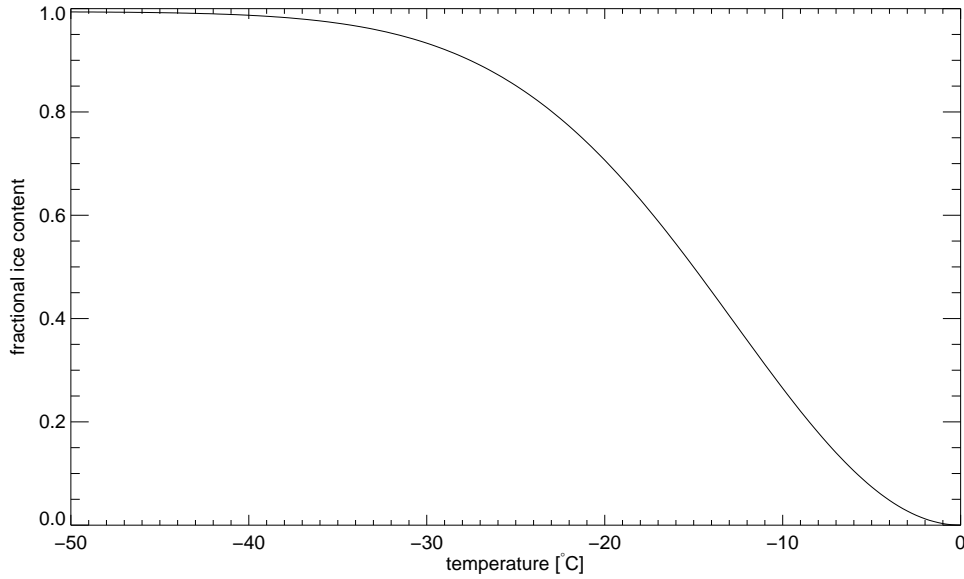


Figure 3.3: Diagnostic ice fraction

Diagnostic of the cloud ice content

As cloud ice is not a prognostic variable, the amount of ice in the cloud has to be diagnosed. Depending on the grid-mean temperature, the prognostic variable *total cloud water* (q_c) is splitted into cloud liquid water (q_{cl}) and cloud ice (q_{ci}). This is done using the following probability functions f_{liq} and f_{ice} (Rockel et al., 1991 [50]):

$$\begin{aligned}
 f_{liq} &= a + (1 - a)e^{-b \cdot (T - T_0)^2} & \forall & \quad T \leq T_0 \\
 f_{liq} &= 1 & \forall & \quad T > T_0 \\
 f_{liq} + f_{ice} &= 1,
 \end{aligned} \tag{3.1}$$

with $a = 0.0059$ and $b = 0.003102$. T is the mean temperature of the respective grid box and T_0 the melting point temperature. The diagnosed ice fraction f_{ice} calculated following equation 3.1 is illustrated in figure 3.3 for the temperature range between $-50 \text{ }^\circ\text{C}$ and $0 \text{ }^\circ\text{C}$.

From the liquid water and ice fractions, the cloud liquid water content (q_{cl}) and the

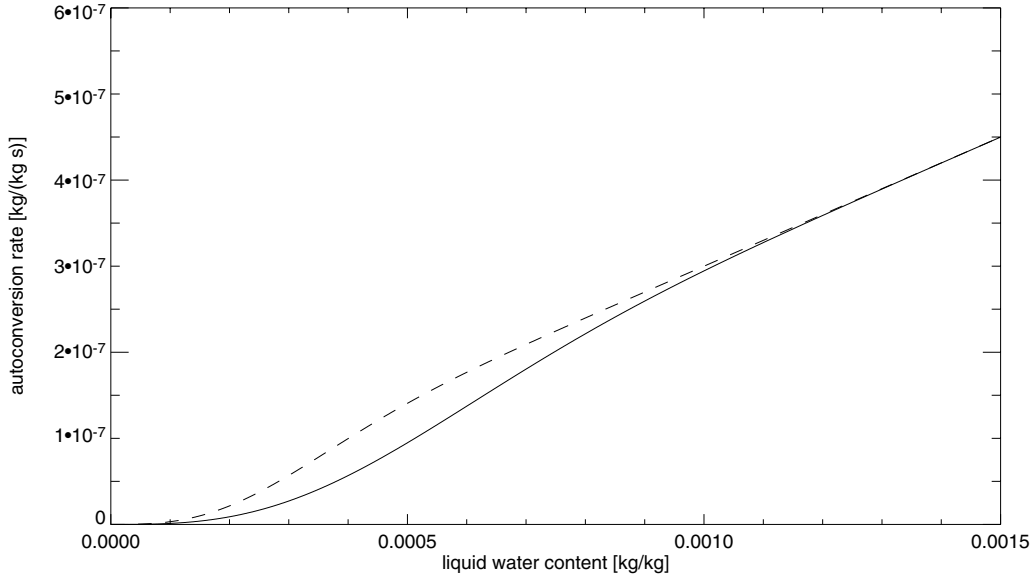


Figure 3.4: Autoconversion rate following Sundqvist (see equation, 3.3). Solid line: continental clouds. Dashed line: maritime clouds.

cloud ice content (q_{ci}) are then calculated as follows:

$$q_{cl} = f_{liq} \cdot q_c \quad \text{and} \quad q_{ci} = f_{ice} \cdot q_c \quad (3.2)$$

Warm clouds

For warm clouds, depletion of cloud liquid water by autoconversion of cloud droplets to precipitating rain drops as well as by the collision of cloud droplets with falling rain is taken into account.

Autoconversion of cloud droplets to rain (Q_{aut}) is parameterized in an exponential form following Sundqvist (1978 [66]):

$$Q_{aut} = q_{cl} \cdot (c_0 \cdot [1 - e^{-\left(\frac{q_{cl}}{q_{cr}}\right)^2}]), \quad (3.3)$$

where q_{cl} is again the cloud liquid water content, c_0 ($= 2 \cdot 10^{-4} s^{-1}$) and q_{cr} ($= 0.5 \cdot 10^{-3}$ for continental and $0.3 \cdot 10^{-3}$ for maritime clouds) are microphysical constants, determining the efficiency of rain formation. Figure 3.4 illustrates the dependency of the autoconversion rate from the cloud liquid water content both for continental and

maritime clouds. As maritime air compared to continental air usually comprises less aerosols which can act as cloud condensation nuclei, the droplets formed in maritime clouds are fewer and larger than those in continental clouds. This has been taken into account in the formulation of the autoconversion rate which increases faster with increasing liquid water content for maritime clouds (dashed line) than for continental clouds (solid line).

The reduction of cloud liquid water by collision of cloud droplets with falling rain (Q_{coll}) is parameterized as follows:

$$Q_{coll} = q_{cl} \cdot c_1 \langle P \rangle, \quad (3.4)$$

where $\langle P \rangle$ is the rain flux density at the top of the respective cloud layer and $c_1 = 1 \frac{m^2}{kg}$ is another microphysical constant determining the efficiency of rain formation and thus cloud lifetime.

Cold clouds

The formation of snow in cold clouds (P_{ci}) is parameterized relating the loss of ice crystals due to sedimentation to the divergence of the ice water flux:

$$P_{ci} = g \frac{\partial}{\partial p} (v_t \rho_{air} q_{ci}), \quad (3.5)$$

where g is the acceleration of gravity, ρ_{air} is the air density, q_{ci} the cloud ice content. The parameter v_t , which is the terminal velocity of the ice crystals, is related to the cloud ice content as derived from observations by Heymsfield (1977, [22]):

$$v_t = \alpha (\rho_{air} \cdot q_{ci})^\beta \quad (3.6)$$

α and β are empirical constants that have been set to 1.97 and 0.16 respectively (Roeckner et al., 1996 [51]). Figure 3.5 illustrates the sedimentation rate related to the cloud ice content. As the sedimentation rate depends on the temperature of the atmospheric layer containing the cloud as well as on cloud height, temperature and pressure (which enter in equation 3.5 via the air density $\rho_{air} = \frac{p}{R_v \cdot T}$) have been varied. Four exemplary clouds are illustrated. The influence of ρ_a on the sedimentation rate is relatively small, resulting in lower sedimentation rates for warmer clouds in lower atmospheric levels and higher rates for clouds that are either located in colder

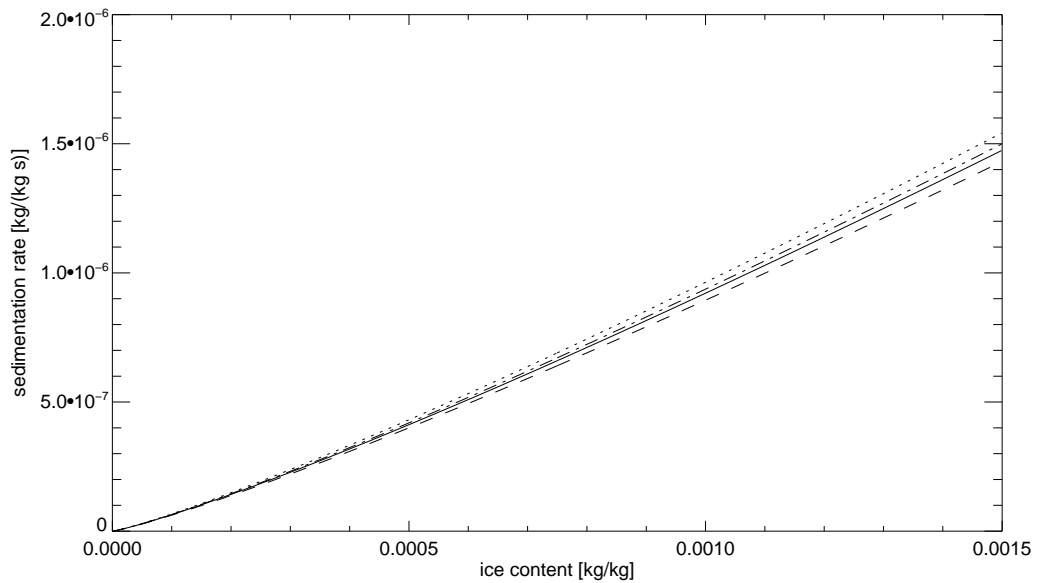


Figure 3.5: Sedimentation rate following Sundqvist for 4 different clouds: Solid line: $T=263.16\text{K}$, $P=800\text{hPa}$. Dotted line: $T=253.16\text{K}$, $p=800\text{hPa}$. Dashed line: $T=253.16\text{K}$, $p=750\text{hPa}$. Dot-dashed line: $T=243.16$, $p=750\text{hPa}$.

atmospheric layers or at higher heights. Comparing the sedimentation rate for cold clouds shown in figure 3.5 to the autoconversion rate for warm clouds shown in figure 3.4, it is obvious that for the selected clouds, the parameterized sedimentation process is more effective in removing cloud ice from the model atmosphere than the autoconversion process is for cloud liquid water: for model grid box cloud ice contents of less than 0.0015 kg/kg , the sedimentation rate lies between 0 and $1.6 \cdot 10^{-6} \frac{\text{kg}}{\text{kg}\cdot\text{s}}$; for equal liquid water contents, autoconversion results in rates between 0 and $4.5 \cdot 10^{-7} \frac{\text{kg}}{\text{kg}\cdot\text{s}}$.

3.2.2 Sub-grid scale cloud scheme

Cumulus convection in REMO is parameterized by a mass flux scheme following Tiedtke (1989 [68]) with some modifications. The scheme includes a static, one dimensional cloud model, taking into account the following processes:

- diabatic warming of the atmosphere resulting from latent heat exchange
- vertical transports of heat, moisture and momentum in convective updrafts and downdrafts and in zones of compensating subsidence
- interaction between up/downdrafts and the environmental air by consideration of entrainment and detrainment processes

As the scheme has been developed for global climate models with coarse horizontal resolutions, the cloud model aims to represent an ensemble of convective clouds located in one grid box. The properties described further are thus not representative for single convective clouds, but rather for their ensemble. Convection is classified into three categories:

Penetrative convection (convection type 1): Convection type 1 is designed to cover the effects of tropical hot towers that develop fast and reach high levels of the atmosphere. Penetrative convection has its basis in the near-ground boundary layer. It is mainly fed by advective transport of moisture into a grid box. Unlike in the procedure recommended by Tiedtke, the mass flux at cloud base is specified following an adjustment closure proposed by Nordeng (1994, [45]), linking the cloud base mass flux to the available convective potential energy (CAPE), which should be removed by convection in a characteristic time τ . In this way, the cloud base mass flux $M_{u,base}$ is inversely proportional to the adjustment time scale. This time scale strongly depends on the horizontal grid resolution of the model. Assuming that there exists a kind of quasi-equilibrium, in convective situations, the moistening from large-scale vertical advection of moisture (given in terms of the resolved vertical velocity of the model) should balance the drying from compensating subsidence around cumulus towers (given dependent on the vertical cloud mass flux). In order to keep the vertical mass flux at approximately the same size as the resolved

vertical velocity of the model, τ must be decreased as the horizontal resolution increases (Nordeng, 1996 [45]). For REMO which is usually used with a horizontal resolution of $\frac{1}{6}^\circ$ (approximately 18 km x 18 km grid sizes) or $\frac{1}{2}^\circ$ (approximately 50 km x 50 km grid sizes), τ has been set to a value of 15 minutes.

Shallow convection (convection type 2): Convection type 2 is designed for convection developing in undisturbed flow (no large-scale convergence). Typical convection associated with this convection type are tradewind cumuli under a subsidence inversion and daytime convection over land. Shallow convection emanates from the boundary layer. In case of shallow convection, the moisture convergence in the grid box is dominated by evaporation from the surface and not dynamically by advected moisture as in the case of penetrative convection. The rates of turbulent entrainment and detrainment are by a factor of three higher than for penetrative convection, accounting for the fact that shallow convection is usually smaller and more turbulent than penetrative convection and thus has larger exchanges with surrounding air.

Midlevel convection (convection type 3): Contrary to convection type 1 and 2, midlevel convection has its roots at levels above the boundary layer. Typical examples for this type of convection are e.g. convective cells occurring in rainbands at warm fronts or in the warm sectors of extratropical cyclones. In such cases, convection starting from the lower levels is often inhibited by a low-level temperature inversion and convection seems to be initiated by lifting low-level air dynamically to the level of free convection.

The convection scheme is unimodal, which means that only one convection type can occur in a column at a time, multi-layered convection is not described. Once the convection type is determined, the properties of the convective cloud ensemble are set according to the appropriate type. The intensity of convection - and therefore the vertical extent that the cloud can reach at maximum - strongly depends on the entrainment of air from the air masses surrounding the cloud into the cloud. Entrainment and detrainment processes are separated in turbulent entrainment and detrainment, which describes the mixing of cloud air and environmental air at the

cloud edges due to turbulent eddies and into organized entrainment and detrainment, which describes organized in and outflow associated with large-scale convergence. Turbulent entrainment and detrainment rates for cumulus updrafts are specified as follows:

Penetrative convection: $E_{pen} = 0.0001 \cdot M_u$

Shallow convection: $E_{sh} = 0.0003 \cdot M_u$

Midlevel convection: $E_{mid} = 0.0001 \cdot M_u$

With M_u being the upward Massflux in the respective cloud layer. Large entrainment rates lead to a weakening of the convective activity and therefore to lower cloud tops and are used to describe shallow convection which usually turbulently exchanges mass with its environment, whereas small entrainment rates are used to describe intense convection which leads to high reaching convective clouds.

For cumulus downdrafts, turbulent entrainment and detrainment rates are set to a value of $0.0002 \cdot M_d$, independent of the type of convection, where M_d is the downward massflux. Organized entrainment and detrainment calculations differ slightly from the original formulation by Tiedtke. Organized entrainment and detrainment are assumed to occur only for penetrative convection. Organized entrainment is restricted to the lower part of the clouds and is formulated in dependency of the buoyancy in the lower cloud levels. Organized detrainment is assumed to occur at all cloud heights. The original formulation by Tiedtke contained a restriction of organized detrainment to the highest cloud level, admitting that *"our detrainment assumption implies a unimodal cloud distribution with large detrainment from the deepest clouds and little detrainment from shallow clouds and medium deep clouds ... the assumption about shallow cumuli is questionable as they are often observed to produce another detrainment maximum immediately above cloud base"* (Tiedtke, 1989, [68]).

For all convection types a common formulation for the formation of precipitation is applied, linking the precipitation rate G_p to the water content of the convective cloud l_{conv} :

$$G_p = K(z) \cdot l_{conv} \tag{3.7}$$

The value of $K(z)$ is set to 0.01 except for thin clouds (vertical extent less than 750m), where it is set to zero to prevent shallow cumuli from producing precipitation. To determine the convective transport of mass and energy, the cloud base mass flux $M_{u,base}$ has to be specified. This is done by a moisture closure for shallow and midlevel convection and by a CAPE closure for penetrative convection.

The convection scheme is coupled to the large-scale cloud scheme by handing over the convective cloud liquid water detrained in the updrafts to the large-scale cloud scheme. The formulation of the convection scheme restricts convective activity to one single time level. The properties of convection in one grid column of the model are assigned for every time step without reconsidering the state of convection one timestep before. Thus the model includes no *memory* in the convection scheme, which would allow convective clouds to develop on a longer time scale.

4 Modifications of the cloud parameterization in REMO

4.1 Changes to the large-scale cloud scheme

One basic shortcoming of the stratiform cloud scheme used in REMO was that *"the precipitation formation in a mixed phase i.e. in a temperature range between about 0 °C and -40 °C , can not be treated independently for the ice phase and the liquid phase respectively. A proper treatment of the interaction between both phases, such as the rapid condensational growth of ice crystals at the expense of cloud droplets (Bergeron-Findeisen process) will require a more elaborate scheme which should be based on the budget equation for each phase."* (DKRZ 1992, [14]). This has been taken into account by implementing a prognostic equation for cloud ice, allowing for interactions between the in-cloud water components ice and liquid water. The new scheme is illustrated in figure 4.1.

The changes made in the stratiform cloud scheme have been adopted from the global circulation model ECHAM5 which is described in detail in the ECHAM5 manual (Roeckner et al., 2003 [52]). A description of the changes is given in the following:

Phase changes between cloud water and cloud ice

As mentioned above, a main benefit of the new scheme is that it allows for interaction between in-cloud liquid water and in-cloud ice. This interaction is described in the following melting and freezing processes:

1. Melting of cloud ice: At temperatures above 0 °C , all cloud ice melts instantaneously

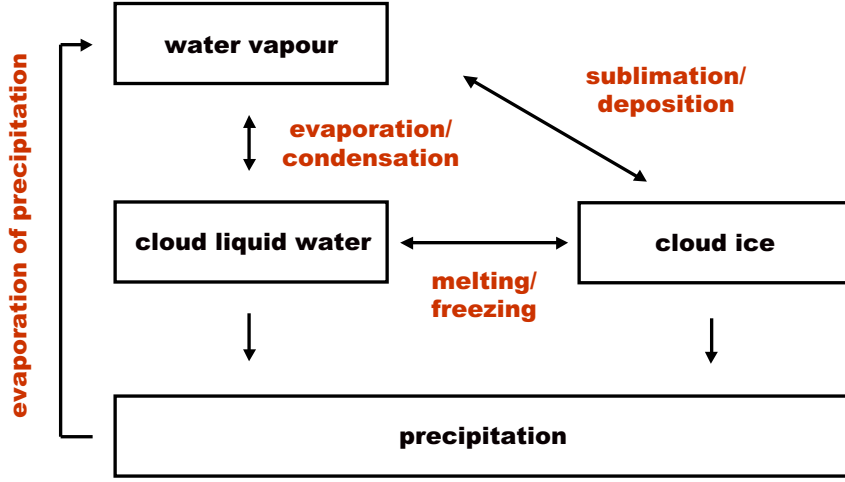


Figure 4.1: Schematical view of the cloud microphysics adopted from ECHAM5.

2. Freezing of cloud water: At temperatures below $-35\text{ }^{\circ}\text{C}$, all cloud water freezes instantaneously
3. Freezing of supercooled cloud droplets at temperatures between $-35\text{ }^{\circ}\text{C}$ and $0\text{ }^{\circ}\text{C}$: If cloud water is existing in this temperature range, two freezing processes are taken into account:

Stochastical and heterogeneous freezing

Stochastical and heterogeneous freezing (Fr_{sh}) is calculated following Levkov et al. (1992, [35]) and Murakami (1990, [43]). The equation is derived from the extrapolation of the Bigg's equation (Bigg, 1953a [5], Bigg, 1953b [6]) down to cloud droplet size.

$$Fr_{sh} = a \cdot (\exp[b(T_0 - T)] - 1) \cdot \frac{\rho_{air} \cdot q_{cl}^2}{\rho_{H_2O} \cdot N_l} \quad (4.1)$$

The constants $a = 100\text{m}^{-3}\text{s}^{-1}$ and $b = 0,66\text{K}^{-1}$ are taken from laboratory experiments and $T_0 = 273.16\text{K}$ is the freezing point. N_l is the cloud droplet number concentration, ρ_{air} the density of air, and $\rho_{H_2O} = 1000\frac{\text{kg}}{\text{m}^3}$ is the density of water. q_{cl} again is the cloud liquid water content.

Contact freezing

Contact freezing (Fr_{Con}) results from random collision of aerosol particles with supercooled water droplets. Following Levkov et al. (1992 [35]) and Cotton et al. (1986 [12]) it can be written as follows:

$$Fr_{Con} = m_{io} \cdot F_1 \cdot d_{ar}, \quad (4.2)$$

where $m_{io} = 10^{-12}kg$ is the initial mass of a nucleated ice crystal. $d_{ar} = 1,4 \cdot 10^{-8} \frac{m^2}{s}$ is the aerosol diffusivity, and $F_1 = 4\pi \cdot rad_l \cdot N_l \cdot N_a / \rho_{air}$. $rad_l = (\frac{0,75 \cdot q_{cl}}{\pi \cdot \rho_{H2O} \cdot N_l})^{1/3}$ is the mean cloud droplet radius, and $N_a = 2 \cdot 10^5 \cdot (270,15 - T)$ is a factor to approximate the concentration of active contact nuclei for contact freezing. With this factor, it is taken into account that not all aerosol particles can act as ice nuclei.

In ECHAM5, the cloud droplet number concentration N_l can directly be related to the mass of sulfate aerosols mSO_4^{2-} (Lohmann and Roeckner 1996, [36]). As in REMO information about aerosol masses is not available, the cloud droplet number concentration N_l is calculated considering maritime and continental cloud properties as well as the dependence of the cloud droplet number concentration from height, as it has been done in the former ECHAM version 4. This is illustrated in figure 4.2 on the following page.

Warm Clouds

Cloud droplets in warm clouds grow by collision and coalescence (summed up under the term *autoconversion*). Additionally, cloud droplets are collected by falling rain. These processes are formulated in the following way:

The formation of precipitation by autoconversion separates maritime and continental clouds by taking into account not only the in-cloud liquid water content (q_{cl}), but also the cloud droplet number concentration N_l (Beheng, 1994, [4]). Autoconversion (Q_{aut}) is derived from the stochastic collection equation, which describes the evolution in time of a droplet spectrum changing by collisions among droplets of different sizes:

$$Q_{aut} = (\gamma_1 \cdot 6 \cdot 10^{28} n^{-1.7} (10^{-6} N_l)^{-3.3} (10^{-3} q_{cl})^{4.7}) / \rho_{air}, \quad (4.3)$$

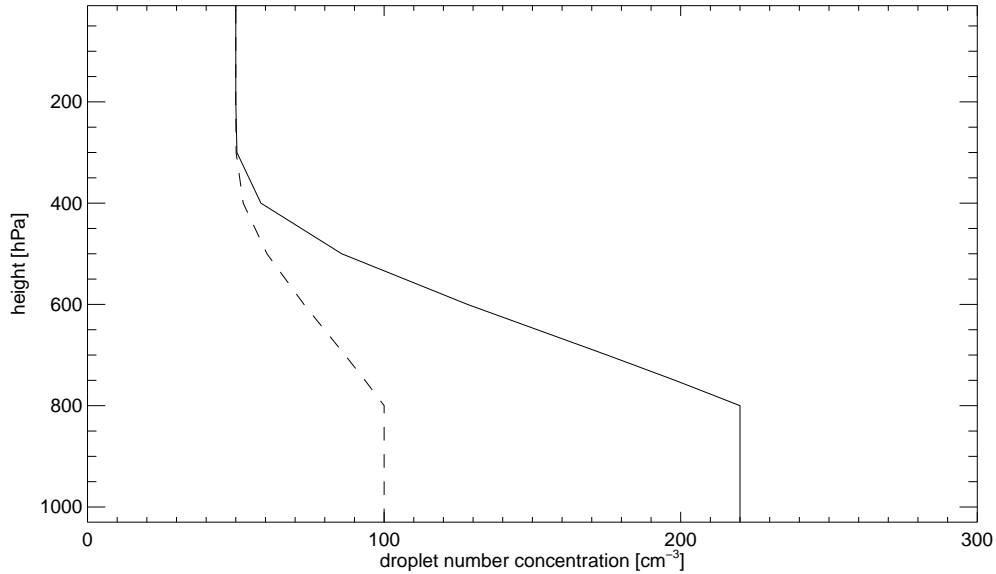


Figure 4.2: Droplet number concentration as calculated in REMO. Solid line: continental clouds, dashed line: maritime clouds.

where $n = 10$ is the width parameter of the initial cloud droplet spectrum and $\gamma_1 = 15$ a tunable parameter which determines the efficiency of the autoconversion process and hence cloud lifetime.

Figure 4.3 compares the autoconversion rate following Sundqvist described in section 3.2.1 to the new autoconversion rate. For better interpretability, the curves are plotted logarithmic in the y-axis. As the new formulation depends on the droplet number concentration N_l , which varies with height (see figure 4.2), only boundary layer clouds are illustrated. For these clouds, N_l is set to 220cm^{-3} for continental clouds and to 100cm^{-3} for maritime clouds. As one can see in figure 4.3, the Beheng-type autoconversion rates are in most cases smaller than the Sundqvist-type rates. This is especially true for the continental clouds. Maritime clouds have lower Beheng-type autoconversion rates for liquid water contents of up to 0.008 kg/kg . For higher values of cloud liquid water content, Beheng-type autoconversion rates for maritime clouds are rapidly exceeding the Sundqvist-type rates. Both autoconversion rates shown in figure 4.3 are dependent on the grid resolution. This follows from the nonlinear dependency of the autoconversion rates from the grid-mean cloud liquid water content. The presence of sub grid scale variability causes

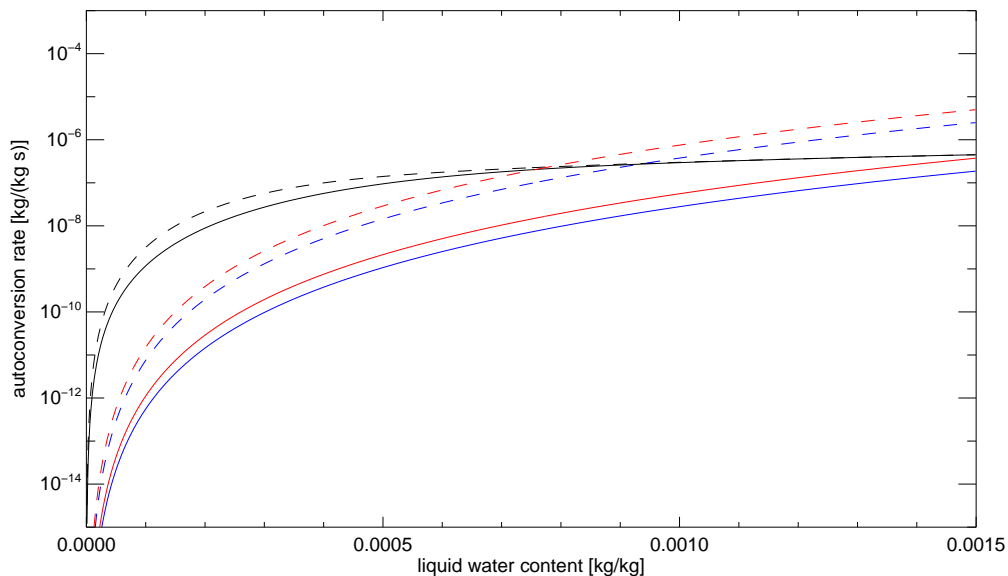


Figure 4.3: Autoconversion rate. Black: Parameterization following Sundqvist (see equation 3.3). Solid line: continental clouds. Dashed line: maritime clouds. Red: Parameterization following Beheng with $\gamma_1 = 15$ (see equation 4.3). Blue: Parameterization following Beheng with $\gamma_1 = 7.5$ (see equation 4.3). Solid lines (red and blue): continental boundary layer clouds with $N_l = 220\text{cm}^{-3}$, dashed lines (red and blue): maritime boundary layer clouds with $N_l = 100\text{cm}^{-3}$. The timestep has been set to 100 s.

a bias between the average of the process rate (here: autoconversion rate) over the grid cell and the process rate computed from grid cell average (see e.g. Wood et al., 2002 [71]). Figure 4.4 illustrates the problem. Imagine a model simulation with finer grid resolution, which comes up with liquid water contents in two different grid boxes of $0.001 \frac{\text{kg}}{\text{kg}}$ (lwc_1) and $0.0014 \frac{\text{kg}}{\text{kg}}$ (lwc_2) respectively. For the two boxes, the autoconversion then is calculated separately, yielding rates of $0.55 \cdot 10^{-7} \frac{\text{kg}}{\text{kg}\cdot\text{s}}$ and $2.7 \cdot 10^{-7} \frac{\text{kg}}{\text{kg}\cdot\text{s}}$ respectively (see the solid black lines in figure 4.4). Averaging the two rates thus gives a mean autoconversion rate of $1.625 \cdot 10^{-7} \frac{\text{kg}}{\text{kg}\cdot\text{s}}$ (illustrated by the short-dashed line). A model with a coarser grid resolution would have seen only one grid box instead of two, including the two-box-mean value of liquid water content, i.e. $0.0012 \frac{\text{kg}}{\text{kg}}$. The autoconversion rate belonging to this mean liquid water content would be $1.3 \cdot 10^{-7} \frac{\text{kg}}{\text{kg}\cdot\text{s}}$ (see long-dashed line). For this example, the bias would result in autoconversion rates that are by 20 % lower for the simulation with coarser

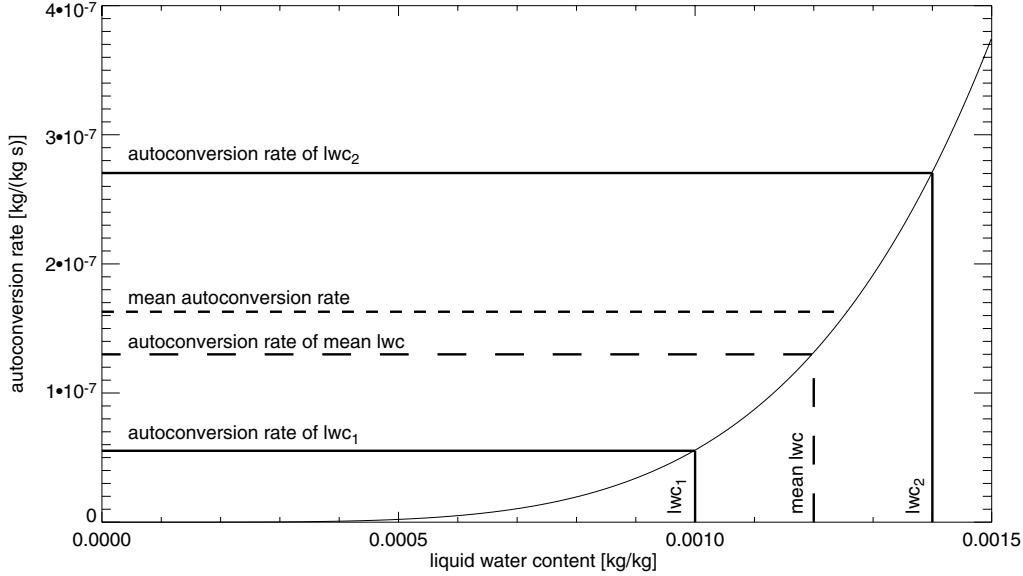


Figure 4.4: Illustration of the autoconversion rate bias. For explanation see the text below.

horizontal resolution. The autoconversion rate bias increases with decreasing grid resolution. (Pincus and Klein, 2000 [46]). For this reason, the tuning parameter γ_1 in equation 4.3 has been introduced in the global model ECHAM. For ECHAM, it has been set to 15 (Lohmann and Roeckner, 1995 [36]). This value has been adopted for calculations with the regional model REMO and will be subject of one of the sensitivity studies discussed in section 5.4. Exemplarily, in figure 4.3, the Beheng-type autoconversion rate has been drawn twice, once with $\gamma_1 = 15$, as used in ECHAM5 (red lines), and once with a reduced factor of $\gamma_1 = 7.5$ (blue lines).

The autoconversion rate following Beheng also strongly depends on the droplet number concentration N_l . The rates for continental and maritime clouds shown in fig. 4.3 (red lines) only differ by the choice of N_l in equation 4.3 and lead to distinctly differing precipitation rates for both cloud types.

Once formed, raindrops continue growing by accretion of cloud droplets. This process is described by the two summands in equation 4.4.

$$Q_{ralc} = a_3 \cdot q_{cl} \cdot r_{rain} + \gamma_2 \rho_{air} \cdot Q_{aut} \Delta t \quad (4.4)$$

The first gives the reduction of cloud liquid water by the rain falling into the cloudy part of the grid box (r_{rain}), with $a_3 = 6 \frac{m^3}{kg \cdot s}$. The second term considers those cloud

droplets that have just been formed by autoconversion (Q_{aut}), i.e. the local rain-water production during a timestep (Δt), that also collect cloud liquid water. This second terms contains a tunable scale dependent parameter γ_2 .

Cold clouds

Snow forms from cloud ice by the aggregation process, describing the accretional growth of cloud ice particels until their terminal velocity is large enough to fall down as snow. The aggregation rate for the conversion of cloud ice to snow (Q_{agg}) is calculated following Levkov et al. (1992), based on Murakami (1990):

$$Q_{agg} = \gamma_3 \frac{\rho_{air} q_{ci}^2 a_4 E_{ii} X \left(\frac{\rho_0}{\rho_{air}}\right)^{1/3}}{-2\rho_i \log\left(\frac{r_{vi}}{r_{s0}}\right)^3} \quad (4.5)$$

γ_3 is a tunable parameter, determining the efficiency of the snow formation and hence cloud lifetime. q_{ci} is the cloud ice content. $E_{ii} = 0.1$ is the collection efficiency between ice crystals, and $X = 0.25$ the dispersion of the fall velocity spectrum of cloud ice. $\rho_0 = 1.3 \frac{kg}{m^3}$ is a reference density of air and ρ_{air} the air density in the grid box. $a_4 = 700 s^{-1}$ is an empirical constant, $r_{s0} = 10^{-4} m$ the smallest radius of a particle in the category *snow*, and r_{vi} the mean volume ice crystal radius, which can be related to the mean effective ice crystal radius (r_{ei}) and to the cloud ice content (q_{ci}) by the following relations (Roeckner et al., 2003 [52]):

$$r_{vi} = 10^{-6} \left(\sqrt{(2809 r_{ei}^3 + 5113188)} - 2261 \right)^{1/3} \quad (4.6)$$

$$r_{ei} = 83.3 (10^3 \rho_{air} \cdot q_{ci})^{0.216} \quad (4.7)$$

Figure 4.5 compares the sedimentation rate following Sundqvist described in section 3.2.1 to the sedimentation rate following Levkov et al., given in equation 4.5 for an exemplary cloud at a temperature of -20 °C and at 800 hPa height. The y-axis is logarithmic for better comparability. For this cloud, the Levkov-type sedimentation rate (red curve) continuously lies below the Sundqvist-type sedimentation rate (black curve). Thus, for equal cloud ice contents, the cloud scheme with the Levkov-type sedimentation rate will produce less snow than the cloud scheme using the sedimentation rate following Sundqvist.

Once formed, snow particles grow by accretion of cloud ice (given in equation 4.8)

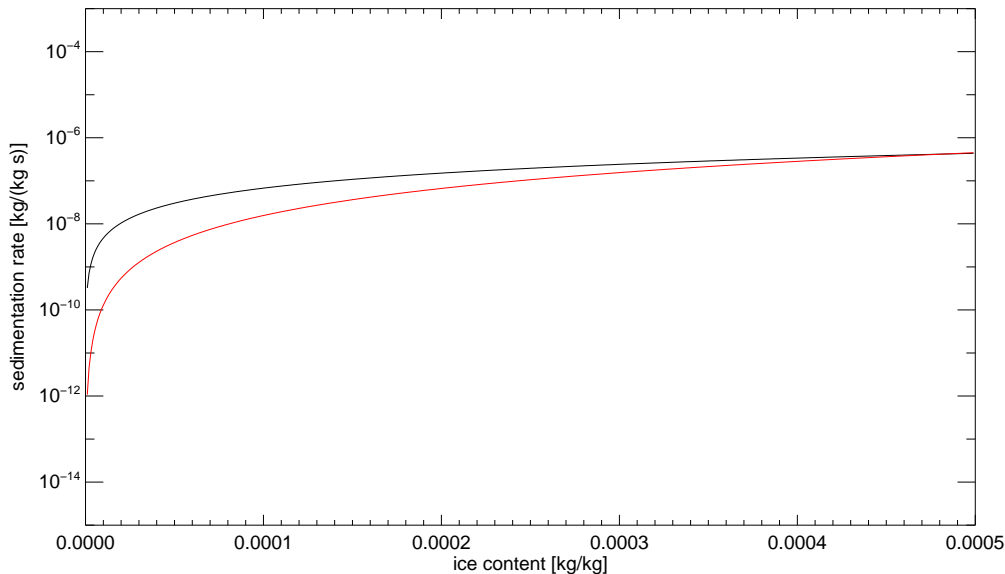


Figure 4.5: Sedimentation rate. Black: Parameterization following Sundqvist (see equation 3.5). Red: Parameterization following Levkov with $\gamma_3 = 220$ (see equation 4.5). The curves are for an exemplary cloud at $-20\text{ }^\circ\text{C}$ at 800 hPa.

as well as by accretion of cloud droplets (given in equation 4.12). The accretion rate of ice crystals by snow is as follows:

$$Q_{saci} = \frac{\pi \cdot E_{si} n_{0s} a_4 q_{ci} \Gamma(3 + b_4)}{4\lambda_s^{3+b_4}} \left(\frac{\rho_0}{\rho_{air}}\right)^{1/2}, \quad (4.8)$$

where $\rho_0 = 1.3 \frac{\text{kg}}{\text{m}^3}$ is the reference air density. Γ is the Gamma-Function, and $a_4 = 4.83$ and $b_4 = 0.25$.

E_{si} in equation 4.8 is the collection efficiency of snow with cloud ice, which depends on temperature following this relation:

$$E_{si} = \exp[0.025(T - T_0)], \quad (4.9)$$

where T is the grid-mean temperature and $T_0 = 273.16\text{K}$. Snow crystals are assumed to be distributed exponentially. Their size distribution is given by the following equation derived by Gunn and Marshall (1958 [19]):

$$n_s(D_s) = n_{0s} \exp(-\lambda_s D_s), \quad (4.10)$$

where $n_s(D_s)$ is the concentration of particels of diameter D_s per unit size interval, and $n_{0s} = 3 \cdot 10^6 m^{-4}$ the intercept parameter obtained from measurements. λ_s is the slope of the particle size distribution:

$$\lambda_s = \left(\frac{\pi \rho_s n_{0s}}{\rho_{air} r_{snow}} \right)^{0.25}, \quad (4.11)$$

where $\rho_s = 100 \frac{kg}{m^3}$ is the bulk density of snow and r_{snow} is the mass mixing ratio of snow. With $\left(\frac{\rho_0}{\rho_{air}} \right)^{0.5}$ in equation 4.8, the lower speed of snow at atmospheric levels with higher air density is taken into account.

The accretion of snow with cloud droplets (Q_{sacl}) is calculated similar to the accretion of snow with ice crystals:

$$Q_{sacl} = \gamma_4 \cdot \frac{\pi \cdot E_{sl} n_{0s} a_4 q_{cl} \Gamma(3 + b_4)}{4 \lambda_s^{3+b_4}} \left(\frac{\rho_0}{\rho_{air}} \right)^{1/2} \quad (4.12)$$

$E_{sl} = 1$ in equation 4.12 is the collection efficiency of snow with cloud droplets. $\gamma_4 = 0.1$ is a tunable parameter which reduces the efficiency of this process.

The complete microphysical parameterization includes four parameters that have been used as *tuning* parameters for the implementation of the new cloud scheme in the global model ECHAM5 (Roeckner et al., 2003 [52]). These are: γ_1 , which controls the efficiency of precipitation formation in warm clouds by autoconversion (equation 4.3), γ_2 , determining the rate of accretional growth of cloud droplets formed in the grid box (equation 4.4), γ_3 , used to scale the conversion of cloud ice to snow (equation 4.5), and γ_4 , controlling the efficiency of the growth of snow by accretion of cloud droplets (equation 4.12). Since *tuning* of the model also is *tuning* the physical parameterizations to model resolution, the sensitivity of the model to these parameters has to be analyzed in respect to the model resolution. This will exemplarily be done in section 5.4 for the parameter γ_1 in the autoconversion rate. γ_1 has been chosen for the sensitivity study because other studies (e.g. Wood et al., 2002, [71]) have highlighted the importance of the scale dependency of the autoconversion rate formulation used in large-scale atmospheric models.

The impact of the introduction of the prognostic cloud ice scheme in the global model ECHAM4 on climate and climate sensitivity has been described by Lohmann and Roeckner (1995, [36]). They concluded that the largest differences (of global mean values) resulting from the changes described above occur in the ice water path, which increases by 33 % for January and 24 % in July. Total precipitation decreases

by 7%. This goes along with a change in the ratio between convective and large scale precipitation in favor of the convective part of the total amount of precipitation.

4.2 Changes to the sub-grid scale cloud scheme

The Tiedtke convection scheme is designed for and tuned to tropical convection. As described in section 3.2.2, the parameterization focuses on phenomena like high-reaching tropical convection (penetrative convection), the tradewind convection under a subsidence inversion, occurring in the ridge region of tropical easterly waves or daytime convection over land (shallow convection) and convection associated with cyclonic warm rainbands (midlevel convection).

Cold convective clouds occurring in cold air outbreaks over sea in the extratropical atmosphere are fed by moisture supply through surface evaporation as it is the case for Tiedtke-type shallow convection, but they differ in terms of temporal evolution as well as in the formation of precipitation remarkably from what the Tiedtke convection scheme actually is designed for. In these cases, as convection is mainly fed by surface evaporation, the convection scheme decides for shallow convection (see section 3.2.2). Simulations with Cloud Resolving Models (Gregory, 1997 [18]) as well as observations (Kershaw and Gregory, 1997 [29]) indicated that the characteristics of such clouds would be better represented by applying deep convection parameters. The high entrainment rates applied to shallow convection lead to an underestimation of the cloud depth and the high detrainment rates to an overestimation of the decrease of mass fluxes with height.

For this reason, a fourth type of convection has been added to the Tiedtke convection scheme. On the basis of Tiedtke's convection type 2 (shallow convection), convection type 4 has been defined. In the following, this convection type will be called cold convection. Triggering criteria for this new convection type are the following assumptions:

- conditions for convective activity are fulfilled (determination of convective activity through the lifting-parcel method described in section 2.2)
- surface evaporation exceeds advection of moisture (criterion for shallow convection)
- If there is either cloud water or cloud ice present in the lower atmosphere:
In the lower part of the atmosphere ($p > 750hPa$), the integrated amount of cloud ice exceeds the amount of cloud liquid water. This accounts for

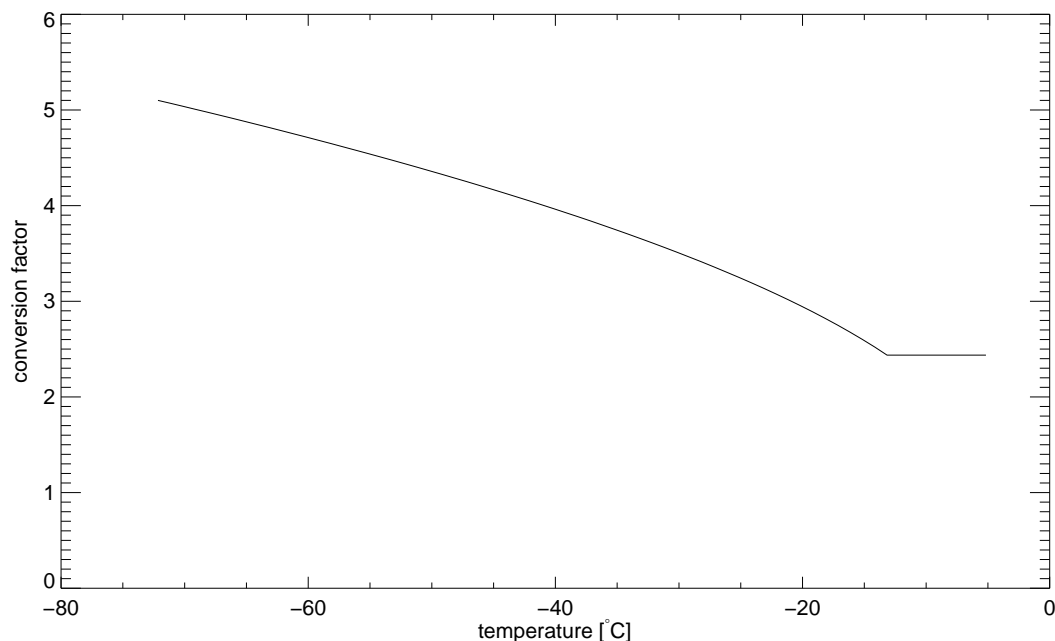


Figure 4.6: Temperature dependent factor for the conversion rate from liquid water to rain for cold convection

embedded convection and its link to the environment. If there is no cloud water / cloud ice in the lower atmosphere:

The decision whether shallow convection or cold shallow convection is activated depends on the temperature in the lower atmosphere: For temperatures lower than $0\text{ }^{\circ}\text{C}$ in the lowest level, cold convection is activated.

Once cold convection is identified, the following attributes are specified for convection in this column:

- The restriction that was meant to suppress precipitation originating from shallow convective clouds is deactivated, allowing the formation of snow and rain even from shallow cold cumuli as it has been observed for higher latitudes (e.g. Müller et al., 1999 [42]).
- The empirical function that relies the precipitation formation to the liquid water contents ($K(z)$ in equation 3.7) has been complemented with a factor that accounts for the properties of formation of precipitation in cold clouds (see figure 4.6). By applying this temperature dependent factor to clouds

at temperatures below 268K, the enhancement of precipitation efficiency by the Bergeron-Findeisen process and by freezing processes is included (Tiedtke 1993, [69]).

- The rates of turbulent entrainment and detrainment for cold convection are set to the corresponding values for penetrative convection.
- For cold convection, the mass flux at cloud base is specified by a CAPE closure.

5 Validation and application of the new cloud scheme

5.1 Experimental setup

The modified cloud scheme has been applied for one case study (the North Atlantic cyclone *Caroline*) and for two longer simulations of European climate (*Baltic* $\frac{1}{2}^\circ$ and *Baltic* $\frac{1}{6}^\circ$). All simulations have been performed with the unchanged version of REMO (*REMO_{standard}*) and with the modified version including all changes described in chapter 4 (*REMO_{cold}*). All accomplished simulations are summed up in table 5.1. The simulations have been done on a rotated spherical grid, to ensure that the model grid box sizes are uniform in the whole simulation area. This is done by rotating the grid coordinates the way that the rotated equator is located in the center of the model simulation domain. The rotation is defined by the position of the rotated north pole, which is $40^\circ\text{N} / 150^\circ\text{E}$ for the simulations of the cyclone *Caroline* and $35.5^\circ\text{N} / 170^\circ\text{E}$ for the simulations of European climate. All $\frac{1}{2}^\circ$ resolution simulations have been initialized and driven by data from ECMWF analyses. The $\frac{1}{6}^\circ$ resolution simulations have been done in a *double nesting* procedure, i.e. $\frac{1}{6}^\circ$ simulations are initialized and driven by data of REMO $\frac{1}{2}^\circ$ simulations.

This chapter starts with the discussion of the simulation of the cyclone *Caroline*. The examinations will be done for the simulations *Caro 1* $\frac{1}{6}^\circ$ and *Caro 2* $\frac{1}{6}^\circ$ (see table 5.1) and are presented in section 5.2. From section 5.3.1 to 5.3.6, the simulation of European climate with *REMO_{standard}* and *REMO_{cold}* will be presented for different atmospheric parameters, based on the simulations *Baltic 1* $\frac{1}{6}^\circ$ and *Baltic 2* $\frac{1}{6}^\circ$ (see table 5.1).

As discussed in chapter 4, the parameterizations of the cloud microphysical processes are possibly resolution dependent. The applied *double nesting* technique with the consistent model chain (*Baltic 1* $\frac{1}{2}^\circ$ and *Baltic 1* $\frac{1}{6}^\circ$, *Baltic 2* $\frac{1}{2}^\circ$ and

Baltic 2 $\frac{1}{6}^\circ$) however makes it difficult to separate the influence of grid resolution from the influence of the driving fields for the $\frac{1}{6}^\circ$ simulations. For this reason, a third $\frac{1}{6}^\circ$ resolution simulation has been performed with *REMO_{cold}*, which has been driven by the *REMO_{standard}* $\frac{1}{2}^\circ$ resolution simulation, which is called *Baltic 3* $\frac{1}{6}^\circ$. This model-version-combination will in the following be addressed as *REMO_{cold_driven_by_standard}*. The comparison of *REMO_{standard}* $\frac{1}{6}^\circ$ and *REMO_{cold_driven_by_standard}* $\frac{1}{6}^\circ$ will be shown and will be opposed to the differences between the *REMO_{standard}* and *REMO_{cold}* simulations in $\frac{1}{2}^\circ$ resolution (section 5.4.1). In this way, it is possible to analyze the direct influence of the different cloud parameterizations in the model in both resolutions, without the constraint of having different driving fields. These examinations will be presented in section 5.4.1.

To assess the sensitivity of the parameterization to changes in the autoconversion of cloud droplets to rain in warm clouds and the sensitivity to the influence of the critical relative humidity (see chapter 4), two additional sensitivity studies (*sensi 1* and *sensi 2*) have been conducted, which are presented in section 5.4.2.

simulation	model version	grid resolution, model timestep & driving data	simulation period
<i>Caro 1</i> $\frac{1}{2}^\circ$	<i>REMO_{standard}</i>	$\frac{1}{2}^\circ$, 240sec. ECMWF Analyses	February 1997
<i>Caro 2</i> $\frac{1}{2}^\circ$	<i>REMO_{cold}</i>	$\frac{1}{2}^\circ$, 240sec. ECMWF Analyses	February 1997
<i>Caro 1</i> $\frac{1}{6}^\circ$	<i>REMO_{standard}</i>	$\frac{1}{6}^\circ$, 100sec. <i>Caroline 1</i> $\frac{1}{2}^\circ$	1997, 16th to 18th of February
<i>Caro 2</i> $\frac{1}{6}^\circ$	<i>REMO_{cold}</i>	$\frac{1}{6}^\circ$, 100sec. <i>Caroline 2</i> $\frac{1}{2}^\circ$	1997, 16th to 18th of February
<i>Baltic 1</i> $\frac{1}{2}^\circ$	<i>REMO_{standard}</i>	$\frac{1}{2}^\circ$, 240sec. ECMWF Analyses	1999 to 2003
<i>Baltic 2</i> $\frac{1}{2}^\circ$	<i>REMO_{cold}</i>	$\frac{1}{2}^\circ$, 240sec. ECMWF Analyses	1999 to 2003
<i>Baltic 1</i> $\frac{1}{6}^\circ$	<i>REMO_{standard}</i>	$\frac{1}{6}^\circ$, 100sec. <i>Baltic 1</i> $\frac{1}{2}^\circ$	1999 to 2003
<i>Baltic 2</i> $\frac{1}{6}^\circ$	<i>REMO_{cold}</i>	$\frac{1}{6}^\circ$, 100sec. <i>Baltic 2</i> $\frac{1}{2}^\circ$	1999 to 2003
<i>Baltic 3</i> $\frac{1}{6}^\circ$	<i>REMO_{cold_driven_by_standard}</i>	$\frac{1}{6}^\circ$, 100sec. <i>Baltic 1</i> $\frac{1}{2}^\circ$	1999 to 2003
<i>sensi 1</i>	<i>REMO_{aut}</i>	$\frac{1}{2}^\circ$, 100sec. ECMWF Analyses	1999 to 2003
<i>sensi 2</i>	<i>REMO_{hum}</i>	$\frac{1}{2}^\circ$ 100sec. ECMWF Analyses	1999 to 2003

Table 5.1: Summary of accomplished simulations

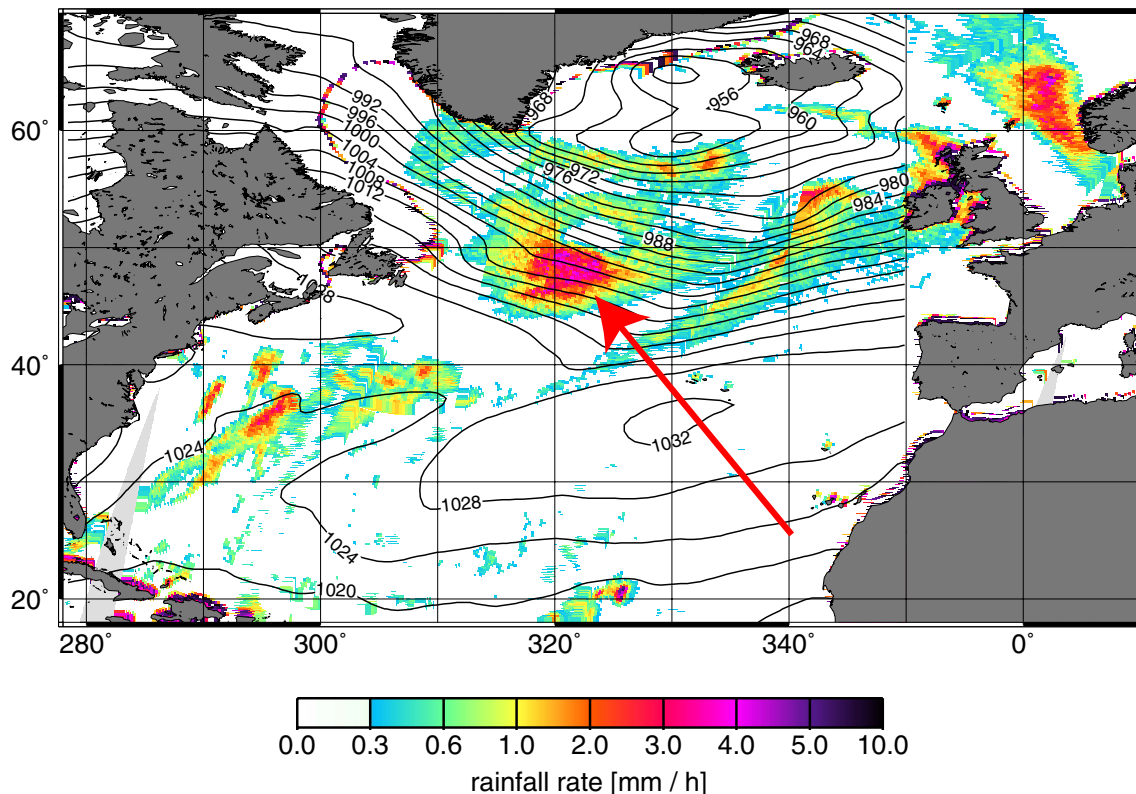
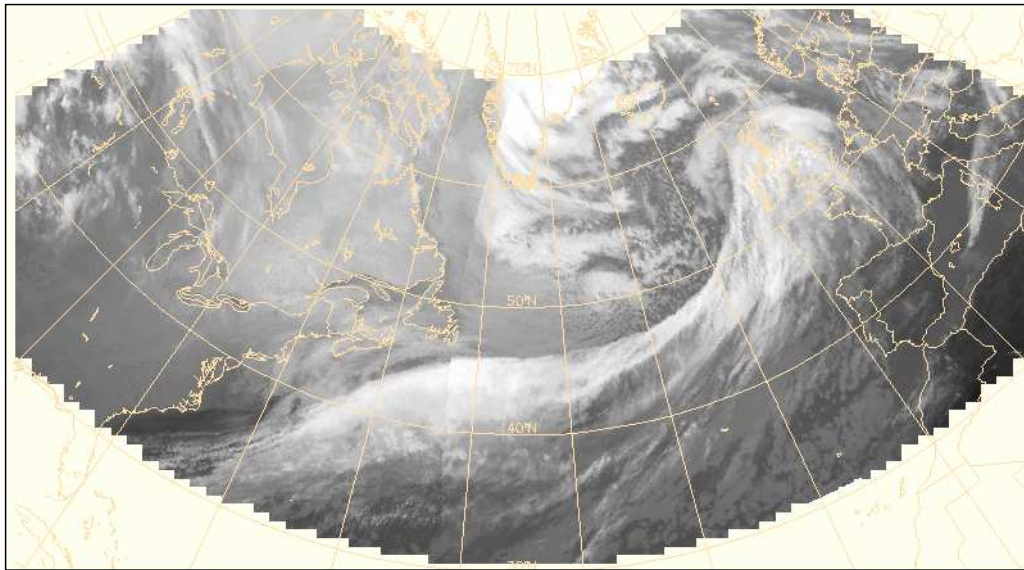


Figure 5.1: SSM/I derived instantaneous rainfall rate [mm/h] for 1997-02-17, combined from three satellite overpasses in the morning. The postfrontal precipitation maximum is highlighted by a red arrow. Source: Keup-Thiel et al. [30].

5.2 North Atlantic Cyclone Caroline

The extension of the convection scheme to cold convection described in section 4.2, has been developed and tested on the basis of a cold air outbreak on the backside of the cold front of the North Atlantic cyclone *Caroline* in February 1997. The simulation of the North Atlantic cyclone *Caroline* has been chosen as example of the importance of cold convective clouds over warm surfaces. Extratropical cyclones as *Caroline* are important sources of freshwater for Europe as most of the cyclones reaching the European continent develop over the North Atlantic Ocean. *Caroline* and the performance of the regional climate model REMO in simulating this cyclone have been described in detail by Keup-Thiel et al. (2003 [30]). In their paper they compared simulated precipitation to estimations of precipitation derived from



MOSAIC IR DATE: 9702171200

Figure 5.2: Satellite infrared mosaic from 17th of February 1997, 12:00 UTC.
Source: <http://www.cnrm.meteo.fr/dbfastex/atlas> (Météo France).

SSM/I (passive microwave Special Sensor Microwave/Imager) satellite observations, using the Bauer & Schlüssel algorithm (Bauer and Schlüssel, 1993 [3]). Their studies revealed that the amount of precipitation originating from the frontal system calculated by REMO almost matched the values derived from SSM/I satellite data, whereas the observed high precipitation rate in the cold air outbreak behind the front (see figure 5.1 for the SSM/I derived precipitation) was underestimated by the model. Figure 5.2 shows a satellite infrared mosaic image of the North Atlantic cyclone *Caroline* on the 17th of February 1997 at 12:00 UTC. For the composite, IR images derived from the geostationary satellites GOES-EAST and METEOSAT-7 have been combined to cover the North Atlantic region. The large frontal system spanning from the British Isles to the Coastal region of northern North America is followed by a convective cloud cluster behind the front. In this region, the cold air streaming from the ice-covered sea surface in the east of the coastline of Canada to the open (and therefore relatively warm) sea surface of the North Atlantic is causing intense fluxes of sensible and latent heat.

Investigations of Klepp (2001 [31]) showed that also the reanalysis products of ECMWF (European Centre for Medium-Range Weather Forecasts) as well as other

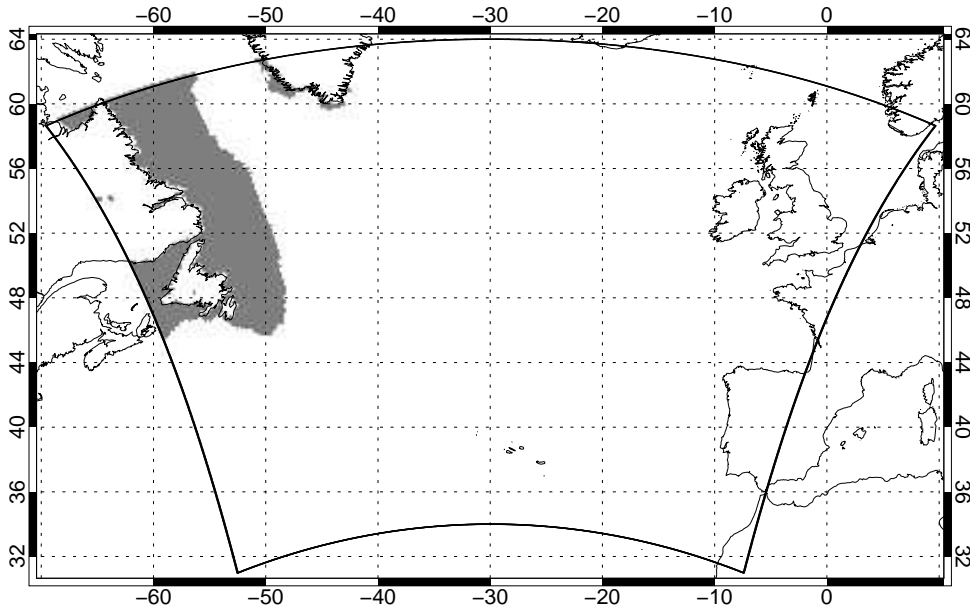


Figure 5.3: Model simulation domain for the $\frac{1}{6}^\circ$ horizontal resolution. In grey, the simulated sea ice edge for the 17th of February 1997 09:00 UTC is marked.

commonly used algorithms to derive precipitation rates from satellite observations were not able to capture the high precipitation behind the front. From his investigations, he concluded that for the 17th of February 1997 in the morning, 60% of the total precipitation originating from the cyclone *Caroline* was postfrontal precipitation, having a mean precipitation intensity of $0.9 \frac{mm}{h}$. 25% of the precipitation was connected to the cold front with a mean intensity of $0.7 \frac{mm}{h}$ and the remaining 15% to the warmfront of the cyclone with a mean intensity of also $0.7 \frac{mm}{h}$. The derived precipitation intensities are limited by the fact that algorithms to derive rain and snow rates quantitatively from satellite observations have still rather large uncertainty rates. For the Bauer & Schlüssel algorithm, Klepp indicates an accuracy of $0.5 \frac{mm}{h}$. In Morrissey and Wang (1995 [40]) the quality of two satellite based rainfall estimation algorithms is given by correlation values between monthly surface-measured rainfall and satellite remote sensing monthly rainfall of 0.87 and 0.88 respectively. The postfrontal precipitation in this cold air outbreak behind the front was supported by ship observations, so that the general underestimation of the model simulated postfrontal precipitation can be taken as a fact.

$REMO_{standard}$	penetrative	midlevel	shallow
Percentage of occurrence	1.9 %	45.9 %	52.2 %
Mean precipitation rate	$0.78 \frac{mm}{h}$	$0.08 \frac{mm}{h}$	$0.11 \frac{mm}{h}$

Table 5.2: Percentage of occurrence and mean precipitation rates for the different convection types from the 17th of February 1997 00 UTC to the 18th of February 1997 00 UTC simulated with $REMO_{standard}$ in $\frac{1}{6}^\circ$ resolution.

In this work, the North Atlantic cyclone *Caroline* has been simulated with $REMO_{standard}$ and $REMO_{cold}$ each in the double nesting procedure introduced in section 5.1. The analyses presented on the following pages are all based on the simulations with $\frac{1}{6}^\circ$ horizontal resolution with $REMO_{standard}$ and $REMO_{cold}$ (simulations *Caro 1* $\frac{1}{6}^\circ$ and *Caro 2* $\frac{1}{6}^\circ$ in table 5.1). Main focus of the investigations will be on the observed postfrontal precipitation and on its representation in both model versions. The model simulation domain for the $\frac{1}{6}^\circ$ simulations is shown in figure 5.3 where additionally the simulated sea ice edge for the 17th of February 09:00 UTC is marked.

For the $REMO_{standard}$ simulation, the frequency of occurrence for each convection type has been determined for the 17th of February 1997 (17th of February 00 UTC to 18th of February 00 UTC). In table 5.2, the percentage of occurrence for each convection type with respect to the total number of convective events is given. Additionally, the mean precipitation rate for the different convection cases is depicted. In addition to the mean percentage of occurrence given in table 5.2, the spatial distribution of the frequency of occurrence for *shallow convection* is shown in figure 5.4. The region of interest behind the front is marked by a black diamond. The precipitation behind the front, which is mostly produced by the convection scheme of the model is mainly connected to convection type *shallow convection*, which is associated with relatively small precipitation rates (see table 5.2). In this region, up to 75% of the convective activity is identified as *shallow convection* by the model, caused by the fact that strong moisture fluxes from the sea surface are the triggering mechanism for *shallow convection* defined in the Tiedtke convection scheme (see section 3.2.2). The introduction of the new convection type *cold convection* results in a redistribution of the convective types in the $REMO_{cold}$ simulation as shown in table 5.3. The *cold convection*, which is also activated when surface evaporation

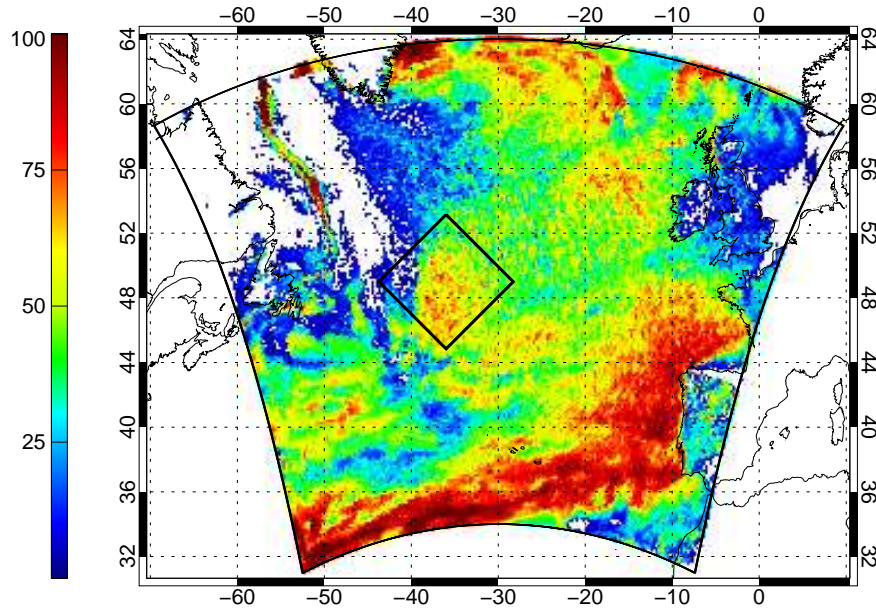


Figure 5.4: Frequency of occurrence [%] for convection type *shallow convection* for the 17th of February 1997 simulated with $REMO_{standard}$ in $\frac{1}{6}^\circ$ horizontal resolution.

provides the lower atmosphere with moisture (see section 4.2), takes over large parts of what has been *shallow convection* before. Due to the conversion factor for precipitation applied to *cold convection* (introduced in section 4.2), *cold convection* has larger precipitation rates than *shallow convection*. Figure 5.5 and figure 5.6 oppose the accumulated precipitation for the 17th of February for $REMO_{standard}$ (left) and $REMO_{cold}$ (right) for convective and total precipitation respectively. Both figures show the strong increase in postfrontal precipitation with $REMO_{cold}$, which is, according to figure 5.5, mainly caused by the increasing convective precipitation. To

$REMO_{cold}$	penetrative	midlevel	shallow	cold
Percentage of occurrence	1.4 %	40.5 %	41.2 %	16.9 %
Mean precipitation rate	$0.72 \frac{mm}{h}$	$0.07 \frac{mm}{h}$	$0.12 \frac{mm}{h}$	$0.25 \frac{mm}{h}$

Table 5.3: Percentage of occurrence and mean precipitation rates for the different convection types from the 17th of February 1997 00 UTC to the 18th of February 1997 00 UTC simulated with $REMO_{cold}$ in $\frac{1}{6}^\circ$ horizontal resolution.

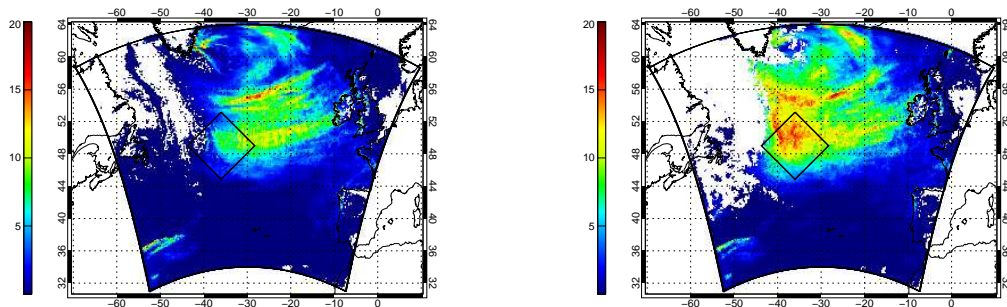


Figure 5.5: Precipitation from convection scheme [mm/24h], 17th of February 1997 for *REMO_{standard}* (left) and *REMO_{cold}* (right).

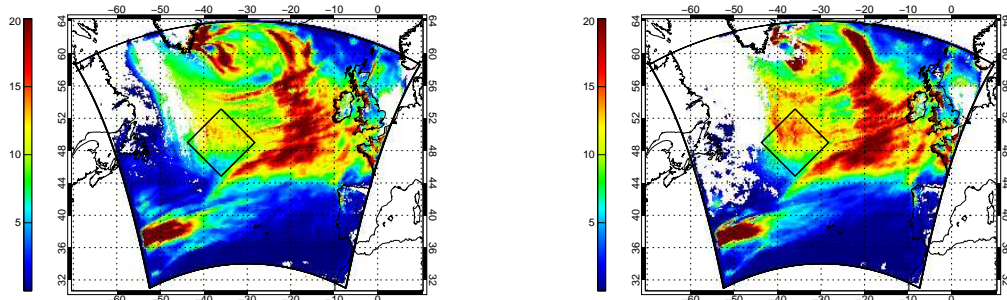


Figure 5.6: Total precipitation [mm/24h], 17th of February 1997 for *REMO_{standard}* (left) and *REMO_{cold}* (right).

be able to compare the simulation results of *REMO_{standard}* and *REMO_{cold}* to the derived precipitation values of Klepp et al., the simulated hourly precipitation fields have been classified as being frontal or postfrontal precipitation. The results of this manual classification are shown in table 5.4. Listed are the values determined for *REMO_{standard}*, for *REMO_{cold}* and those derived by Klepp from SSM/I satellite observations for the 17th of February 1997 (morning). For different reasons, the values simulated by the model and the values derived by Klepp are not entirely comparable. First, the satellite image represents a composite of different satellite overpasses, each catching an instantaneous image of the situation. The composites are composed of data from the three SSM/I orbiters F10, F11 and F13, which each pass the North Atlantic in four orbits in the morning and additional four overpasses in the evening (for details see Klepp 2001 [31]). This composite is only qualitatively comparable with the mean hourly values derived from the REMO simulations. Second,

Contribution to total precipitation [%]		
	Postfrontal area	Frontal system
<i>REMO_{standard}</i>	44 %	56 %
<i>REMO_{cold}</i>	53 %	47 %
SSM/I	60 %	40 %

Table 5.4: Contribution of the frontal system and the postfrontal area to the total precipitation on the 17th of February 1997 between 04 a.m and 02 p.m. Results from *REMO_{standard}* and *REMO_{cold}* are compared to values derived by Klepp (2001 [31]) for the morning of the 17th.

the method of classifying precipitation in frontal and postfrontal parts is different, again allowing only for qualitative comparison. For these reasons, the partitioning of precipitation in frontal and postfrontal (compared in table 5.4) is interesting not in terms of quantities of precipitation, but in the relation of frontal to postfrontal precipitation. Klepp concluded from his investigations that in the mature stage of *Caroline*, the postfrontal precipitation accounts for 60 % of the total precipitation of the cyclone. This value is nearly reached by the *REMO_{cold}* simulation with a value of 53% of postfrontal precipitation at this time, but was definitely underestimated by *REMO_{standard}* with only 44 % of postfrontal precipitation.

In conclusion, it can be stated that *REMO_{cold}* with the extension of the convection scheme to extratropical cold convection is able to simulate the presented postfrontal precipitation related to the cold air outbreak on the backside of the North Atlantic cyclone *Caroline* better than *REMO_{standard}*.

5.3 Simulation of European climate

For European climate, simulations covering the time period from 1999 to 2003 have been conducted. This period has been chosen in order to benefit from the extensive model validation effort undertaken in the BMBF funded project BALTIMOS (*Development and Validation of a Coupled Model System in the Baltic Region*). In the context of this project, satellite derived cloud and atmospheric properties have been processed and interpolated to the REMO model domain and resolution. They are now available for model validation on a $\frac{1}{6}^\circ$ grid for the years 2001 to 2003. Additionally, temperature observations from the *Climate Research Unit* (CRU) dataset (New et al., 1999 [44]) and precipitation observations from the Global Precipitation Climatology Center (Rudolf et al., 2003 [60]) have been used for model validation. To account for the time the model needs to produce an equilibrium for soil temperature and soil moisture after being initialized (the soil *spin up time*, which can take a few seasons to years (e.g. Giorgi and Mearns, 1999 [16])), the $\frac{1}{2}^\circ$ simulations have been initialized with soil fields from another simulation that already has been run for several years.

The orography of the $\frac{1}{2}^\circ$ and the $\frac{1}{6}^\circ$ model domains is shown in figure 5.7, where additionally sub-areas are highlighted that will be used for model comparison in the following sections. The sub-areas are the following:

1. The Baltic Sea catchment (referenced as *Baltex*)
2. The Danube catchment (referenced as *Danube*)
3. Germany (referenced as *Germany*)

In the following sections, simulations with $REMO_{cold}$ $\frac{1}{6}^\circ$ and $REMO_{standard}$ $\frac{1}{6}^\circ$ (*Baltic 1* $\frac{1}{6}^\circ$ and *Baltic 2* $\frac{1}{6}^\circ$ in table 5.1) will be compared for the liquid water and ice content (section 5.3.1), for precipitation (section 5.3.2), the integrated water vapor (section 5.3.3), total cloud fraction (section 5.3.4), mean sea level pressure (section 5.3.5) and for temperature (section 5.3.6). Validation of the model results has been carried out for those parameters that were available as observations.

In the following analyses, the internal variability of the model will be addressed more than once. Therefore, this term should be explained here: Generally, changes

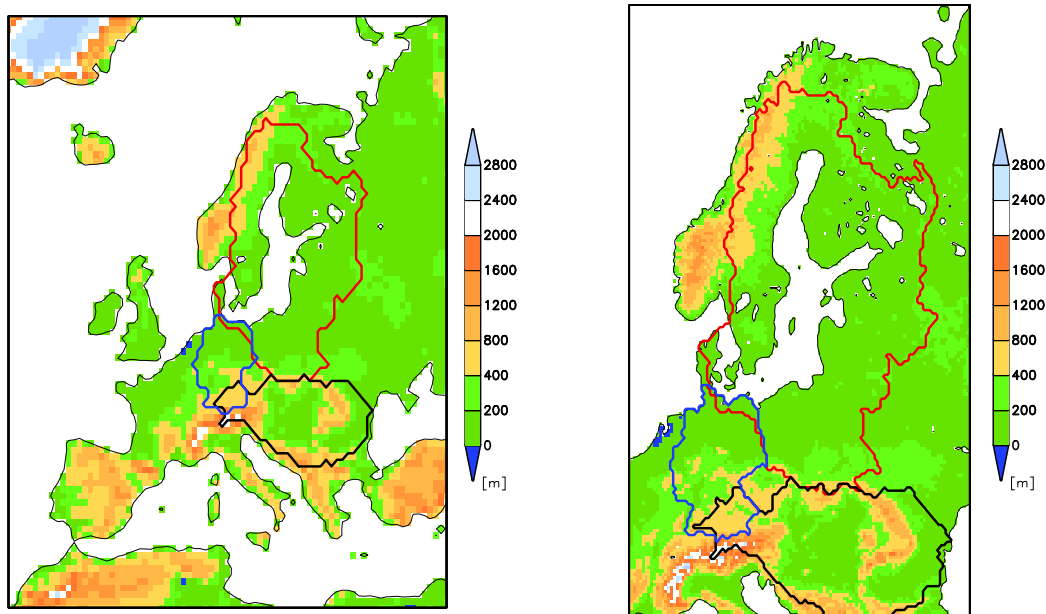


Figure 5.7: Orography of the model domain in $\frac{1}{2}^\circ$ horizontal resolution (left) and in $\frac{1}{6}^\circ$ horizontal resolution (right) [m]. Highlighted are the sub-domains *Baltic Sea*, *Germany*, and *Danube*.

between the climate simulations may not only result from changes in the parameterizations, but also from the nonlinearity of the governing equations, which can lead to distinct differences in the simulated climate conditions caused by only small initial differences in the atmospheric variables.

In the context of regional climate modeling and especially in the field of cloud modeling, internal variability should be more pronounced in summer than in the other seasons, as the regional model then is less affected and constrained by the large-scale circulation than in winter and autumn.

5.3.1 Liquid water and ice

In *REMO_{standard}*, cloud ice is diagnosed internally and is not a standard model output variable. For this reason, the following post processing has been accomplished to allow for comparison of this variable: For the *REMO_{standard}* simulation, atmospheric ice content has been calculated according to equation 3.1 for each grid box on a 6-hourly basis. From the resulting 3-dimensional ice and liquid water fields, vertically integrated liquid water and ice content have been derived. The 3-dimensional fields of ice and liquid water prognosed in the *REMO_{cold}* simulation also have been integrated vertically every 6 hours.

Figure 5.8, 5.9, and 5.10 show the annual cycle of vertically integrated ice content (qi_{vi}), vertically integrated liquid water content (ql_{vi}) and vertically integrated total water content ($qi_{vi} + ql_{vi}$). Shown are area-averaged values for the two catchments and Germany introduced in section 5.3 as well as area-averaged over the entire simulation domain (referenced as *Europe*).

As for the global circulation model ECHAM4 (see section 4.1), the introduction of the modified cloud parameterization results in a distinct increase in the vertically integrated ice content (see figure 5.8), especially for the winter months. This can be observed for all areas. For *Europe*, the vertically integrated ice increases by 25% in July and by up to 73% in January. For late autumn, winter and early spring, this increase is balanced by a decreasing vertically integrated liquid water content in the *REMO_{cold}* simulation, shown in figure 5.9. For all areas, vertically integrated liquid water is remarkably lower in winter, spring and partially also in autumn, whereas a rise can be observed for the summer months (also for all areas, lowest in the Danube catchment). Consequently, vertically integrated total water (see figure 5.10) experiences a decrease in winter and early spring, dominated by the strong decrease in the liquid water component, and an increase in summer and early autumn, due both to liquid water and ice increases. Possible reasons for this will be discussed later in this section.

The changes in vertically integrated liquid water and ice content can also be observed in the vertical distribution of liquid water and ice in the atmosphere. Seasonal mean values have been calculated for the three-dimensional fields of cloud liquid water and cloud ice.

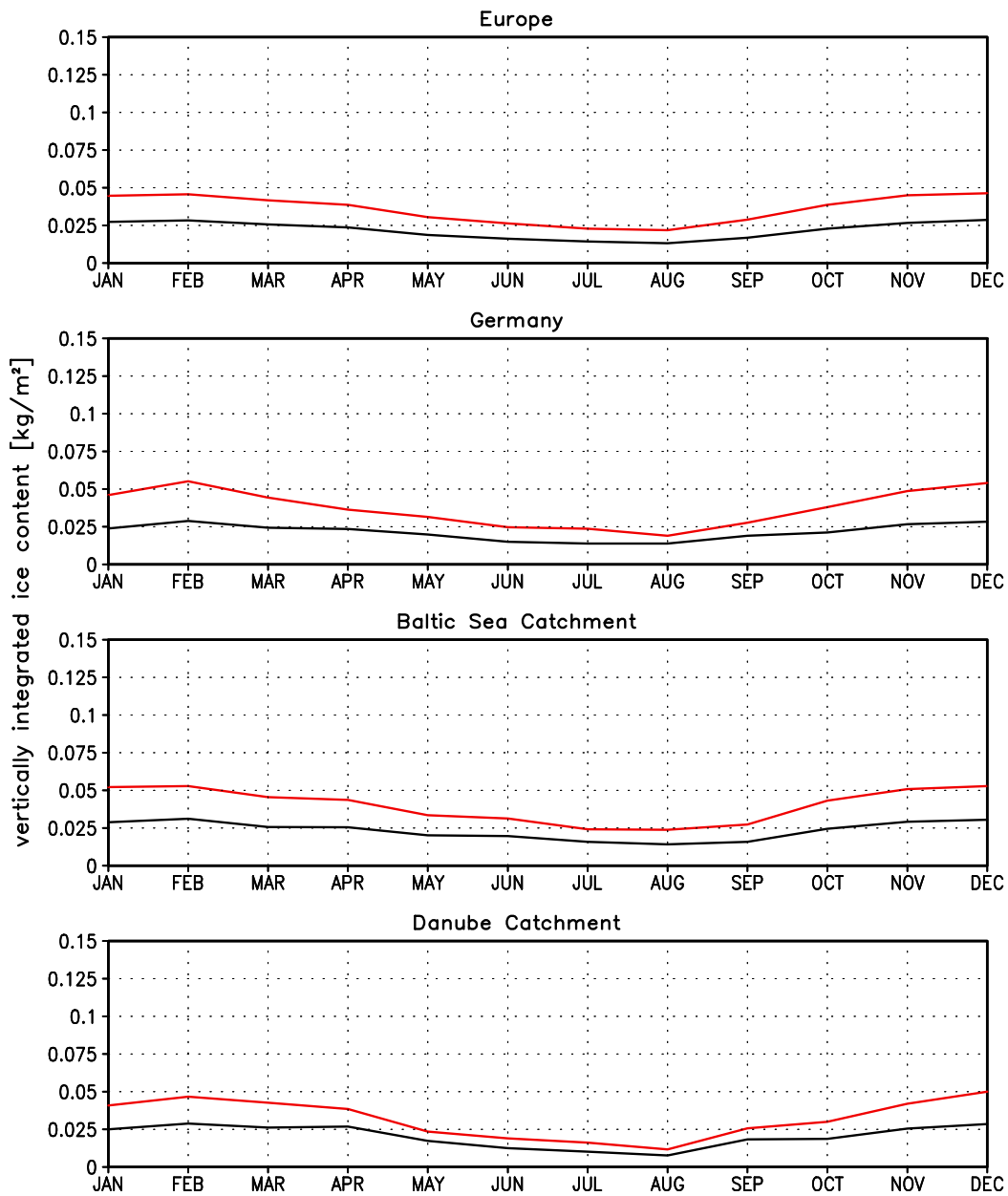


Figure 5.8: Mean annual cycle of vertically integrated ice content [kg/m^2] (1999 to 2003) for *REMO_standard* (black line) and *REMO_cold* (red line) both with $\frac{1}{6}^\circ$ horizontal resolution in different sub-areas of the model simulation domain.

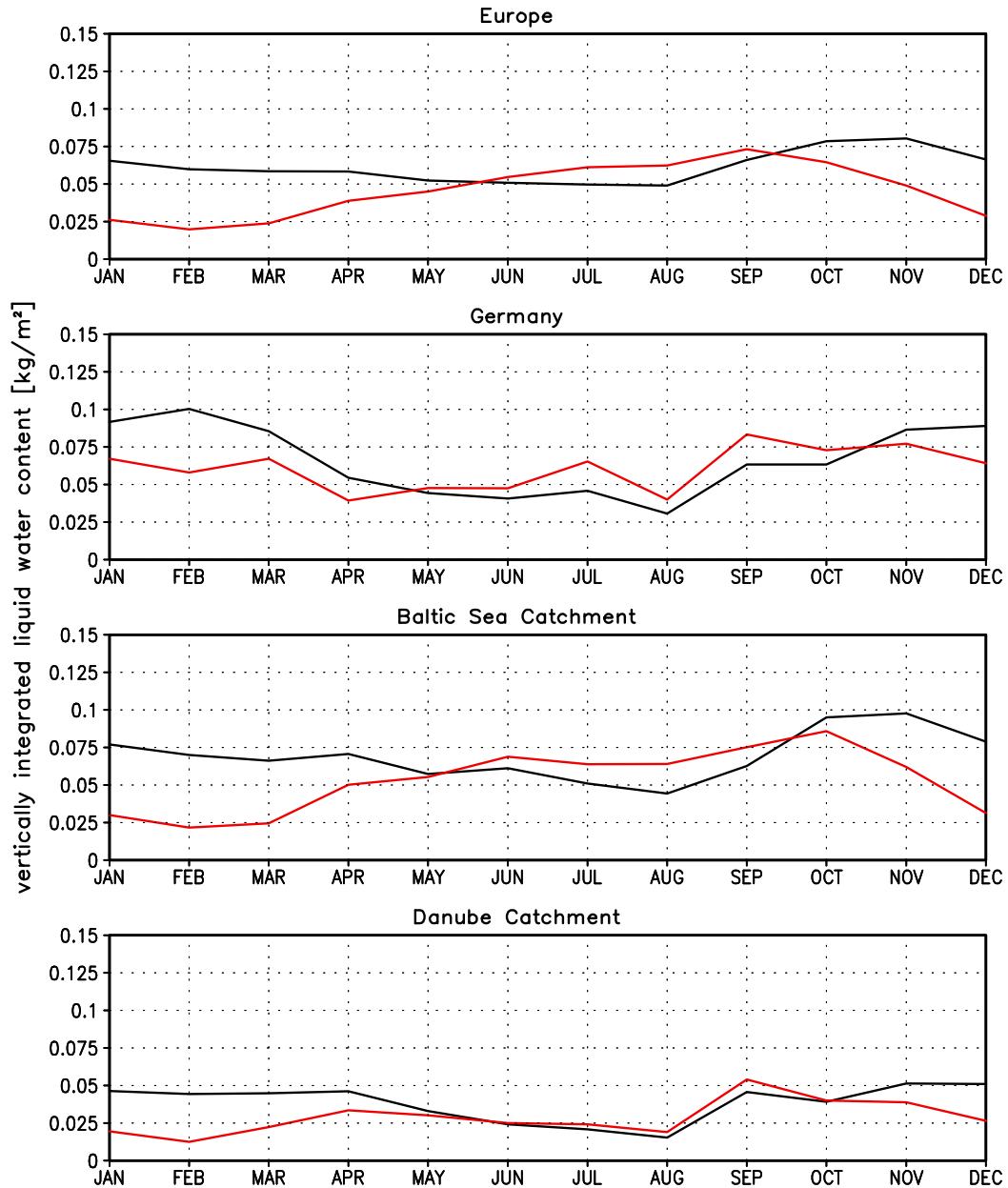


Figure 5.9: Mean annual cycle of vertically integrated liquid water content [kg/m^2] (1999 to 2003) for *REMO_standard* (black line) and *REMO_cold* (red line) both with $\frac{1}{6}^\circ$ horizontal resolution in different sub-areas of the model simulation domain.

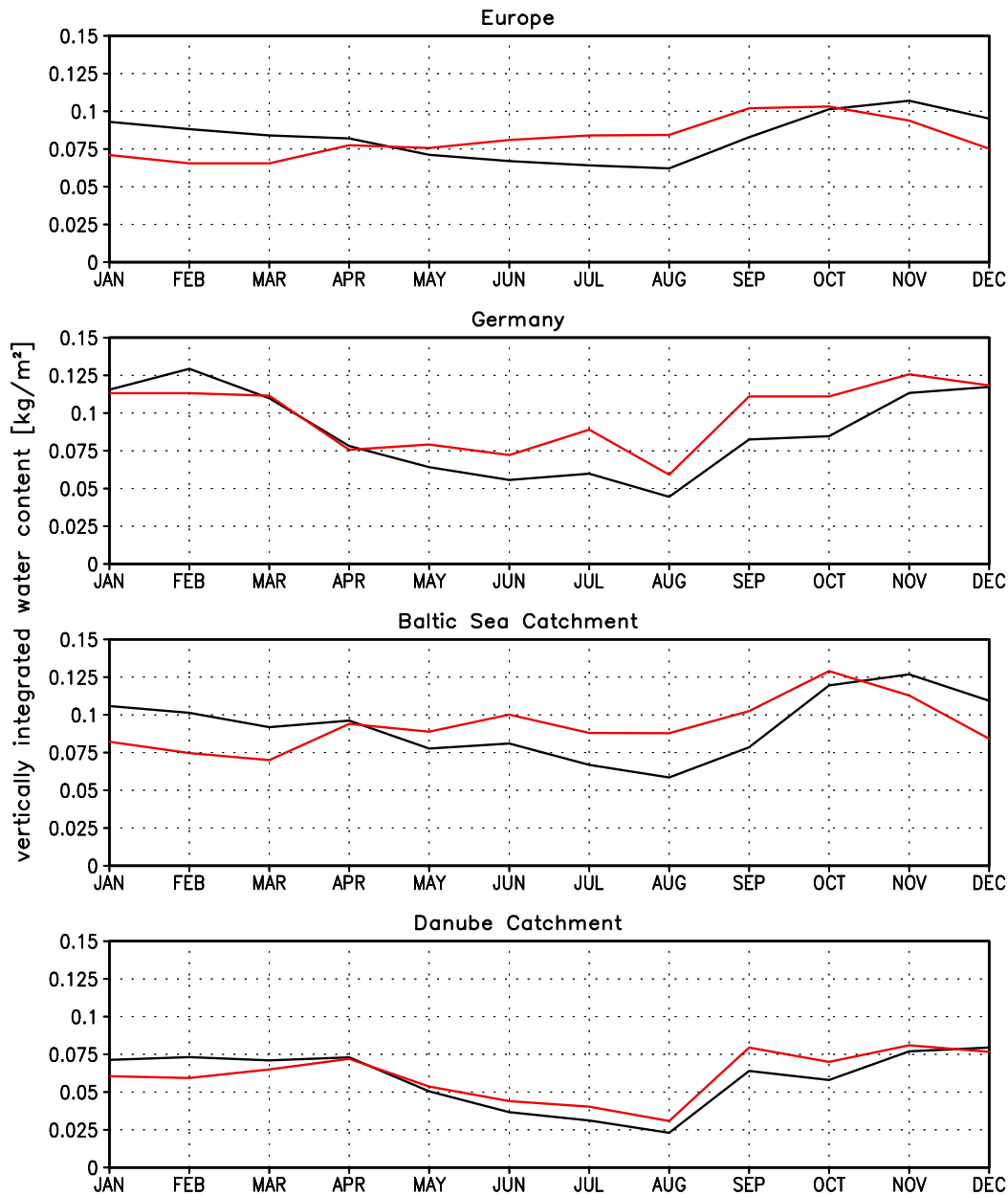


Figure 5.10: Mean annual cycle of vertically integrated water content (liquid water and ice) [kg/m^2] (1999 to 2003) for $REMO_{standard}$ (black line) and $REMO_{cold}$ (red line) both with $\frac{1}{6}^\circ$ horizontal resolution in different sub-areas of the model simulation domain.

To get an impression of the vertical distribution of cloud liquid water and cloud ice, *quasi-zonal means* have been generated. For the *quasi-zonal means*, the three-dimensional fields on the hybrid model levels have been averaged along the model grid in x-direction. As a result of the rotation of the model grid (see section 5.1), this averaging does not strictly follow the geographic latitudes, although it still roughly represents a north-south transect of the model simulation domain. This representation of the vertical structure of atmospheric variables is not recommended for the comparison of model results to observations, as the altitude of the model levels depends on surface pressure and is therefore not constant in time and space (see section 3.1). It should therefore only be used in model-to-model comparisons as presented here. This *quasi-zonal mean* is illustrated in figure 5.11 for the cloud liquid water content and in figure 5.12 for the cloud ice content. On the vertical axis are the hybrid model levels, numbered in descending order, starting by level No. 20 at the surface and ending with level No. 1 at the top of the atmosphere. The upper panels refer to summer means and the lower panels to winter means. Compared are $REMO_{standard}$ on the left to $REMO_{cold}$ on the right. For the summer season, both simulations show the largest liquid water contents in the northern part of the simulation domain, whereas liquid water in winter has maximum values confined to warmer regions more in the southern part of the simulation domain (figure 5.11). The differences between $REMO_{standard}$ and $REMO_{cold}$ also become evident in figure 5.11: A large decrease in liquid water content in the winter months, that already has been stated in the context of the annual cycles of liquid water content can be observed (figure 5.9). The same is true for the increasing liquid water content in the summer months. Furthermore, the maximum height for liquid water in the $REMO_{cold}$ simulation seems to be restricted to lower atmospheric levels than it is the case for the $REMO_{standard}$ simulation. This can be seen both in the summer and the winter panels of figure 5.11. This shift in maximum heights cannot be seen for the cloud ice component (figure 5.12), which however occupies lower atmospheric levels in $REMO_{cold}$ than in the $REMO_{standard}$ simulation. Additionally, cloud ice in $REMO_{cold}$ experiences dramatical changes in its amount especially in the winter atmosphere (see the lower panels of figure 5.12). As these changes are not coinciding with analogous changes in the vertical temperature distribution (which

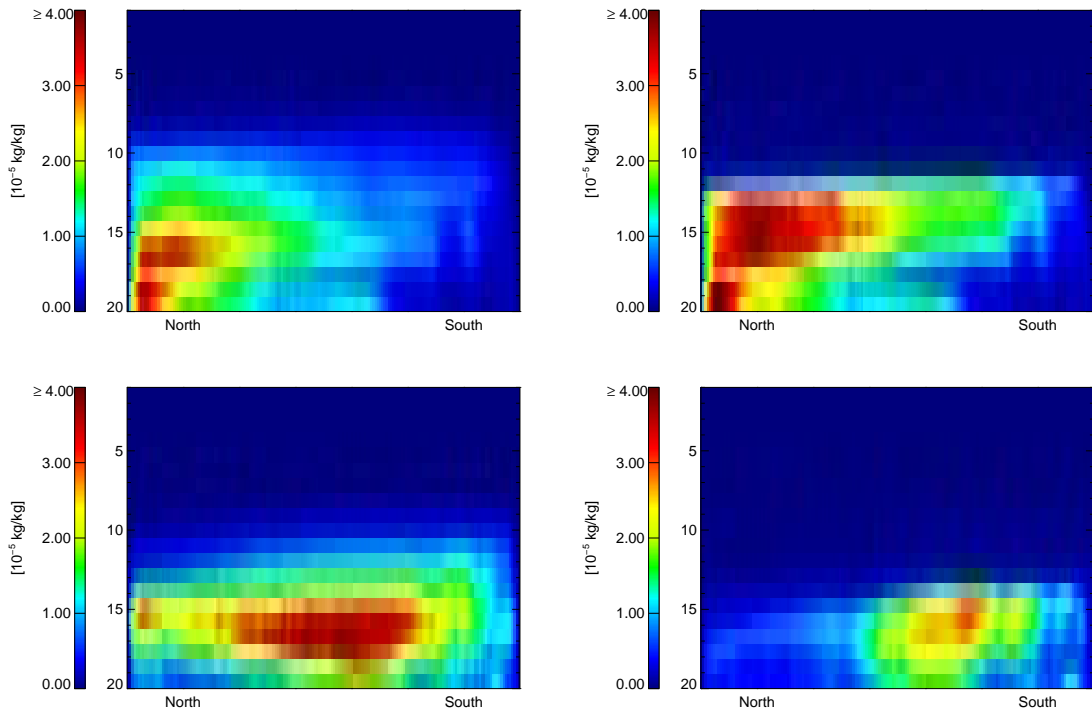


Figure 5.11: *Quasi-zonal mean* liquid water content for $REMO_{standard}$ (left) and $REMO_{cold}$ (right) in $[10^{-5}kg/kg]$ for the 20 vertical levels. Summer mean (upper panels) and winter mean (lower panels) of 1999 to 2003 in $\frac{1}{6}^{\circ}$ horizontal resolution.

will be shown in section 5.3.6 and illustrated in figure 5.28), the reason for these large differences must be related to cloud ice fraction as a function of temperature.

To assess the mean cloud ice and cloud liquid water fractions with respect to temperature for $REMO_{cold}$ and $REMO_{standard}$, mean cloud liquid water fractions have been calculated in the following way: For $REMO_{standard}$, the diagnostic relation given in equation 3.1 has been applied. For $REMO_{cold}$, the liquid water fraction has been calculated as $f_{liq} = \frac{q_{cl}}{q_{cl} + q_{ci}}$ for every grid box where the cloud fraction exceeds a threshold value of 0.01, i.e. 1 % of the grid box has at least to be cloud covered. These liquid water fractions are then weighted by the cloud coverage of the respective grid box to assure that very small clouds are not overinterpreted. Temperature bins in the range of $-50^{\circ}C$ to $10^{\circ}C$ have been defined. The calculated cloud liquid water fractions have been sorted into the bins and have been averaged for each temperature bin. The result is a mean relation between temperature and

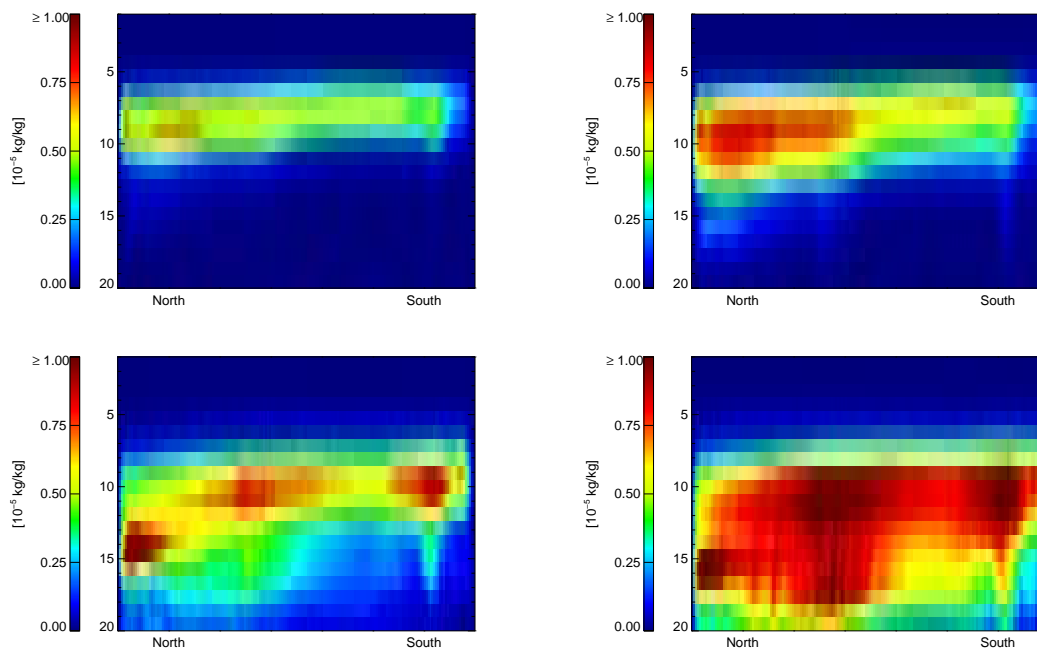


Figure 5.12: Quasi-zonal mean ice content for $REMO_{standard}$ (left) and $REMO_{cold}$ (right) in $[10^{-5} \text{ kg/kg}]$ for the 20 vertical levels. Summer mean (upper panels) and winter mean (lower panels) of 1999 to 2003 in $\frac{1}{6}^\circ$ horizontal resolution.

cloud liquid water fraction, which can be displayed in the same way as the diagnostic ice fraction in figure 3.3. Both the diagnostic liquid water fraction of $REMO_{standard}$ and the prognostic liquid water fraction of $REMO_{cold}$ are displayed in figure 5.13 for the year 1999. It is obvious, that $REMO_{cold}$ (shown as red line) simulates much lower amounts of supercooled water in the temperature range of -5°C to -25°C than the diagnostic relation (blue line) assumes to be present. To help judging the realism of both simulation results, the curves have been drawn in a figure taken from Bower et al. (1996, [8]), which shows measured values of liquid cloud fraction for frontal clouds in continental airmasses (crosses), maritime airmasses (squares) as well as the linear best fit to those two data-sets (dotted line: linear best fit to continental clouds, dashed line: linear best fit to maritime clouds). The solid black line indicates the parameterization of liquid fraction as it was used in the UK Meteorological Office atmospheric global climate model at the time of the publication of the article. Although the simulated liquid water fraction with $REMO_{cold}$ seems to

be a little higher at low temperatures and somewhat lower in the higher temperature range than the observations are, it is obvious that the former parameterization as used in *REMO_{standard}* results in overestimated supercooled liquid water in clouds at basically all temperatures. As mentioned by Bower et al. (1996, [8]) as well as in Rotstayn et al. (1999, [57]), high values of liquid fraction at temperatures below $-15\text{ }^{\circ}\text{C}$ are typically observed in convective clouds rather than in frontal stratiform cloud systems.

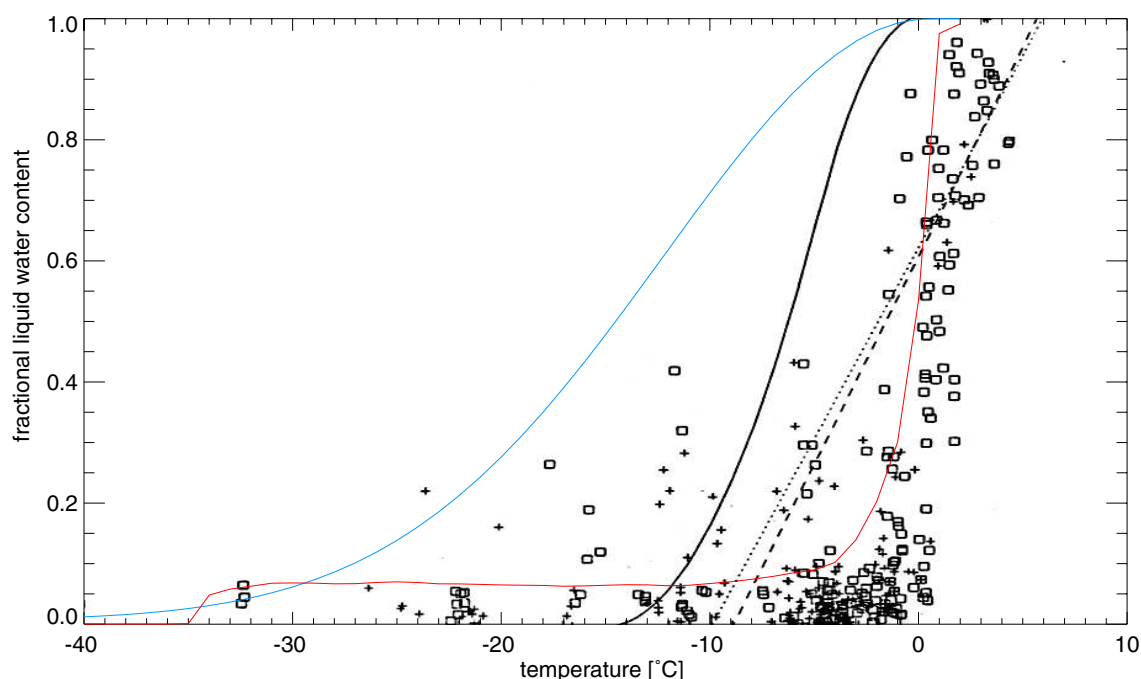


Figure 5.13: Variation of the cloud liquid water fraction with temperature. Figure reproduced from Bower et al. (1996, [8]). Black: liquid fraction obtained from aircraft observations as described by Bower et al. Crosses indicate clouds in continental airmasses, squares clouds in maritime airmasses, The dotted line is the best-fit line to the data for continental clouds, the dashed line for maritime clouds. The solid line is an example for the parameterization of liquid fraction in the UK meteorological Office atmospheric global climate model. Blue: parameterization of the liquid fraction in *REMO_{standard}* as given in equation 3.1. Red: mean liquid fraction as simulated by *REMO_{cold}* for 1999 in $\frac{1}{6}^{\circ}$ resolution.

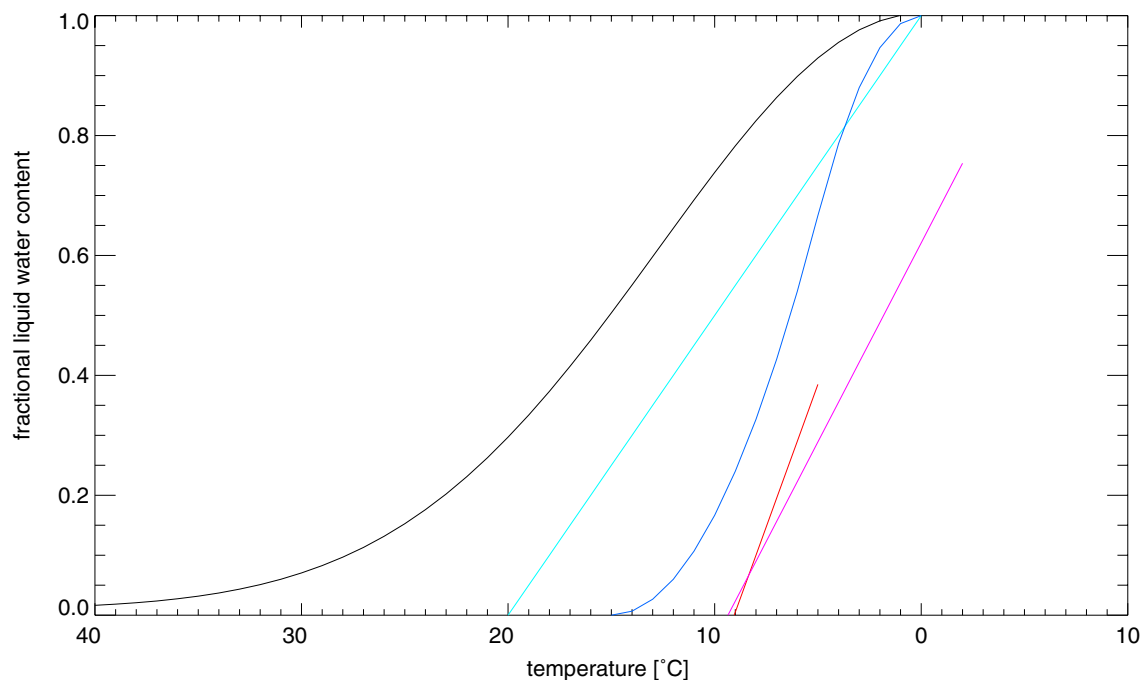


Figure 5.14: Variation of the cloud liquid water fraction with temperature according to different parameterizations for mixed phase clouds: black line: following Rockel et al. (as used in *REMO_{standard}*). Light blue: following Rasch and Kristjansson (1998, [49]), also used in the NCEP GFS model. Dark blue: following Smith (1990, [62]). Red line: following Moss and Johnson (1994, [41]). Purple: following Bower et al. (1996, [8]).

A relatively wide range of possible parameterization of cloud liquid fraction is existing. Some of them are presented in figure 5.14. The parameterization used in *REMO_{standard}* (black line) clearly is an outlier, giving by far the highest values of liquid fraction. Consequently, one can conclude that the large changes in simulated cloud phase occurring with *REMO_{cold}* indicate a more realistic simulation of cloud phase with *REMO_{cold}* than with *REMO_{standard}*.

The validation of the simulated cloud phase has been accomplished on the basis of a single set of observations (Bower, 1996 [8]). A more comprehensive validation of simulated cloud phase on longer time scales covering larger areas is not yet possible because of the lack of observational data. Up to now, satellite-derived cloud phase products are restricted to cloud top values, limiting the validation to this special case. Furthermore, common algorithms are based on assumptions that are as simple

as those used in some models (e.g. the derivation of cloud top phase from cloud top temperature, assuming threshold values for the fraction of glaciation) or have large uncertainty ranges. Another difficulty when comparing model-simulated cloud properties to satellite-derived cloud top values is that it first has to be investigated, whether the model and the satellite are addressing the same clouds. If e.g. the comparison of cloud top phase from model simulations and satellite observations results in the statement that the model simulates more ice clouds than seen by the satellite, the reasons could be the wrong cloud microphysics, resulting in too strong glaciation of clouds. As well, the result can be caused by the fact, that clouds in the model are located systematically at higher altitudes than the clouds seen by the satellite, thus experiencing lower temperatures. A third possible explanation for the observed mismatch in cloud phase could be the flawed representation of the vertical temperature structure of the modeled atmosphere.

Validation would thus be easier with observed vertical structures of clouds, allowing for the validation not only of cloud top values, but also of profiles inside the cloud layer. This will be possible for CloudSat, an experimental satellite that will use radar to measure the vertical structure of clouds and cloud properties from space. Launch is planned for 2006 [11]. A validation of cloud phase and other cloud related parameters with products derived from CloudSat measurements should thus be undertaken as soon as CloudSat data are available.

Summarizing the results for liquid water and ice, the changes in the cloud microphysics result in an increase in vertically integrated total water in summer and a decrease of vertically integrated total water in winter, the cloud ice component increases throughout the year, whereas the liquid water component remarkably decreases in winter and only slightly increases in summer. The simulated cloud phase with respect to temperature seems to be simulated more realistically with *REMO_{cold}* than with *REMO_{standard}*.

5.3.2 Precipitation

Total precipitation has also been averaged for the four areas and is illustrated in figure 5.15. As could be expected, changes in the cloud parameterization of the model result in visible changes in simulated precipitation. Recalling again that *REMO_{cold}* simulates increasing total water content in summer, and decreasing total water content in winter, going along with an increasing cloud ice content over the whole year, these changes in liquid water should also be visible in changes of simulated precipitation. This will be examined in the following.

Averaged over the whole model simulation domain, the annual mean precipitation does not change much. In the mean annual cycle, summer precipitation increases and a slight decrease in winter precipitation can be observed (*Europe*, figure 5.15). The differences are larger for the smaller areas. For Germany, the simulation with *REMO_{cold}* results in an increase in summer precipitation by up to 9%. Largest changes in winter precipitation are seen in the Baltic Sea catchment as well as in the Danube catchment, where winter precipitation simulated with *REMO_{cold}* is reduced by 7 to 8%. In the context of changes in atmospheric liquid water, the decreasing winter precipitation is reflected in decreasing winter water contents of the atmosphere, and the increasing precipitation in summer goes along with increasing total water content of the summer atmosphere (section 5.3.1).

The contribution of the large-scale cloud scheme and the convection scheme to the total precipitation is shown in figure 5.16, where the convective component is drawn as solid line and the large-scale component is drawn as dashed line, again both for *REMO_{standard}* in black and *REMO_{cold}* in red. For all catchments, an increase in the convective component of the precipitation is only in parts compensated by the reduction of the large-scale precipitation component in summer. In the winter months, the reduction in the large-scale is dominating, resulting in the slight reduction of winter precipitation visible in the uppermost panel of figure 5.15.

The increase in the convective precipitation component is not caused by a higher frequency of convective events, but by an increase in the intensity of the single convective precipitation event.

To analyze changes in the precipitation intensities, hourly precipitation has been analyzed and subdivided into precipitation intensity classes. Histograms of precipitation intensities are displayed in figure 5.17 for a) total precipitation (upper panel),

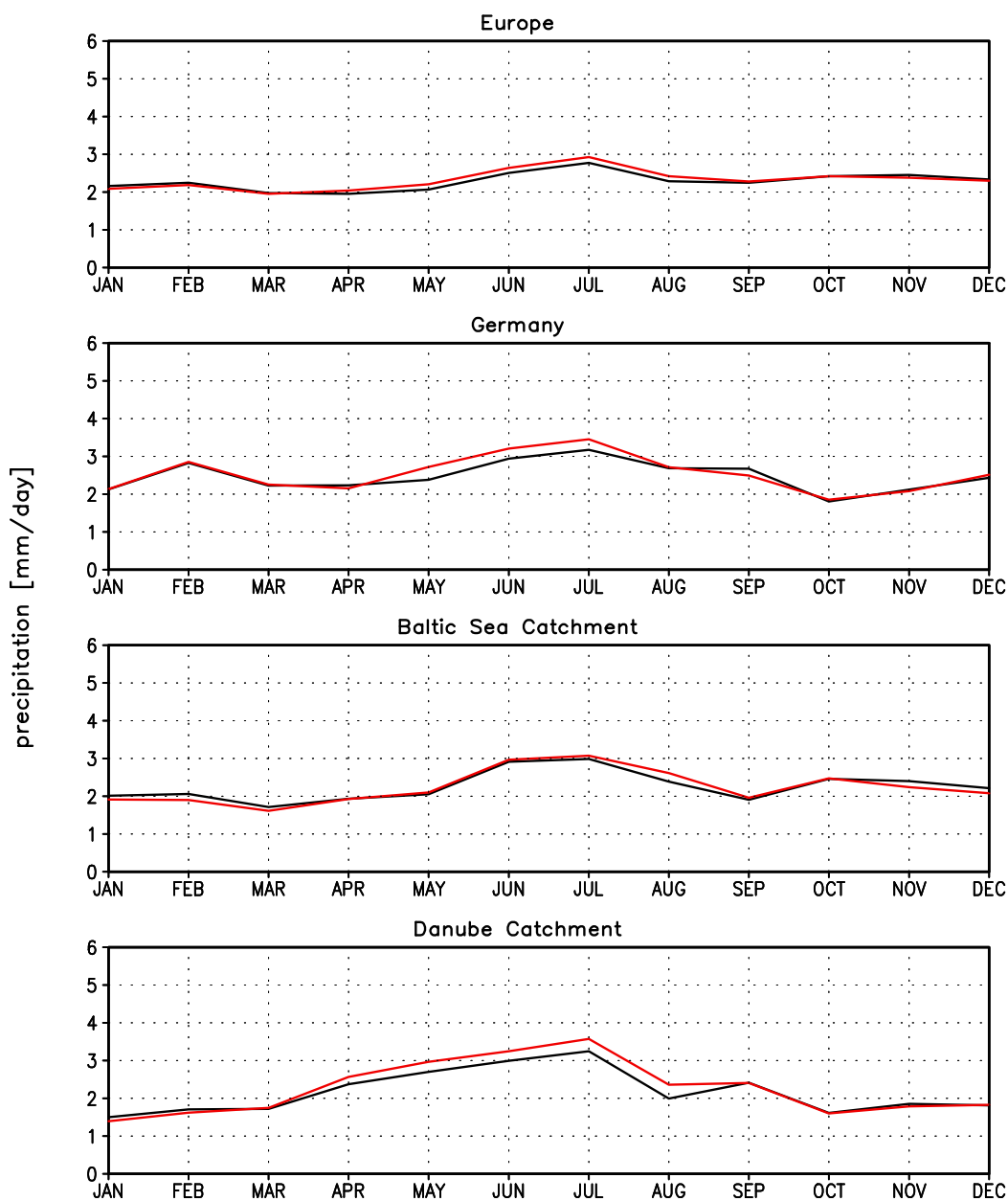


Figure 5.15: Mean annual cycle of precipitation [mm/day] (1999 to 2003) for $REMO_{standard}$ (black line) and $REMO_{cold}$ (red line) both with $\frac{1}{6}^\circ$ horizontal resolution in different sub-areas of the model domain.

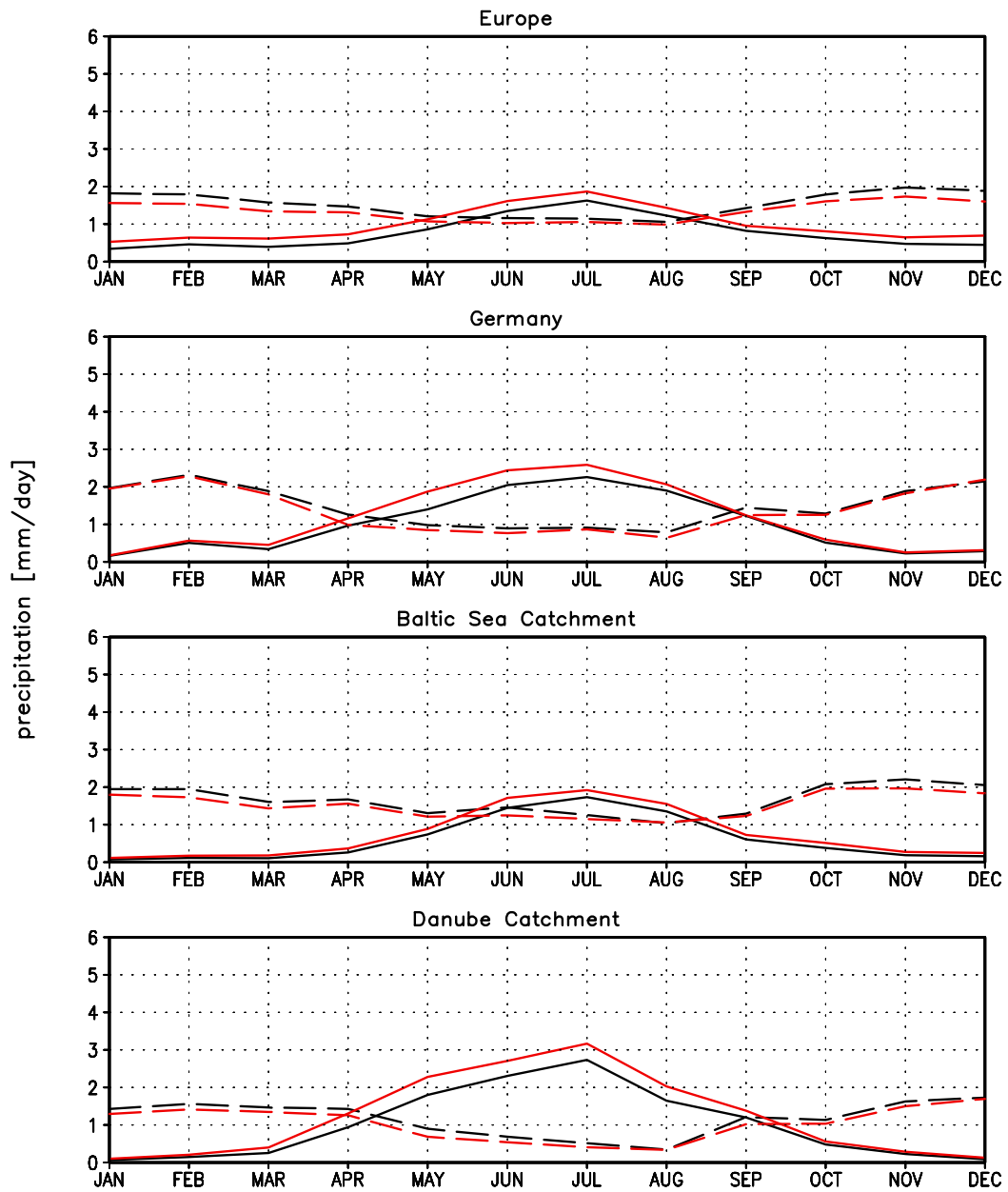


Figure 5.16: Mean annual cycle of precipitation components [mm/day] (1999 to 2003) for *REMO_standard* (black line) and *REMO_cold* (red line) both with $\frac{1}{6}^\circ$ horizontal resolution in different sub-areas of the model domain. Solid lines: precipitation from the convection scheme. Dashed lines: precipitation from the large-scale cloud scheme.

b) precipitation produced by the large-scale cloud scheme (middle panel), and c) precipitation produced by the convection scheme (lower panel) for the $\frac{1}{6}^\circ$ resolution simulations of *REMO_{standard}* and *REMO_{cold}*. The percentage of occurrence in the single intensity classes has been calculated with respect to the total number of precipitation events, given by N in all panels. All grid boxes have been used for the statistic, so that the first bin in the histograms in figure 5.17 groups all cases with intensities up to $0.05 \frac{mm}{h}$, including zero precipitation values. The y-axis is arranged logarithmic, ranging from 0.1% to 100%. The last bin in the precipitation intensities groups all precipitation values higher than $1.95 \frac{mm}{h}$. As such precipitation events do not occur very often, one would not see them as individual bins in the histograms. Only grouping reveals their contribution to the precipitation spectrum.

Generally, simulated precipitation intensities are distributed in such a way that the lower intensities are more frequent than the higher intensities. For the total precipitation, 78% (*REMO_{standard}*) respectively 79% (*REMO_{cold}*) of the grid boxes have no or very little precipitation. Precipitation intensities between $0.05 \frac{mm}{h}$ and $0.5 \frac{mm}{h}$ are present in approximately 16%, respectively 18% of the cases, whereas the high precipitation events ($> 1.5 \frac{mm}{h}$) only occur in less than 2% of all grid boxes. For *REMO_{cold}*, the distribution has a slightly lower slope, having less events in the lower classes (apart from the class including the zero-precipitation events) and higher frequencies of occurrence for the higher intensity classes. This is also the prominent feature of the intensities of the large-scale precipitation component. Here, the intensities below $1.4 \frac{mm}{h}$ occur more frequent in *REMO_{standard}* than in *REMO_{cold}* while intensities of more than $1.4 \frac{mm}{h}$ increasingly dominate in the *REMO_{cold}* simulation. For the convective precipitation, *REMO_{cold}* experiences higher frequencies of occurrence for the whole spectrum of intensity classes, explaining the strong increase in the convective precipitation seen in figure 5.16. Thus *REMO_{cold}* simulates generally stronger convective events than *REMO_{standard}* and also more high-intensity precipitation events of the large-scale component.

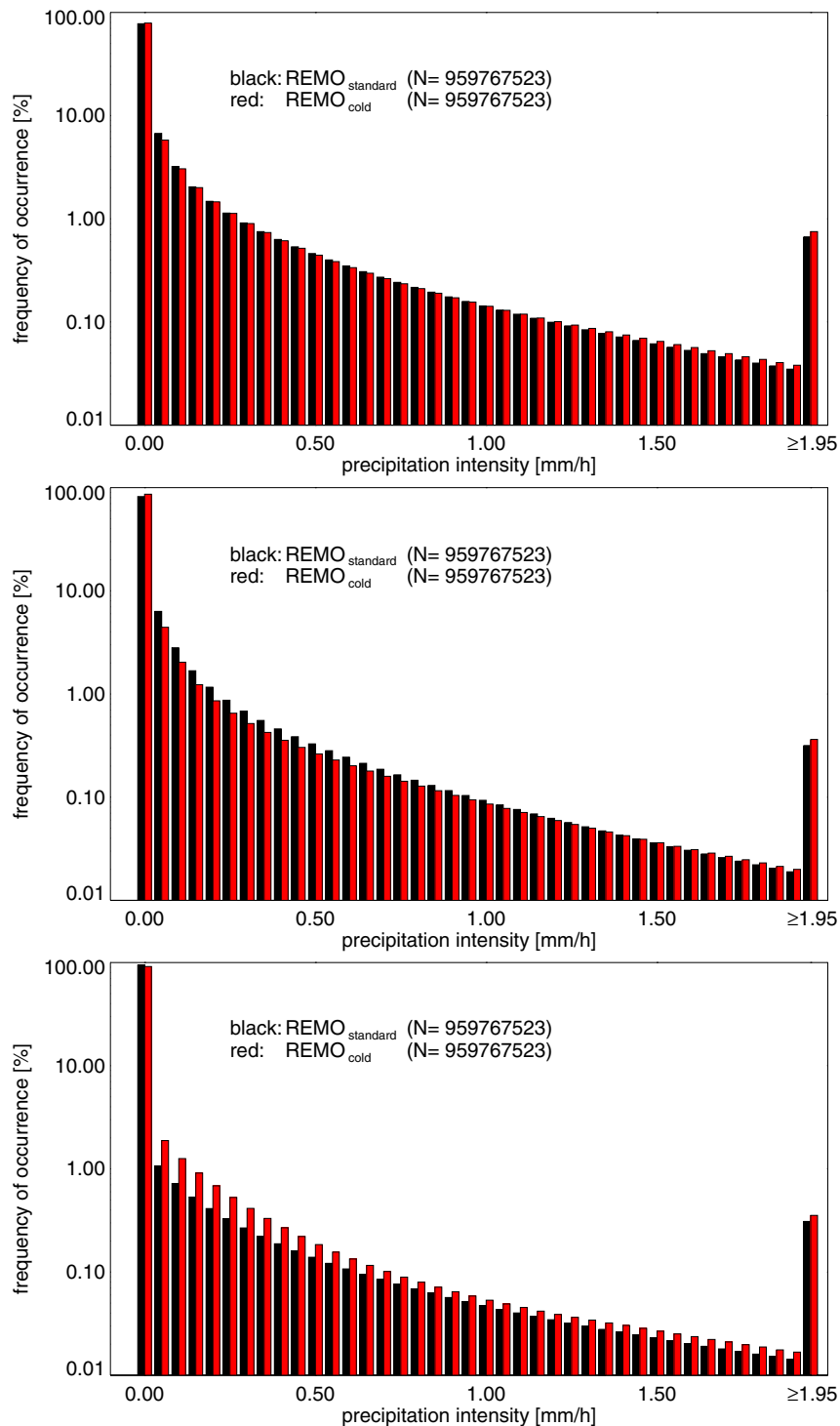


Figure 5.17: Histograms of hourly precipitation intensities for $REMO_{standard}$ (black) and $REMO_{cold}$ (white) for the years 1999 to 2003 for the simulations in $\frac{1}{6}^\circ$ horizontal resolution. Upper panel: total precipitation. Middle panel: precipitation from the large-scale scheme. Lower panel: precipitation from the sub-grid-scale scheme. The y-axis is arranged logarithmic.

		<i>REMO_{standard}</i>	GPCC	<i>REMO_{cold}</i>
Germany	mean	2.47	2.16	2.53
	stddev	0.85	0.80	0.88
	rmse	0.53		0.60
	correlation	0.86		0.84
Baltic Sea	mean	2.28	1.70	2.26
	stddev	0.67	0.60	0.74
	rmse	0.65		0.66
	correlation	0.90		0.89
Danube	mean	2.16	1.85	2.25
	stddev	0.82	0.77	0.96
	rmse	0.56		0.67
	correlation	0.81		0.83

Table 5.5: mean, standard deviation (stddev), root mean square error (rmse) in mm/day and correlation coefficient for the precipitation time series depicted in figure 5.18 for the $\frac{1}{6}^\circ$ resolution simulations of *REMO_{standard}* and *REMO_{cold}* and for the GPCC observations.

Simulated precipitation for the years 1999 to 2003 has been compared to observations from the Global Precipitation Climatology Center (GPCC, Rudolf et al., 2003 [60]), which is a German contribution to the World Climate Research Programme (WCRP) and to the Global Climate Observing System (GCOS). The GPCC data are gauge-based gridded precipitation values collected and interpolated to a $1^\circ \times 1^\circ$ grid and are not corrected for systematic measuring errors. Those systematic measurement errors are errors introduced by evaporation or condensation in the rain gauge and by mismeasurements due to aerodynamic turbulences around the rain gauge. To give an estimate of the size of the possible measurement bias, results of Rubel and Hantel, who designed a correction and analysis model for precipitation observations (Rubel and Hantel, 2001 [59]) are cited here: for the three year period of 1996 to 1998, they determined a mean aerodynamic correction factor (based on information on the weather event as wind speed and precipitation intensities as well as on specific information on the rain gauge) of 1.05 for the summer months and 1.25 for the winter months respectively. Thus the uncorrected GPCC observations are

probably also less reliable for winter than for summer. The comparison between observed and simulated precipitation is shown in figure 5.18 for the simulations with $\frac{1}{6}^\circ$ horizontal resolution. In addition to the time series plotted in figure 5.18, the mean value, the temporal standard deviation and the root mean square error as well as the correlation coefficient have been calculated for all time series on a monthly mean basis. The results are shown in table 5.5 for the $\frac{1}{6}^\circ$ simulations with *REMO_{standard}* and *REMO_{cold}*. In the context of the BALTIMOS project, the model quality target for simulated precipitation has been defined as $\pm 10\%$ deviation from observed values for the long term annual mean precipitation and $\pm 20\%$ for the long term monthly mean. From table 5.5, for the German sub-area, the 5-year annual mean simulated precipitation is by 14% overestimated for *REMO_{standard}* and by 17% for *REMO_{cold}*. All simulations are therefore outside the aspired accuracy, *REMO_{cold}* by a higher degree than *REMO_{standard}*. Similar results can be derived for the other sub-areas. From the time series in figure 5.18 it becomes clear, that the stronger deviation for *REMO_{cold}* is caused by the increasing summer precipitation, whereas the winter precipitation in *REMO_{cold}* is slightly closer to the observed values than in *REMO_{standard}*. This also becomes evident in the values of the standard deviation shown in table 5.5, which are larger for the *REMO_{cold}* simulation. This indicates that the higher mean values of precipitation with *REMO_{cold}* are not produced by a continuous increase in all seasons, but by a stronger increase in summer which cannot be compensated by the observed slight decrease in precipitation in winter. Summarizing, both model versions simulate too much precipitation compared to the GPCP precipitation observations. *REMO_{cold}* tends to worsen the problem in summer by simulating still more precipitation than *REMO_{standard}*, but reduces winter precipitation compared to *REMO_{standard}*. The intensity of single precipitation events is higher with *REMO_{cold}* than with *REMO_{standard}*. This is especially the case for convective summer precipitation.

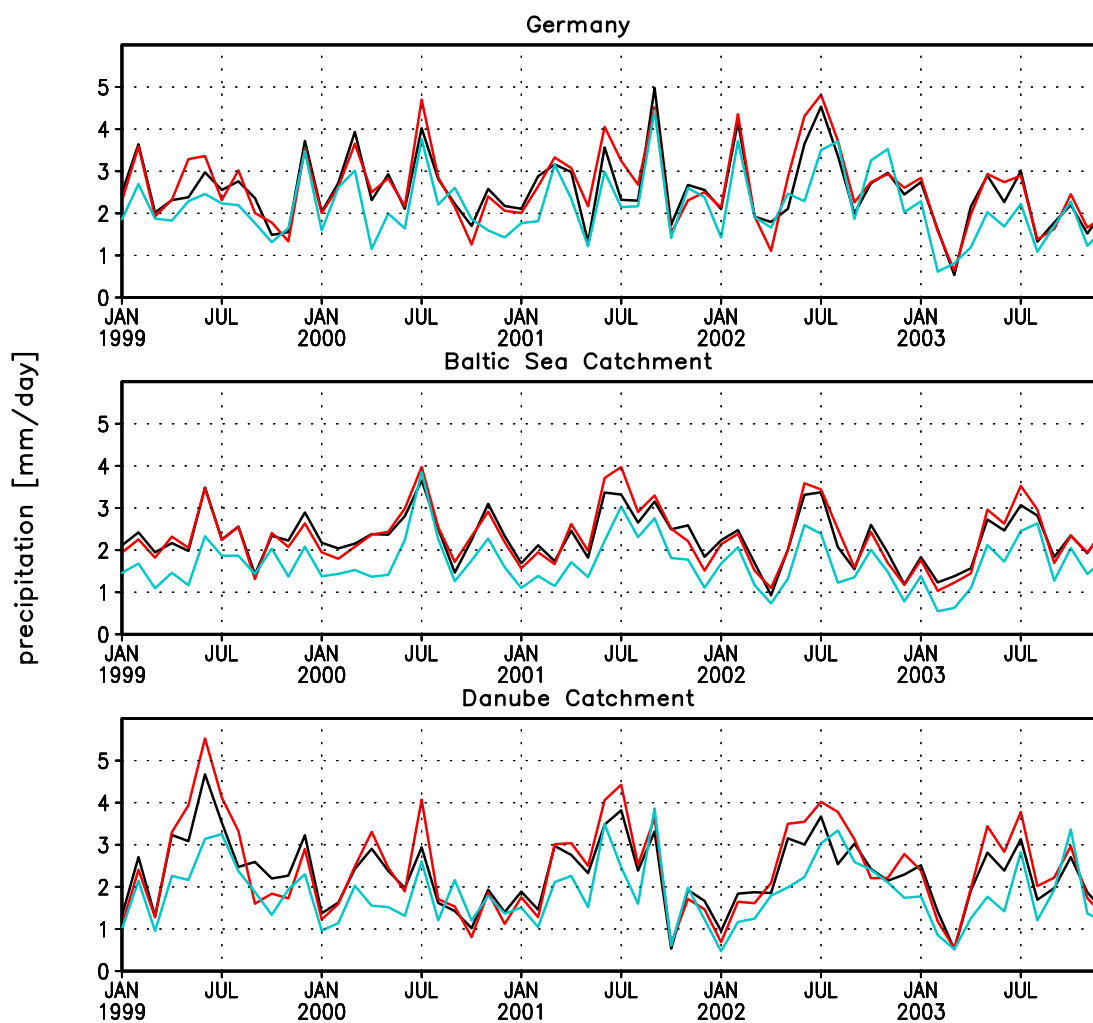


Figure 5.18: Mean precipitation [mm/day] from January 1999 to December 2003 for GPCC observations (blue line) compared to $REMO_{standard}$ (black line) and $REMO_{cold}$ (red line) both with $\frac{1}{6}^\circ$ horizontal resolution for different sub-areas of the model domain.

5.3.3 Integrated water vapor

Integrated water vapor (IWV) has been compared to observations that have been derived from satellite measurements in the context of BALTAMOS. The algorithm as well as the quality of the observation is described in Albert et al. (2005, [1]) and in Leinweber (2004 [34]). It is based on the *differential absorption technique* using water vapor absorption bands and adjacent window channels of the Moderate Resolution Imaging Spectrometer (MODIS), onboard the polar orbiting satellite TERRA. MODIS observations have been interpolated to the REMO $\frac{1}{6}^\circ$ grid. The algorithm to derive IWV from MODIS measurements only works over land surfaces. Water covered areas are thus a priori excluded. For the comparison of IWV derived from MODIS measurements with the REMO simulated values, only those grid boxes of both REMO and MODIS have been used that contained MODIS measurements, i.e. that were in the MODIS swath. Cloudy cases have been excluded by applying the respective cloud masks for MODIS and REMO separately (Leinweber, 2004 [34]).

Figure 5.19 shows the mean integrated water vapor for $REMO_{standard}$ from October 2001 to October 2003 in $[\frac{kg}{m^2}]$ (upper left panel). The upper right panel of figure 5.19 shows the differences between $REMO_{standard}$ and $REMO_{cold}$ ($REMO_{standard}$ minus $REMO_{cold}$) for the same period. Differences between the two model versions amount to 3 to 6 % at most, the largest changes occurring in the region of the Danube as well as north of the Carpathian Mountains, where IWV increases by up to $0.3 \frac{kg}{m^2}$. Slightly decreasing IWV values (in the order of $0.1 \frac{kg}{m^2}$) can be found for northern Germany and near the Gulf of Riga as well as over the Alps and in northern Italy. When comparing the inter-model differences to the differences between model simulation and observations (figure 5.19 lower panel) the difficulty in judging the changes introduced by the modified model physics becomes clear. The differences between satellite-derived IWV and modeled IWV are by a factor of 10 larger than the differences between the model versions. Although a visual comparison of the regional changes indicates that IWV simulated with $REMO_{cold}$ is in many regions closer to the observations than the $REMO_{standard}$ simulation (especially in the Danube region, where the well known *summer drying* problem occurs (Hagemann et al., 2002 [20])), the magnitude of the changes is much too low to interpret them as a

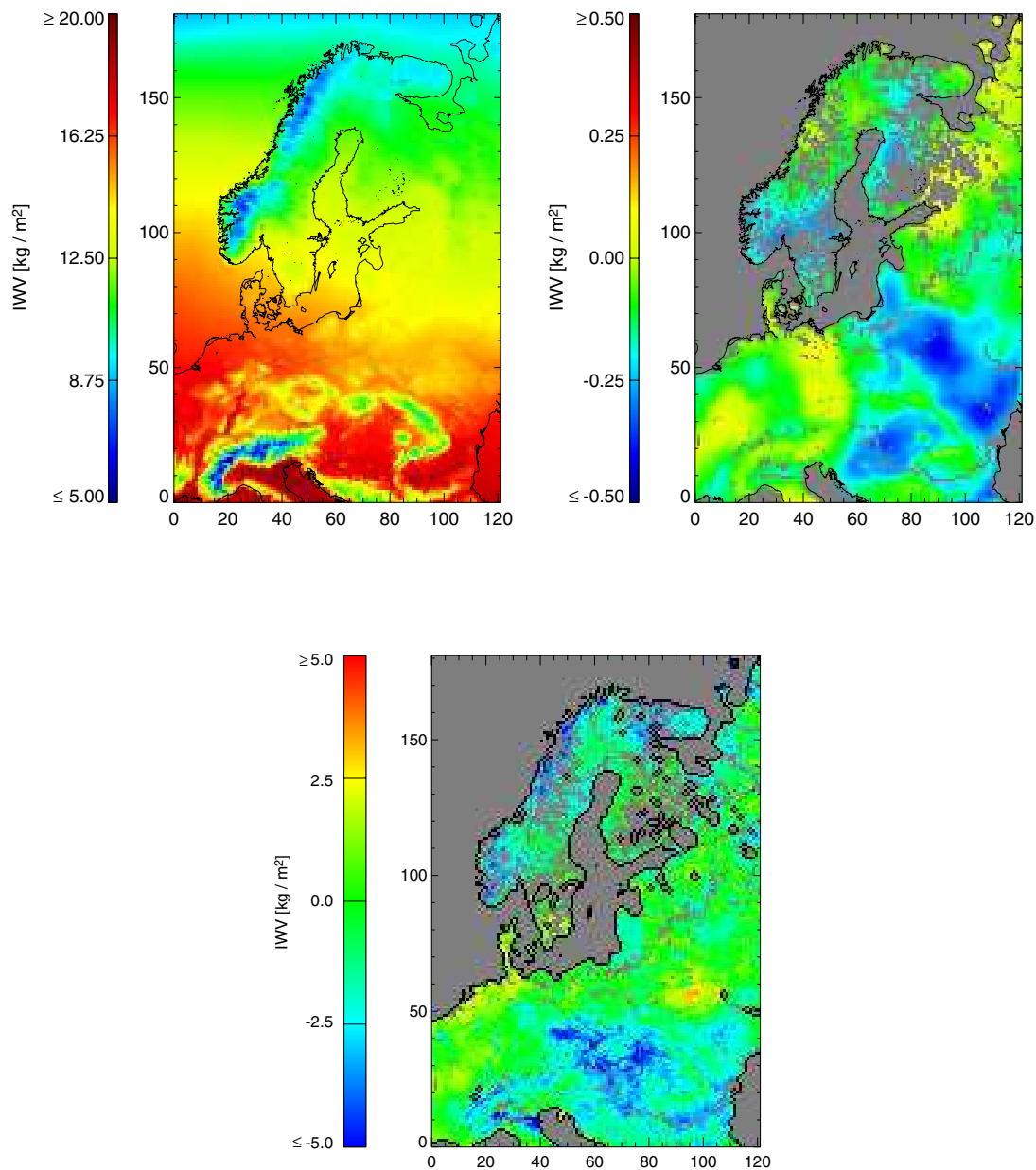


Figure 5.19: Upper panels: Left: Mean vertically integrated water vapor (IWV) for $REMO_{standard}$ in $[kg/m^2]$, right: Difference between IWV $REMO_{standard}$ and IWV $REMO_{cold}$ $[kg/m^2]$ ($REMO_{standard}$ minus $REMO_{cold}$). Lower panel: Difference between observed IWV (MODIS) and IWV simulated with $REMO_{standard}$ $[kg/m^2]$ ($REMO_{standard}$ minus MODIS) for the period from October 2001 to October 2003 (lower figure by courtesy of R. Leinweber, FU Berlin).

clear improvement of the model development. Generally, REMO tends to simulate in both model versions slightly higher values of IWV than observed.

The differences between the *REMO_{standard}* and the *REMO_{cold}* simulation are shown in more detail in figure 5.20 for the four sub areas. In addition to the mean annual cycle of integrated water vapor from 1999 to 2003 for *REMO_{standard}* (black line) and *REMO_{cold}* (red line), the differences between both simulations (*REMO_{cold}* minus *REMO_{standard}*) are shown (dashed lines). As it was the case for the average values over the two years shown in figure 5.19, the maximum differences in the mean annual cycle do not exceed $0.5 \frac{\text{kg}}{\text{m}^2}$. The tendency of having slightly higher values of IWV with *REMO_{cold}* shows for all sub areas, except for some summer months in *Germany* and in the *Baltic Sea* catchment, where *REMO_{cold}* has slightly lower values of IWV than *REMO_{standard}*.

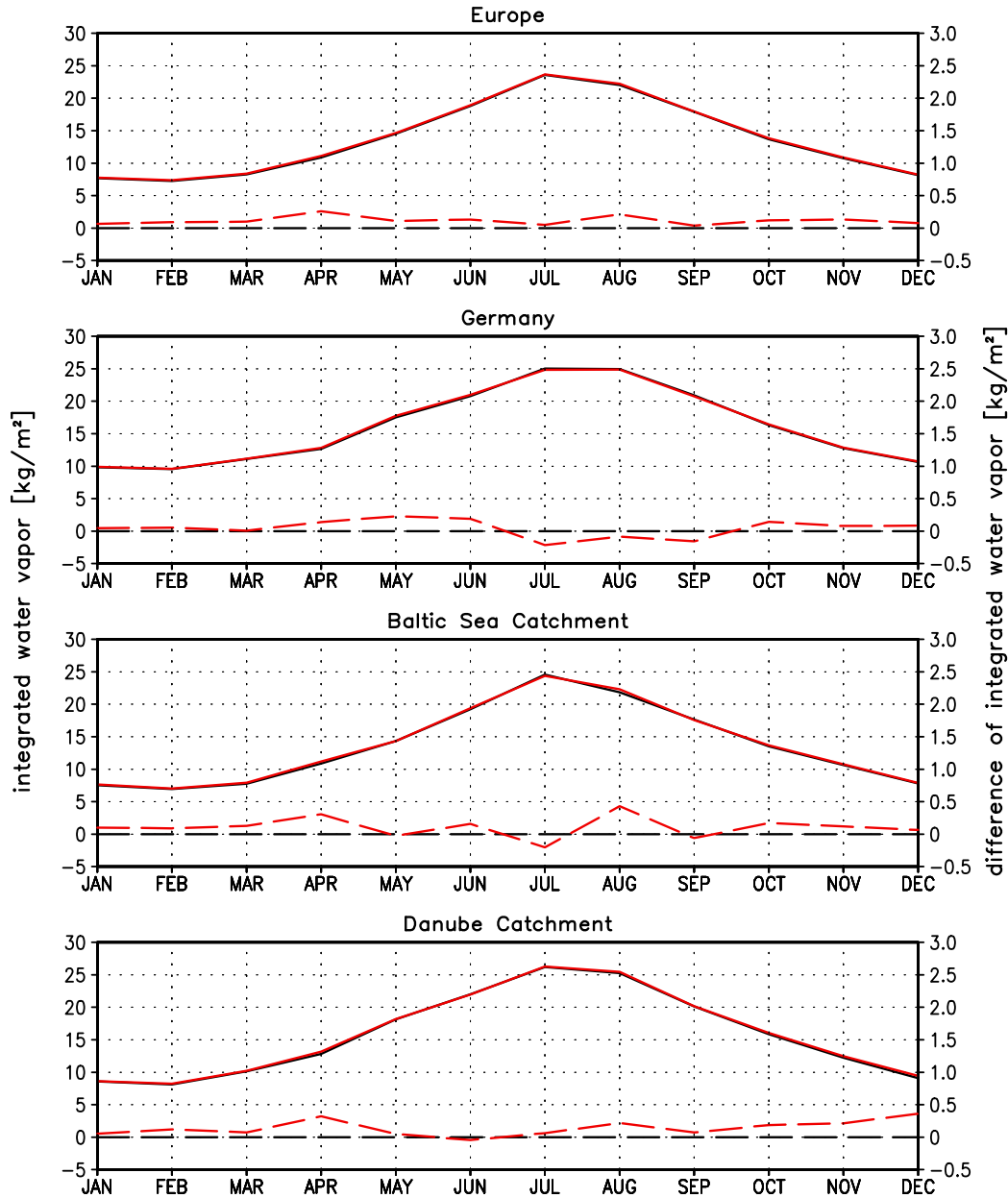


Figure 5.20: Mean annual cycle of integrated water vapor [$\frac{kg}{m^2}$] (1999 to 2003) for $REMO_{standard}$ (black line) and $REMO_{cold}$ (red line) both with $\frac{1}{6}^\circ$ horizontal resolution in different sub areas of the model simulation domain. Dashed: Difference between $REMO_{standard}$ and $REMO_{cold}$ with respect to $REMO_{standard}$

5.3.4 Total cloud fraction

Cloud fraction has been compared to observations derived from METEOSAT (METEOSAT-6 and 7) measurements. In the context of BALTIMOS, the observations have been interpolated to the REMO grid and are available for the period from 1993 to 2002 as monthly mean values. The algorithm used for deriving cloud coverage from satellite observations is based only on the thermal infrared window channel of the METEOSAT scanning imager (located in the atmospheric spectral window at around $11.5\mu m$). It is conceptual similar to the ISCCP algorithm, for which the error is estimated being less than 10 % (Rossow et al. 1993 [54]).

Figure 5.21 shows the mean annual cycle for the years 1999 to 2002 for the areas given in figure 5.7. Obviously, there is a systematic mismatch of observed and modeled cloud cover for the summer months. This underestimation of summertime cloud fraction by the model occurs in all areas and in both model versions. As summer atmospheres are to a large extent dominated by smaller-scale convective clouds, these clouds seem to be the reason for the discrepancy between simulated and observed cloud cover. Cloud cover in REMO is calculated in a rather simple way by deriving it from the relative humidity of the respective grid box, applying a minimum threshold value for grid-mean relative humidity. Convective clouds are only partially represented in the moisture field of the model for the following reason: The convection parameterization does not include cloud microphysics and it does neither include a memory of the convection state of the timestep before. Convection in a grid column is supposed to form, to develop, to precipitate and to dilute in one timestep. This is an appropriate assumption for large timesteps. With increasing horizontal resolution, time steps are becoming shorter. For the $\frac{1}{6}^\circ$ horizontal resolution simulation, the time step is 100 seconds which is much below the lifetime of a convective cloud. As discussed in section 2.2, it is questionable whether the assumptions underlying traditional convection parameterization approaches do hold for finer resolution and for short timesteps. Allowing the convective cloud to remain in the atmosphere for longer than only one timestep would probably result in a better representation of summer cloudiness.

Another source for the discrepancy between observed and simulated cloud cover could be the method to calculate a 2-dimensional total cloud cover (TCC) from the 3-dimensional cloud cover (CC) field. In REMO, this is done using the maximum

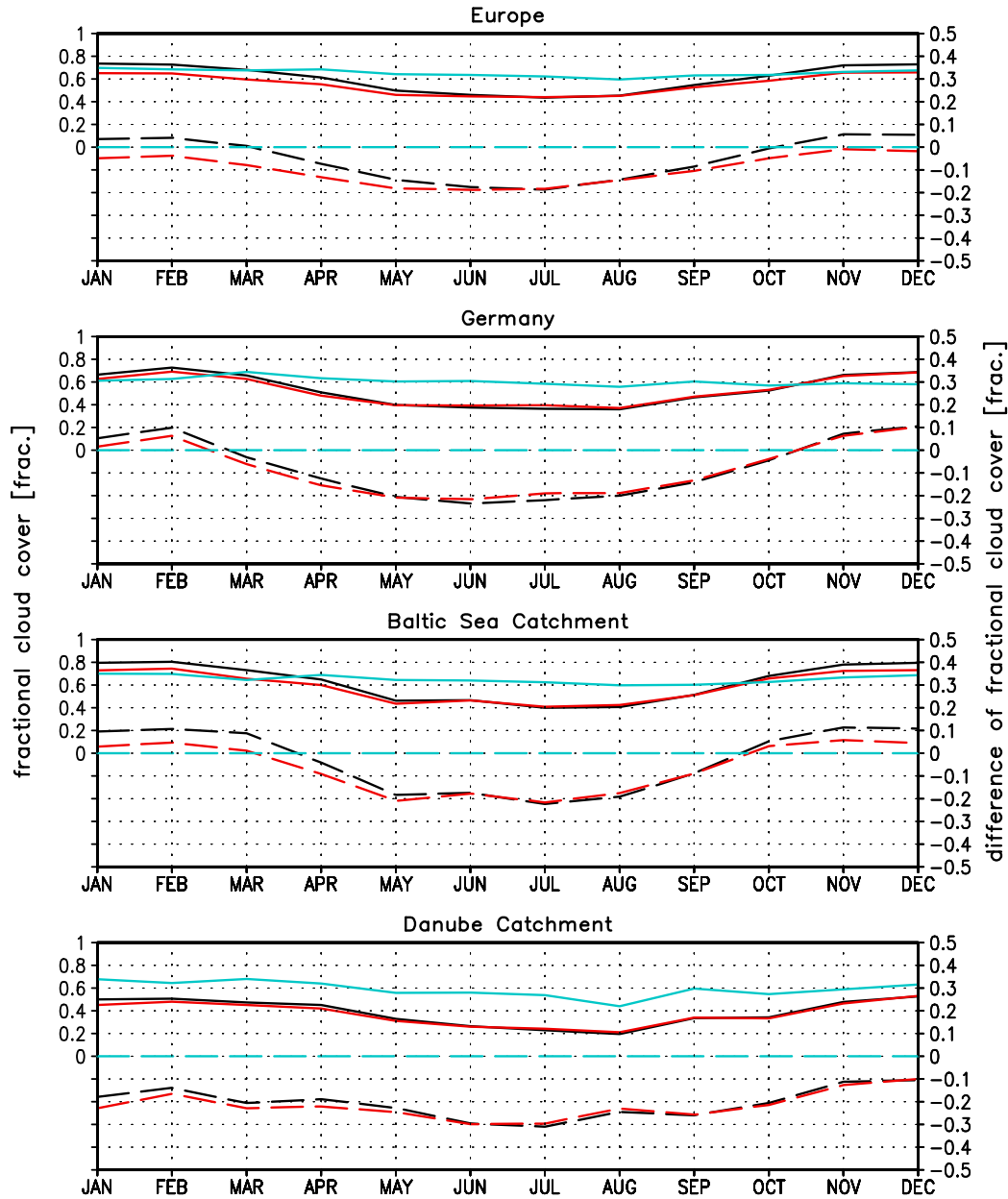


Figure 5.21: Solid lines: mean annual cycle of total cloud fraction (1999 to 2002) for observations derived from METEOSAT (blue line) compared to $REMO_{standard}$ (black line) and $REMO_{cold}$ (red line) both with $\frac{1}{6}^\circ$ horizontal resolution in different sub-areas of the model simulation domain. Dashed: difference between $REMO_{standard}$ and METEOSAT (black) and $REMO_{cold}$ and METEOSAT (red) with respect to METEOSAT.

random overlap assumption. With this approach, vertically continuous clouds are assumed to be maximally overlapped, while clouds at different heights that are separated by an entirely cloud-free model level are randomly overlapped. However, studies of Hogan and Illingworth (2000, [23]) indicate that for vertically continuous clouds, the mean overlap is distinctly more random than assumed by the maximum-random overlap, which would result in higher values of TCC for such clouds.

The differences between the simulation with *REMO_{standard}* and the simulation with *REMO_{cold}* are also visible in figure 5.21. For *Europe*, *REMO_{cold}* simulates up to 10% less cloud cover in winter and spring, and virtually unchanged values of cloud cover in summer and early autumn. This tendency is also the case for the sub-areas *Germany*, *Baltic Sea*, and *Danube*, whereas the differences in winter cloud cover are larger for the northern regions than for the southern catchment *Danube*. The decrease in winter cloud cover with *REMO_{cold}* compared to *REMO_{standard}* is consistent with the decreasing integrated total water and precipitation observed for the winter atmosphere (see sections 5.3.1 and 5.3.2).

In conclusion, both model versions disagree with observed total cloud cover especially in the summer months by simulating too little cloud amount. In winter, mismatches are generally smaller and seem still to be reduced with *REMO_{cold}*. The source of the error could either be already in the calculation of the 3-dimensional cloud cover field or it could be introduced by the maximum-random overlap method to calculate a 2-dimensional total cloud cover from the 3-dimensional field. If the latter would be the case, the observed mismatch would have no influences on other parts of the model physical processes, as the 2-dimensional TCC is only a diagnostic parameter. However, if the 3-dimensional cloud cover already strongly deviates from reality, the influences on other physical processes are larger, because the 3-dimensional TCC-field enters as input parameter both the calculation of radiative processes and the cloud and precipitation parameterization routine. As it was mentioned in section 5.3.1 for the atmospheric liquid water, a detailed validation of the vertical structure of the simulated cloud amount would be highly desirable.

5.3.5 Mean sea level pressure

The mean sea level pressure (MSLP) is a helpful indicator to judge if both model versions reproduce similar climates. Figure 5.23, 5.24, 5.25, and 5.26 show the mean sea level pressure averaged over the 5 years (1999 to 2003) for all seasons each with the $REMO_{standard}$ simulation on the left and the difference between the $REMO_{standard}$ and the $REMO_{cold}$ simulation ($REMO_{cold}$ minus $REMO_{standard}$) on the right for the $\frac{1}{6}^\circ$ simulations. The differences between the model versions are relatively small for all seasons, i.e. they do not exceed $1hPa$. For autumn and winter, the seasonal mean differences are entirely positive throughout the whole simulation domain, i.e. with $REMO_{cold}$ the seasonal mean MSLP slightly increases for those seasons. For spring and summer, there are parts of the simulation domain, where the MSLP simulated with $REMO_{cold}$ is slightly reduced, in summer mainly over land. The differences for the single months are shown as time series for the *Baltic Sea* sub area in figure 5.22 ($REMO_{cold}$ minus $REMO_{standard}$). For single months again the differences are relatively small, having maximum values of $1.7hPa$. Altogether, the differences are in an order of magnitude that can be related to internal variability in the simulations as well as to changes in parameterizations. However this does not exclude the possibility that changes in the cloud parameterization are responsible for the minor changes in simulated mean sea level pressure, it just makes it impossible to disregard internal variability as source for the differences.

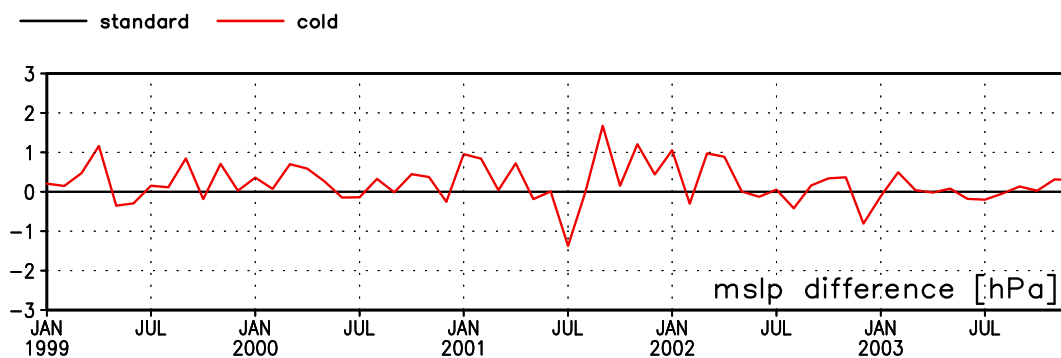


Figure 5.22: Change of the monthly mean values of mean sea level pressure for $REMO_{cold}$ (red line) with respect to the simulation with $REMO_{standard}$ (black line). Area of investigation is the Baltic Sea catchment.

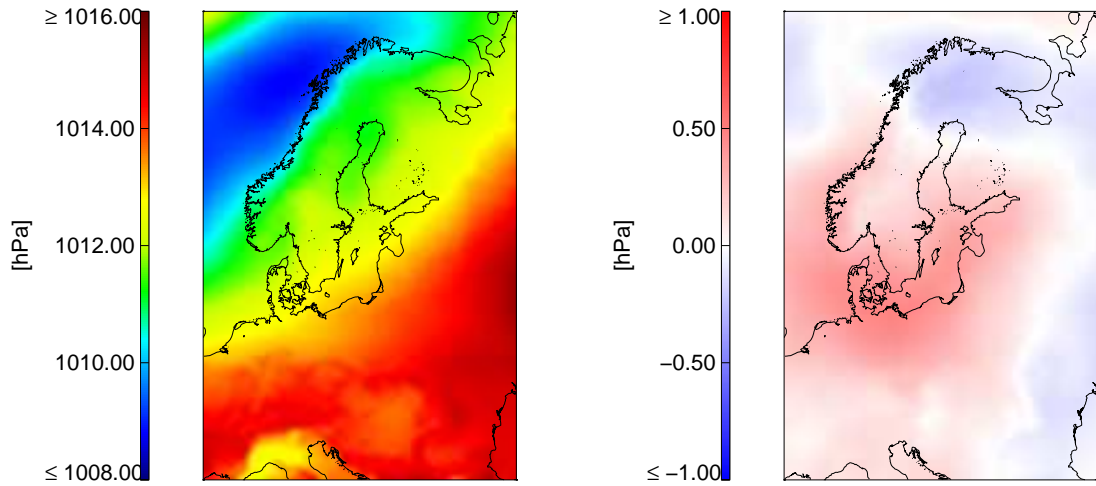


Figure 5.23: Mean sea level pressure in spring (March/April/May; 1999 to 2003) simulated with *REMO_standard* (left). Differences for MSLP spring: *REMO_cold* minus *REMO_standard* (right).

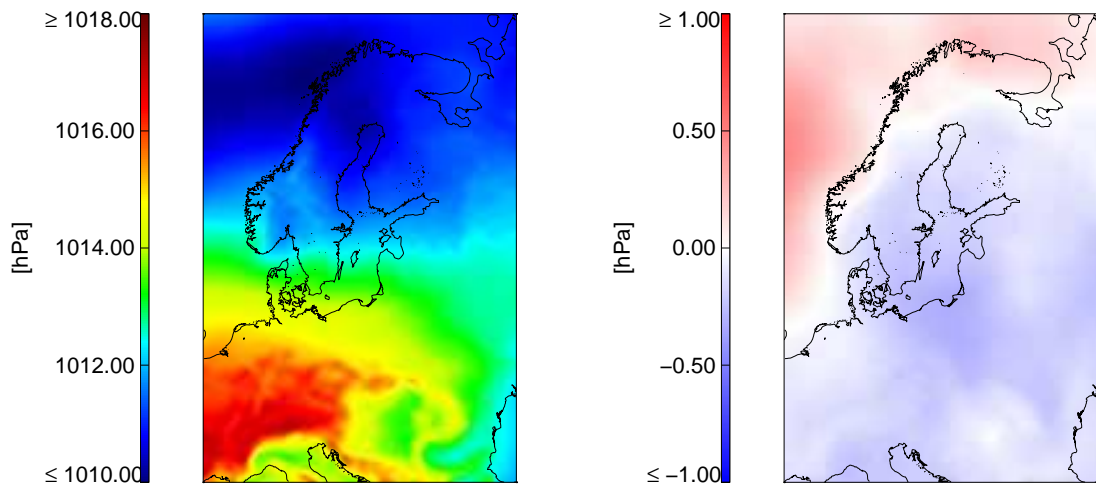


Figure 5.24: Mean sea level pressure in summer (June/July/August; 1999 to 2003) simulated with *REMO_standard* (left). Differences for MSLP summer: *REMO_cold* minus *REMO_standard* (right).

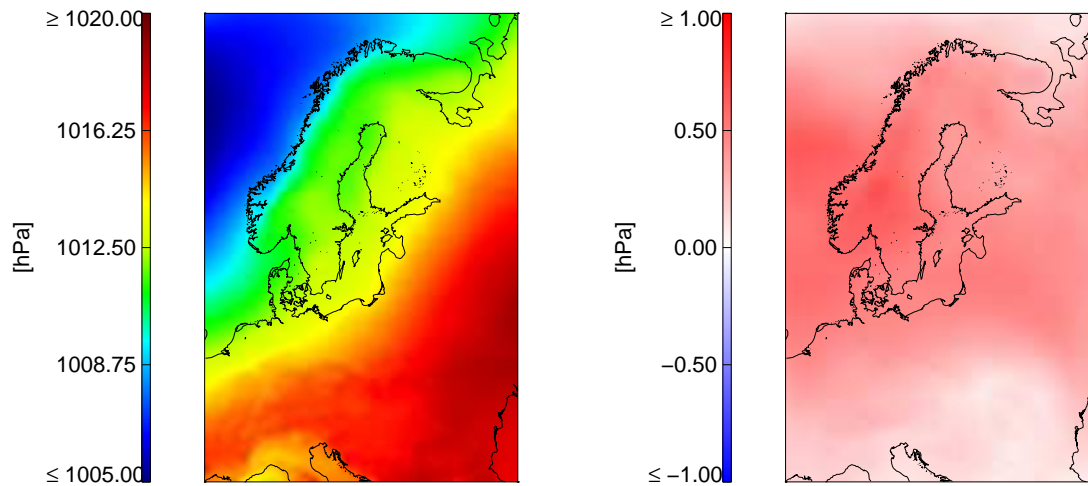


Figure 5.25: Mean sea level pressure in autumn (September/October/November; 1999 to 2003) simulated with *REMO_standard* (left). Differences for MSLP autumn: *REMO_cold* minus *REMO_standard* (right).

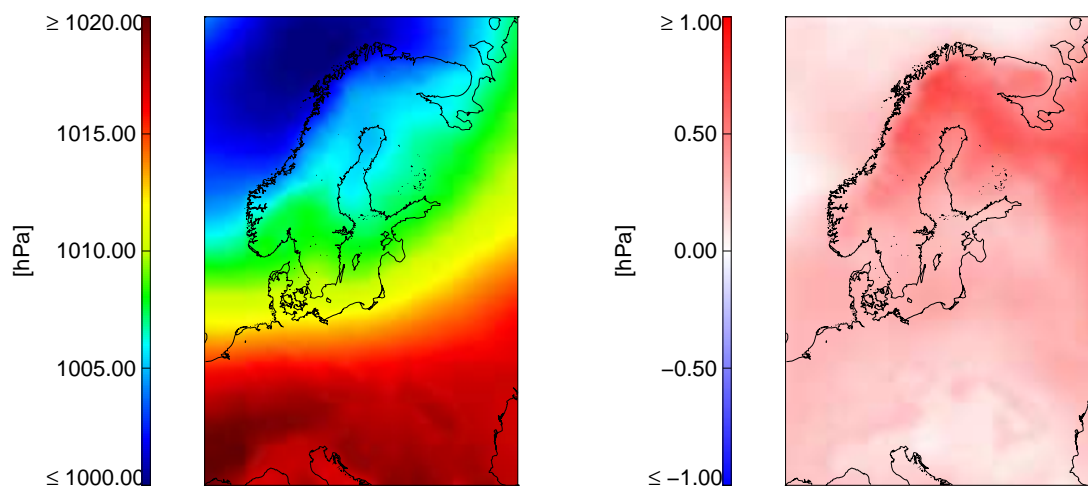


Figure 5.26: Mean sea level pressure in winter (December/January/February; 1999 to 2003) simulated with *REMO_standard* (left). Differences for MSLP winter: *REMO_cold* minus *REMO_standard* (right).

5.3.6 Temperature

Simulated surface and atmospheric temperatures have been compared for the simulations with *REMO_{standard}* and *REMO_{cold}*. In addition, 2-meter temperature has been compared to observed 2-meter temperatures. The results of this comparison are shown at the end of this section.

Time series of area-averaged surface temperatures for the sub-areas are shown in figure 5.27 for the model simulations with *REMO_{standard}* and *REMO_{cold}* in $\frac{1}{6}^\circ$ horizontal resolution. In addition to the mean annual cycle of temperature, the differences between the simulations are highlighted as dashed lines.

On average over the five years from 1999 to 2003, the changes between *REMO_{standard}* and *REMO_{cold}* result in largest changes in surface temperature for the winter and spring months. For the northern regions of the simulation domain, winter temperatures decrease by up to 1°C (*Baltic Sea* in figure 5.27). For the *Danube* sub-area, an increase in surface temperature of up to 0.5°C in winter and early summer can be observed. Summer and early autumn temperatures are virtually unchanged for all areas. Overall, shown in the uppermost panel of figure 5.27, the changes result in a decrease in temperature in November, December, January and February, a slight increase in spring and unchanged mean temperatures in the other seasons. The decrease of surface temperature with *REMO_{cold}* in the winter months probably is a result of the decreasing winter cloud cover with *REMO_{cold}* (see section 5.3.4), as clouds in winter mostly have a warming effect by reflecting outgoing thermal radiation back to the earth's surface.

There is no remarkable difference in the vertical distribution of temperature in the atmosphere between the two model versions. Figure 5.28 shows the mean vertical summer and winter temperatures as a *quasi-zonal mean* (introduced in section 5.3.1), the left panel comprises results from *REMO_{standard}*, the right panel those simulated with *REMO_{cold}*. All seasons have been examined. As no significant changes are visible in any season, only summer and winter are displayed exemplarily.

As temperature observations have not been available for the entire 4-years period from 1999 to 2003, but only for the years 1999 and 2000, temperature validation is restricted to these two years. The temperature observations provided by the Climate Research Unit (CRU) are globally gridded 2-meter temperatures on a $0.5^\circ \times 0.5^\circ$ grid over land. The climatology that was primarily covering the period from 1961

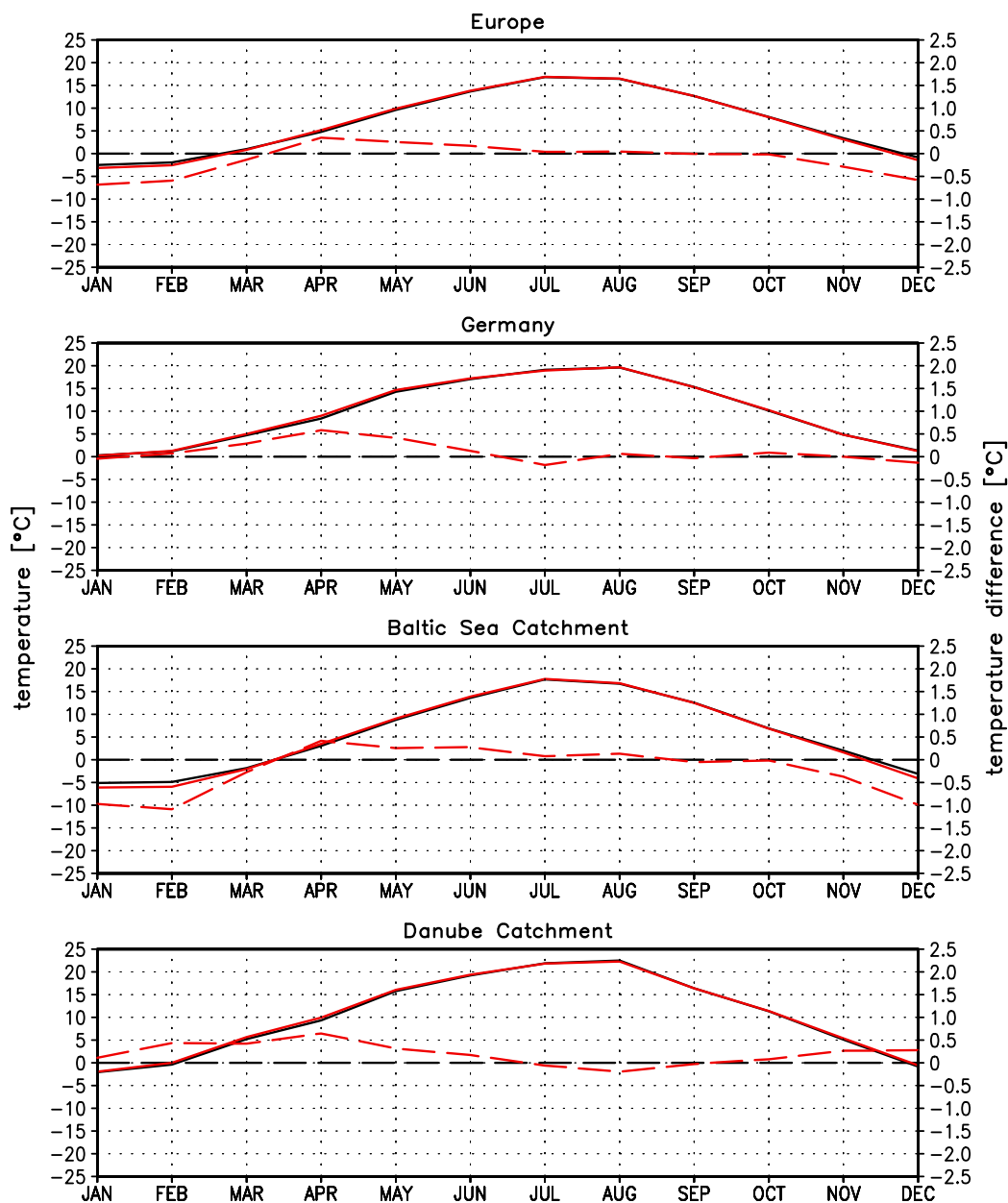


Figure 5.27: Mean annual cycle of surface temperature [°C] (1999 to 2003) for *REMO_standard* (black line) and *REMO_cold* (red line) both with $\frac{1}{6}^\circ$ horizontal resolution in different sub-areas of the model simulation domain. Dashed: Difference between *REMO_standard* and *REMO_cold* with respect to *REMO_standard*

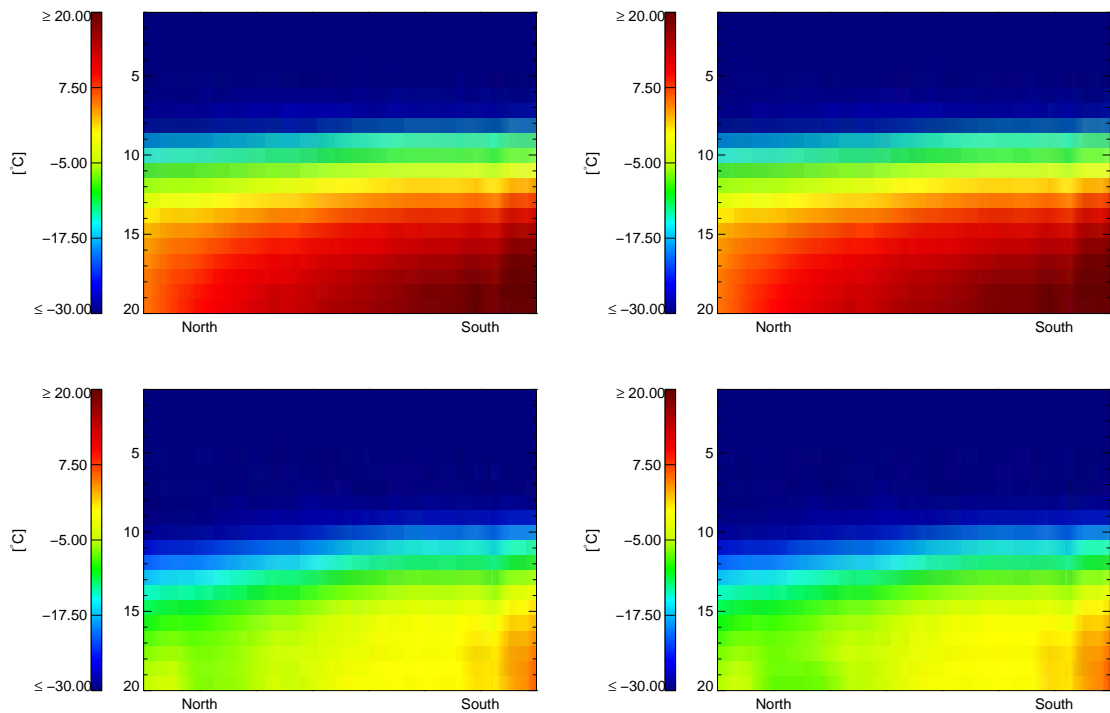


Figure 5.28: *Quasi-zonal mean* temperature $REMO_{standard}$ (left) and $REMO_{cold}$ (right) in $^{\circ}C$ for the 20 model levels. Summer mean (upper panels) and winter mean (lower panels) for 1999 to 2003.

to 1990 has recently been extended up to the year 2000. For the comparison, model results as well as observations have been averaged for the three sub-areas introduced in section 5.3, considering only land areas.

The comparison is illustrated in figure 5.29. As for the mean annual cycle of surface temperature in figure 5.27, the differences between the simulated 2-meter temperature and the observed 2-meter temperature ($REMO$ minus CRU) is given for both model versions by the dashed lines (red for $REMO_{cold}$ minus CRU , black for $REMO_{standard}$ minus CRU). For the two years, the largest differences between simulated and observed 2-meter temperature can be seen in late summer, where both model versions tend to overestimate 2-meter temperature by up to $2^{\circ}C$ for *Germany* and the *Baltic Sea* area, and by up to $4^{\circ}C$ for the southern sub-area *Danube*. For *Germany* and the *Baltic Sea* area, winter and spring 2-meter temperatures are slightly underestimated by both model versions. The differences of the 2-meter temperature between the model versions are distinctly smaller than the deviations

from the observed temperatures and basically show the same characteristics as the differences between the surface temperatures that were shown in figure 5.27.

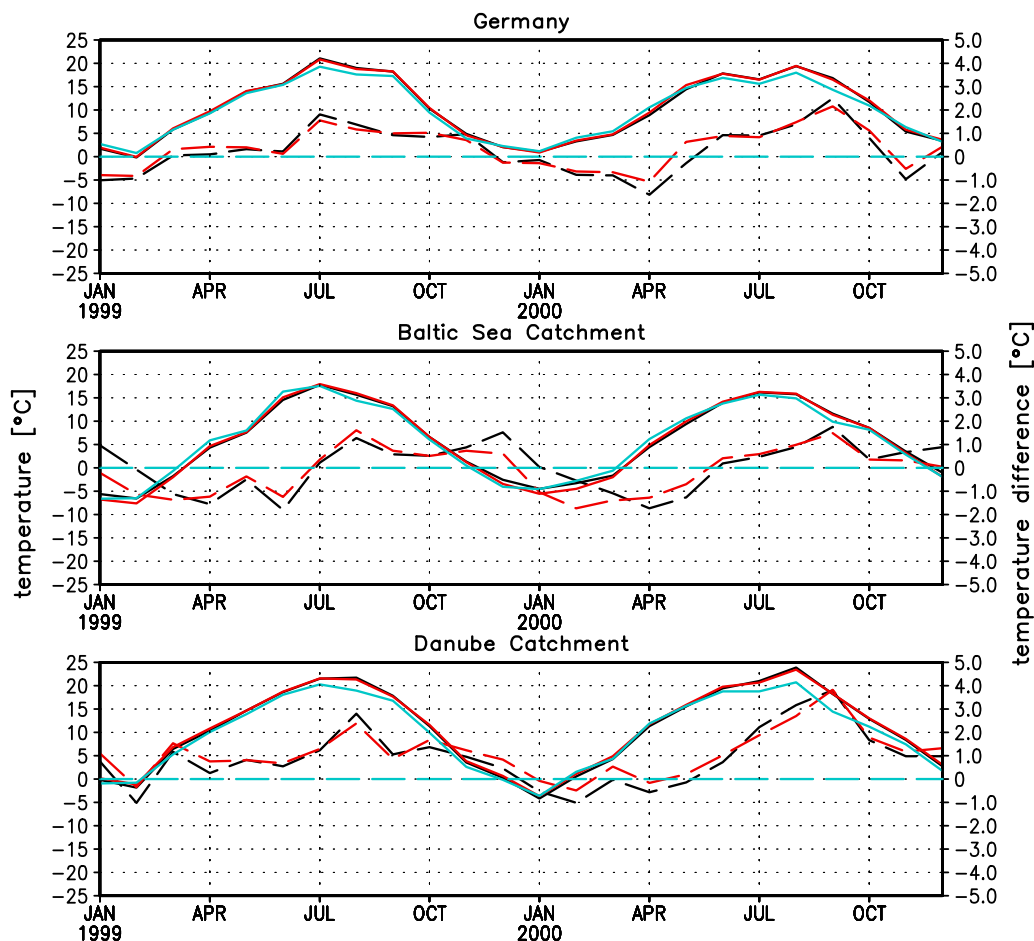


Figure 5.29: Monthly mean 2-meter temperature [$^{\circ}C$] from January 1999 to December 2000 for CRU Observations (blue line) compared to $REMO_{standard}$ (black line) and $REMO_{cold}$ (red line) both with $\frac{1}{6}^{\circ}$ horizontal resolution in different sub-areas of the model simulation domain. Dashed: Difference between $REMO_{standard}$ and CRU (black) and $REMO_{cold}$ and CRU (red) both with respect to CRU observations

The differences between simulated and observed temperatures could partially be attributed to uncertainties of the observed dataset, which are mostly due to the density of available observing stations. New et al. provide estimates of this uncertainty by performing internal cross validation as well as by comparing their data with other available observed climatologies. For the period of 1961 to 1990, they give uncertainties in seasonal mean temperature of between 0.5 and 1.3 K (New et al., 1999 [44]). However, in their dataset, Europe represents one of the *well-sampled* regions, so that for this comparison, the observation errors should be at the low end of the given range. Another source of uncertainty in the comparison of temperature observations to simulated temperature is the (possibly) different height of the observation station compared to the mean height of the model grid-box. In the case of the CRU dataset, elevation effects are accounted for by including elevation as predictor variable in the interpolation routine from the station location to the 0.5° grid (New et al., 1999 [44]). For the analyzed areas, the differences in mean elevation of the grid-boxes and in the spatial standard deviation of grid-box elevations between the $\frac{1}{2}^\circ$ and the $\frac{1}{6}^\circ$ model simulation domain are relatively small (see also figure 5.7). Thus the differences between the observations on a 0.5° grid and the model simulations on the $\frac{1}{6}^\circ$ grid resulting from elevation effects should be small. In conclusion, the vertical structure of atmospheric temperature and the annual cycle of surface temperature and 2-meter temperature do not show large differences between $REMO_{standard}$ and $REMO_{cold}$. Winter temperatures are by up to 0.5° lower with $REMO_{cold}$ than with $REMO_{standard}$, especially in the northern catchments. Temperatures in spring tend to be slightly higher in the $REMO_{cold}$ simulation for all catchments. Inter-model differences are distinctly smaller than the differences between model simulation and CRU observations. The observed 2-meter summer temperatures are by up to $2-4^\circ C$ lower than simulated, a finding which is more pronounced for the southern catchment *Danube* than for the northern *Baltic Sea* catchment.

5.4 Sensitivity studies

5.4.1 Influence of driving fields and resolution

As discussed in section 5.3, the comparison between the $\frac{1}{6}^\circ$ resolution simulations belonging to the consistent chain of simulations using the same model version for both the $\frac{1}{2}^\circ$ and the $\frac{1}{6}^\circ$ resolution simulations, does not allow to separate the influence of the driving fields on simulation results from the influence of the changes in the physical parameterizations. By comparing the differences between the $\frac{1}{2}^\circ$ simulations with $REMO_{standard}$ and $REMO_{cold}$ and the differences between the $\frac{1}{6}^\circ$ simulations with $REMO_{standard}$ and $REMO_{cold_driven_by_standard}$, the consistency of the input data for each resolution is guaranteed.

In all following figures, the differences between $REMO_{cold}$ and $REMO_{standard}$ in $\frac{1}{2}^\circ$ horizontal resolution both driven by ECMWF analyses (*Baltic 1* $\frac{1}{2}^\circ$ and *Baltic 2* $\frac{1}{2}^\circ$) are shown by a solid red line. The differences between $REMO_{standard}$ and $REMO_{cold_driven_by_standard}$ in $\frac{1}{6}^\circ$ resolution, both driven by the $REMO_{standard}$ $\frac{1}{2}^\circ$ simulation (*Baltic 1* $\frac{1}{6}^\circ$ and *Baltic 3* $\frac{1}{6}^\circ$) are shown by a dashed red line. The green line shows the differences between two simulations with $REMO_{cold}$ in $\frac{1}{6}^\circ$, which differ only by their driving fields (*Baltic 1* $\frac{1}{6}^\circ$ and *Baltic 2* $\frac{1}{6}^\circ$). As the differences between $REMO_{standard}$ and $REMO_{cold_driven_by_standard}$ are similar to the differences between $REMO_{standard}$ and $REMO_{cold}$, the detailed validation presented in the last sections is not repeated for the simulation with $REMO_{cold_driven_by_standard}$. The analysis here will be restricted to the differences between the $\frac{1}{2}^\circ$ simulations and the $\frac{1}{6}^\circ$ simulations as well as the order of magnitude of differences induced by using different driving fields for *Baltic 2* $\frac{1}{6}^\circ$ and *Baltic 3* $\frac{1}{6}^\circ$.

Figure 5.30 shows the differences in the mean annual cycle of precipitation for the four catchments. For the $\frac{1}{6}^\circ$ simulations, the differences in simulated precipitation originating from different driving fields (green line) are in most cases larger than the differences originating from the different model versions (solid red line). Thus the sensitivity of the model to the driving data is larger than the sensitivity of the model to the changes in the cloud parameterization. For the simulations which differ by model version but not by driving fields (red lines), the differences of summer precipitation in the sub areas between the $\frac{1}{2}^\circ$ simulations are distinctly larger than the differences between the $\frac{1}{6}^\circ$ simulations. For the other seasons, the differences

between $REMO_{standard}$ and $REMO_{cold_driven_by_standard}$ are approximately of the same order of magnitude. For the interpretation of the apparently strong resolution dependency of the summer precipitation differences between $REMO_{standard}$ and $REMO_{cold_driven_by_standard}$, different aspects must be taken into account:

Firstly, it is possible that the parameterizations included in the model are not independent from model grid resolution. This is the case e.g. for the autoconversion rate, where the dependency on grid resolution has been discussed in section 4.1, and possibly also for the other process rates presented in the same chapter. The parameterization of large-scale clouds included in $REMO_{cold}$ is more *single-process-based*, i.e. it is aiming to describe as many small scale processes separately, whereas the parameterization included in $REMO_{standard}$ is more an *integral* approach, combining the effects of several physical processes into one integral equation. The *single-process-based* approach may fail for the coarser resolution, causing the stated overestimation for the summer precipitation. The fact that the differences are most pronounced in summer precipitation might also be an indicator for stronger grid-scale resolution dependency of the convection scheme in REMO.

A second aspect to be considered as a reason for the apparently different behavior of the model on different scales is again the driving field. Although the $\frac{1}{2}^\circ$ simulations are driven by the same fields (ECMWF analyses) and also the $\frac{1}{6}^\circ$ simulations are driven by the same fields (the $REMO_{standard}$ $\frac{1}{2}^\circ$ simulation), the differences between the $\frac{1}{2}^\circ$ simulations can hardly be compared to the differences between the $\frac{1}{6}^\circ$ simulations for the following reason: A given climate model develops - dependent on the inherent parameterizations - an equilibrium for its atmosphere, i.e. in terms of water holding capability. This equilibrium can be different for different models, but should be similar for one model in different grid resolutions. Assuming that the equilibrium of the ECMWF-climate differs from the REMO-climate equilibrium, the model if driven by ECMWF analyses is forced to adjust its atmosphere to its equilibrium at every time step, while the driving fields permanently impose their equilibrium. This effect is already known for REMO, which tends to remove much more humidity from the atmosphere by precipitation when it is driven by analyses than when it is driven by another REMO simulation in coarser resolution. This adjustment of the driving fields to the REMO-climate equilibrium could be coped with differently by $REMO_{standard}$ and $REMO_{cold}$, resulting in larger differences

between *REMO_{standard}* and *REMO_{cold}* for the simulations driven by ECMWF analyses than for the simulation driven by REMO itself.

For the other parameters (surface temperature, cloud cover, integrated water vapor and vertically integrated total water content shown in figures 5.31 and 5.32), the differences between the $\frac{1}{6}^\circ$ simulations are larger in the winter season for all variables than the differences between the $\frac{1}{2}^\circ$ simulations. For integrated liquid water content, this is also valid for summer. For temperature and cloud cover, the summer differences between the $\frac{1}{2}^\circ$ simulations and the $\frac{1}{6}^\circ$ simulations are close to each other, which is also caused by the fact that the differences themselves are much smaller for summer than for winter. For surface temperature, cloud cover and vertically integrated liquid water, the differences between the *REMO_{cold}* driven by *REMO_{cold}* and *REMO_{cold-driven-by-standard}* are small. Thus changes in those parameters, derived in section 5.3 can definitely be related to the differences between the model versions. These parameters seem to be less sensitive to differences in the driving fields. Tying up to the hypothesis derived for the precipitation concerning the adjustment of the model's atmosphere to some kind of equilibrium, this process is obviously controlled by the amount of precipitation, which reacts sensitively to changes in the input fields. It is controlled only to a lower degree by the other atmospheric parameters, which are not that sensitive to changes in the driving fields. In conclusion, the resolution dependency of the changes introduced in the cloud parameterization does not show systematic differences between the simulation results for the $\frac{1}{2}^\circ$ and the $\frac{1}{6}^\circ$ simulations, but shows differences in the strength of the changes, which are mostly larger for the $\frac{1}{6}^\circ$ simulations than for the $\frac{1}{2}^\circ$ simulations. An exception is the simulated summer precipitation, where a resolution dependency of the convection scheme possibly adds to the differences.

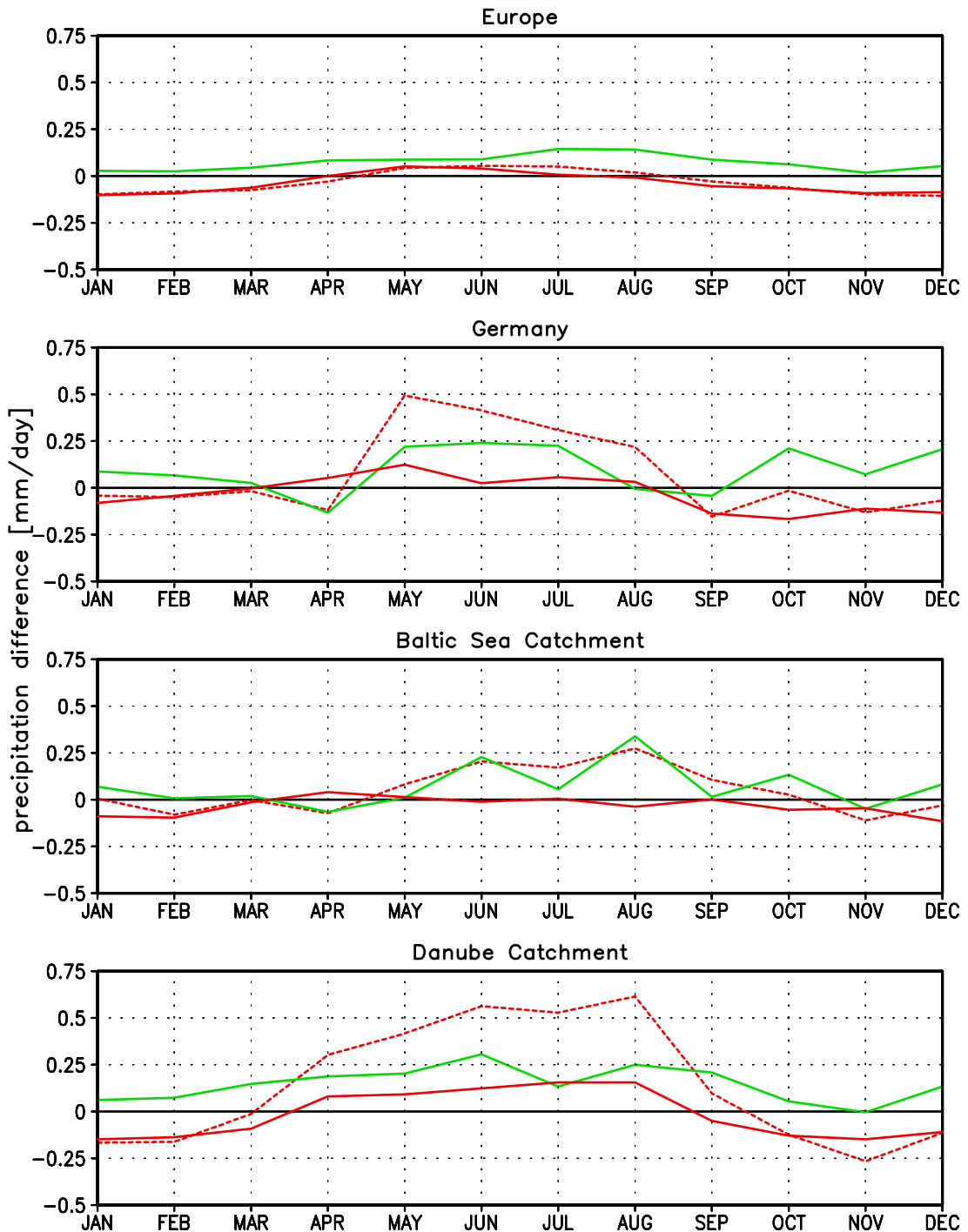


Figure 5.30: Differences in the mean annual cycle of total precipitation [$\frac{mm}{day}$]. $REMO_{cold}$ minus $REMO_{standard}$ in $\frac{1}{2}^\circ$ resolution both driven by ECMWF analyses (dashed red line), $REMO_{cold}$ minus $REMO_{standard}$ in $\frac{1}{6}^\circ$ resolution both driven by $REMO_{standard}$ $\frac{1}{2}^\circ$ (solid red line), and $REMO_{cold}$ $\frac{1}{6}^\circ$ driven by $REMO_{cold}$ $\frac{1}{2}^\circ$ minus $REMO_{cold}$ $\frac{1}{6}^\circ$ driven by $REMO_{standard}$ $\frac{1}{2}^\circ$ (solid green line).

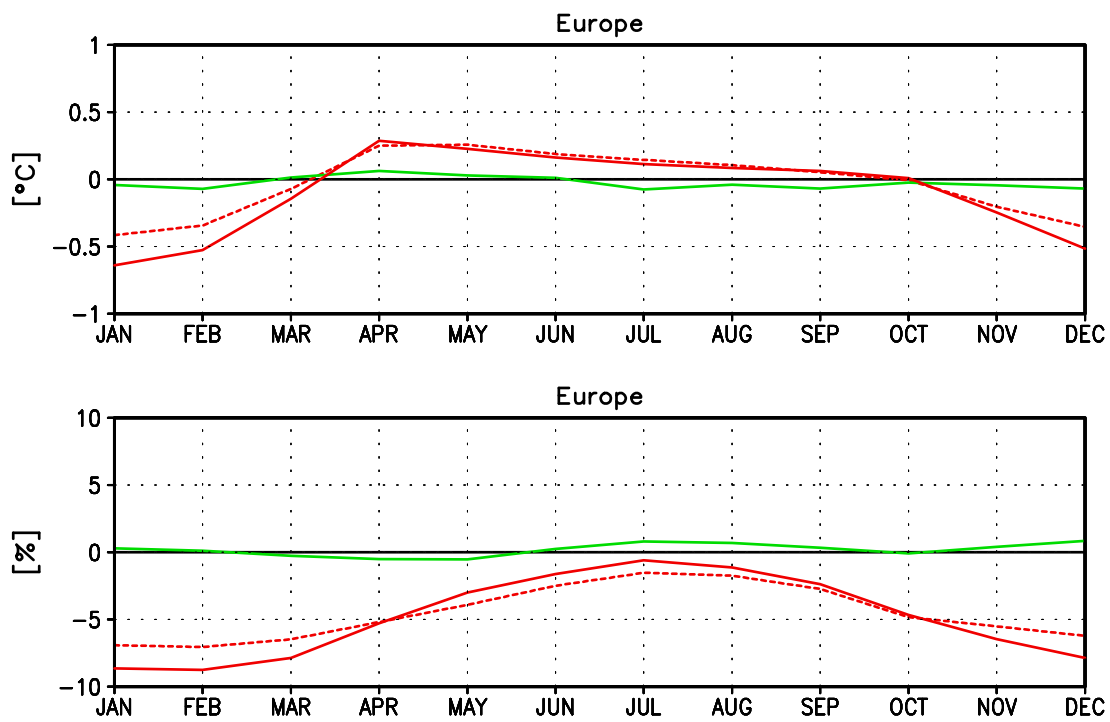


Figure 5.31: Differences in the mean annual cycle of surface temperature (upper panel) and total cloud cover (lower panel). $REMO_{cold}$ minus $REMO_{standard}$ in $\frac{1}{2}^\circ$ resolution both driven by ECMWF analyses (dashed red line), $REMO_{cold}$ minus $REMO_{standard}$ in $\frac{1}{6}^\circ$ resolution both driven by $REMO_{standard}$ $\frac{1}{2}^\circ$ (solid red line), and $REMO_{cold}$ $\frac{1}{6}^\circ$ driven by $REMO_{cold}$ $\frac{1}{2}^\circ$ minus $REMO_{cold}$ $\frac{1}{6}^\circ$ driven by $REMO_{standard}$ $\frac{1}{2}^\circ$ (solid green line).

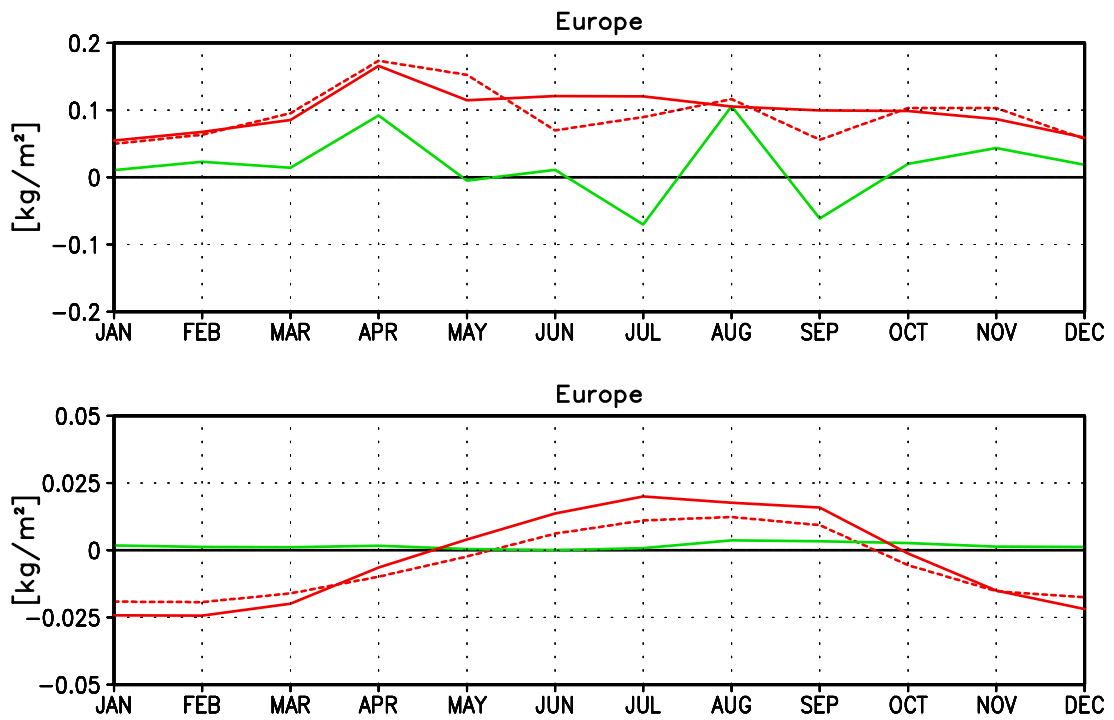


Figure 5.32: Differences in the mean annual cycle of integrated water vapor (upper panel) and total vertically integrated water content (lower panel). $REMO_{cold}$ minus $REMO_{standard}$ in $\frac{1}{2}^\circ$ resolution both driven by ECMWF analyses (dashed red line), $REMO_{cold}$ minus $REMO_{standard}$ in $\frac{1}{6}^\circ$ resolution both driven by $REMO_{standard}$ $\frac{1}{2}^\circ$ (solid red line), and $REMO_{cold}$ $\frac{1}{6}^\circ$ driven by $REMO_{cold}$ $\frac{1}{2}^\circ$ minus $REMO_{cold}$ $\frac{1}{6}^\circ$ driven by $REMO_{standard}$ $\frac{1}{2}^\circ$ (solid green line).

5.4.2 Sensitivity to changes of the microphysical parameters

Resulting from the examinations presented in the last sections, one problem in the cloud parameterization in REMO seems to be the amount of precipitation which is overestimated for all presented model simulations. For *REMO_{cold}*, this is especially true for summer precipitation, where the deviations from observed values are largest. Deficiencies in the simulated precipitation have an impact on other model variables and can of course be founded in deficiencies of other model variables. This chain encompasses all variables of the hydrological cycle and can e.g. be seen in the underestimation of summer cloudiness stated in section 5.3.4 and in the overestimation of the integrated water vapor (see section 5.3.3). The reasons for this can be manifold, ranging from external influences as e.g. the too large amount of humidity transported into the model domain by the influence of the driving fields over shortcomings in the vertical and horizontal transports of humidity and energy by the model dynamics to leakages in the model's cloud physical schemes. Sensitivity studies here are limited to the field of cloud microphysics, however bearing in mind that the problems could as well be caused elsewhere. As mentioned in section 4.1, the implementation of the new cloud microphysics in the global climate model ECHAM5 led to the inclusion of several tuning parameters, one of them determining the efficiency of precipitation formation in warm clouds.

Another parameter which has been found to be crucial in the regulation of the amount of precipitation formed in the large-scale microphysical scheme is the critical relative humidity, introduced in section 3.2.1, which is used in both model versions. The sensitivity of the simulations to the choice of this parameter will be discussed. Both sensitivity studies have been performed for the domain shown in figure 5.7 with a horizontal resolution of $\frac{1}{2}^\circ$ for the five year period between 1999 and 2003. The characteristics of the simulations are summarized in table 5.1. The sensitivity studies will be presented in the following two sections.

Autoconversion rate for warm clouds in the large-scale cloud scheme

As mentioned in section 4.1, autoconversion rates as used in the large-scale cloud parameterization scheme strongly depend on model resolution, implying sometimes the need to arbitrarily apply tuning factors as it is the case for the ECHAM5 global

model. An example for such a tuning factor is the factor γ_1 applied in the equation for autoconversion (equation 4.3). To assess the influence of the large-scale warm-cloud autoconversion rate on simulated precipitation, the five-year period has been simulated with $\gamma_1 = 7.5$ in addition to the standard simulations with $\gamma_1 = 15$. In the following, this simulation will be addressed as *REMO_{aut}* (see table 5.1). The theoretical basis of this change is shown in figure 4.3 in section 4.1, where the autoconversion rate with $\gamma_1 = 7.5$ is drawn as blue line and the autoconversion rate with $\gamma_1 = 15$ in red. To halve γ_1 results in lower rates for the autoconversion from liquid water to rain. The differences between the simulation with *REMO_{aut}* and the reference simulation with *REMO_{cold}* are shown by the red lines in figure 5.33 for precipitation, surface temperature and total cloud cover. All time series are area-averaged values of grid boxes located in the Baltic Sea catchment area. The smaller sub-area *Baltic Sea* has been chosen for model evaluation, to prevent possible changes from being overseen by averaging over large domains. Nevertheless, the investigated area remains large enough for the changes to be significant.

At first view astonishingly, the reduction of the autoconversion rate in the large-scale cloud scheme results in no clear trend in the simulated total precipitation amount. In the five-year period, the largest differences occur with $+0.5 \frac{mm}{day}$ for July 2000 and $-0.5 \frac{mm}{day}$ for July 2001. This result is also valid for the precipitation components. Figure 5.34 shows the difference in the single precipitation components between *REMO_{aut}* and *REMO_{cold}* again as red line. The change in the large-scale scheme introduces a change in the large-scale component of precipitation and also in the precipitation amount produced in the sub-grid scale cloud scheme, again showing no clear trend. The surface temperature and total cloud cover differences shown in figure 5.33 (red lines) result in changes of surface temperature of maximum $0.4 \text{ }^\circ\text{C}$, and differences of the simulated cloud cover between *REMO_{aut}* and *REMO_{cold}* of less than 5%, again showing no significant trend for *REMO_{aut}*. The changes in simulated mean sea level pressure (MSLP) are shown in figure 5.35, where the red line illustrates the differences between *REMO_{aut}* and *REMO_{cold}*. The changes in MSLP are relatively small and again do not show a clear trend. They are of the same order of magnitude as the MSLP differences between the simulations with *REMO_{standard}* and *REMO_{cold}* shown in section 5.3.5 (see figure 5.22) and can therefore possibly be attributed to the internal variability of the model.

This sensitivity study illustrates the problem that an effective control of the amount of simulated precipitation by the tuning of single precipitation processes is not possible, as the rain formation - as in this case - can be overtaken by other processes/formulations. In this case, the expected result - to get less precipitation from warm clouds - is not achieved, e.g. due to the convection scheme, which in some situations not only balances the lower autoconversion rates, but even seems to be more efficient in removing moisture from the atmosphere than the autoconversion process in the large-scale scheme.

Improving the simulated precipitation of the model by modifying the tuning parameters confined to single cloud microphysical processes, as in this case the autoconversion rate for warm clouds, seems not to be an appropriate solution to the problem.

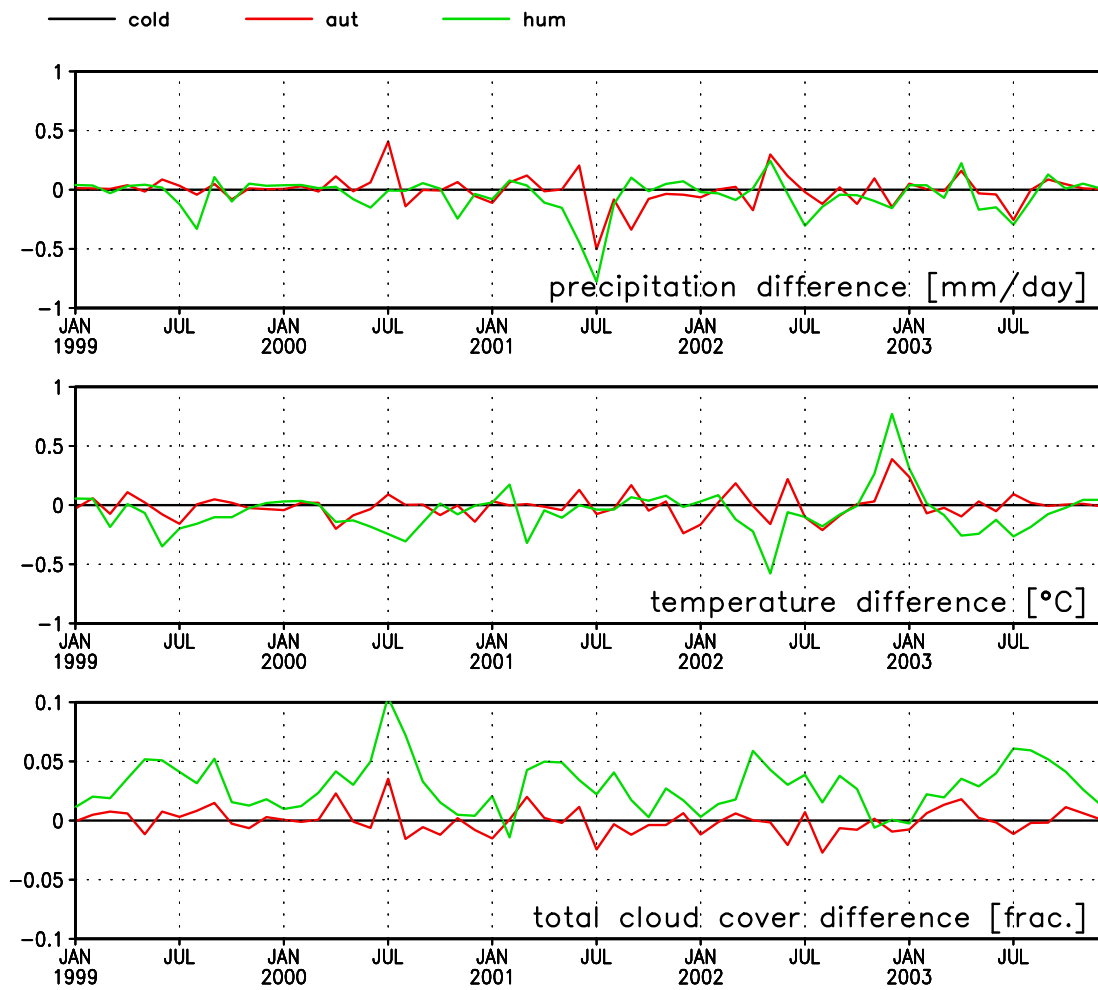


Figure 5.33: Change of the monthly mean values of precipitation, temperature and total cloud cover for $REMO_{aut}$ (red line) and $REMO_{hum}$ (green line) each in respect to the simulation with $REMO_{cold}$ (black line). Area of investigation is the Baltic Sea catchment.

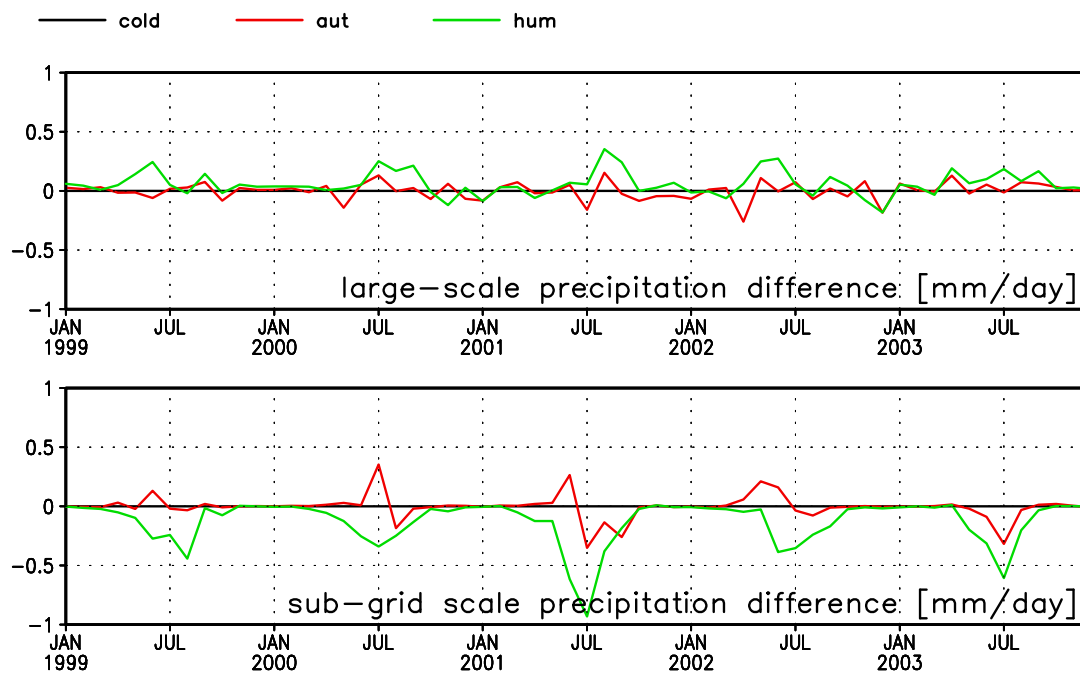


Figure 5.34: Change of the monthly mean values of the precipitation components, for $REMO_{aut}$ (red line) and $REMO_{hum}$ (green line) each with respect to the simulation with $REMO_{cold}$ (black line). Area of investigation is the Baltic Sea catchment.

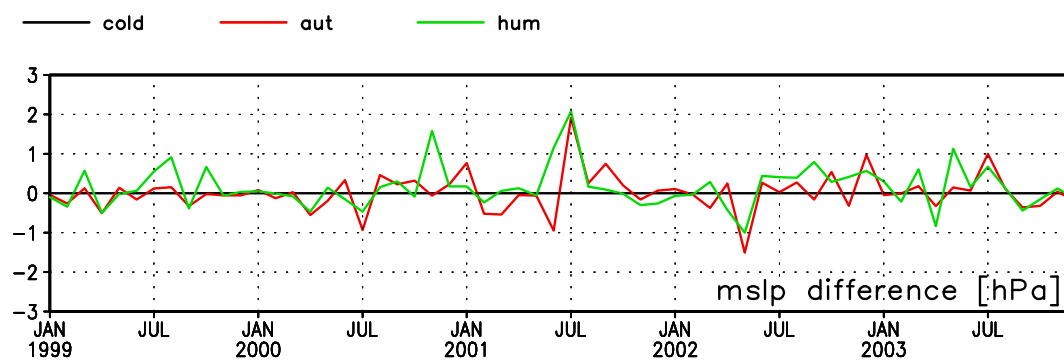


Figure 5.35: Change of the monthly mean values of mean sea level pressure for $REMO_{aut}$ (red line) and $REMO_{hum}$ (green line) each with respect to the simulation with $REMO_{cold}$ (black line). Area of investigation is the Baltic Sea catchment.

Critical relative humidity

The concept of critical relative humidity (CRH) was introduced in section 3.2.1. The profile of the critical relative humidity determines the onset of condensation and therefore cloud formation in a grid box. The choice of the relative humidity needed to allow cloud formation depends on the horizontal grid resolution of the model. The larger the grid boxes, the smaller the critical humidity can be chosen in order to make allowance for clouds occupying only part of the grid box. For this sensitivity study, the upper-atmosphere value for CRH has been reduced from 80% to now 70%. Both the profile used in *REMO_{standard}* and the profile used in this sensitivity study are shown in figure 5.36. The simulation with the reduced value of CRH will be addressed as *REMO_{hum}*.

The comparison of the results between *REMO_{hum}* and *REMO_{cold}* in figure 5.33

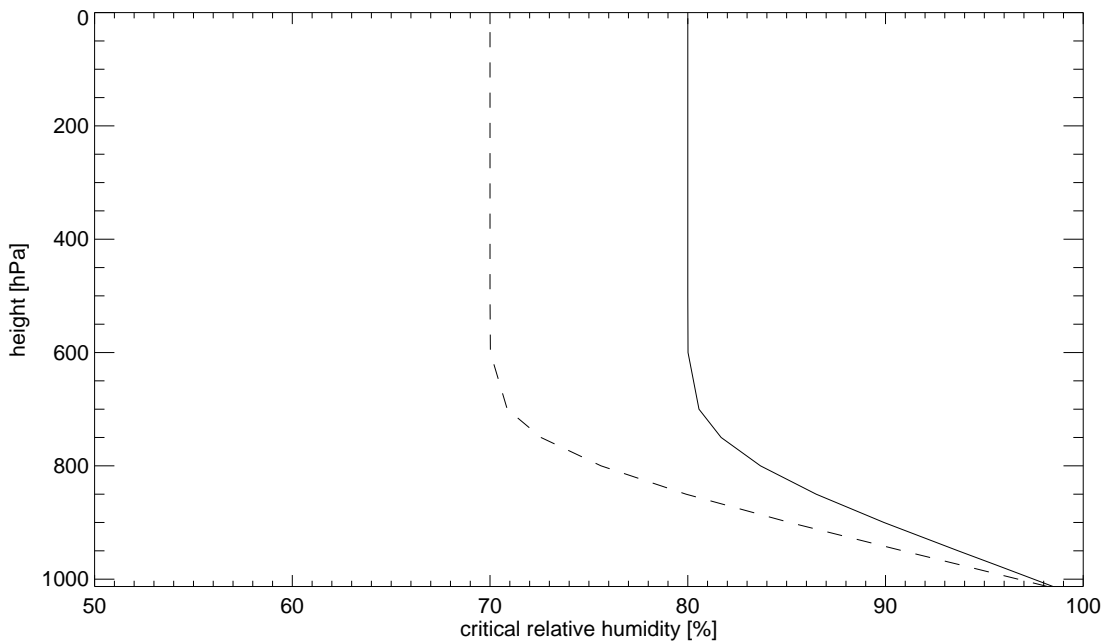


Figure 5.36: Profile of critical relative humidity for threshold values of 70% and 80%.

(green line) reveals a reduction of summer precipitation with *REMO_{hum}* for most of the summer months. The decreasing precipitation is dominated by a strong decrease of the convective component of the total precipitation. Figure 5.34 shows that the reduction of the threshold of CRH and therefore the earlier onset of large-scale

condensation only slightly increases the large-scale precipitation, whereas it visibly inhibits convective activity.

The decrease in summer precipitation with $REMO_{hum}$ is accompanied by a decrease in summer temperatures of up to $\frac{1}{2}^{\circ}$ C and an increase in cloudiness over the whole year with maximum increase in summer by around 5% (see figure 5.33). The changes in precipitation, temperature and cloud cover for $REMO_{hum}$ are more pronounced and seem to be more systematical as those deduced for the sensitivity study with $REMO_{aut}$ described in the previous section. The mean sea level pressure change, illustrated in figure 5.35 shows differences in the same order of magnitude as seen for the study with $REMO_{aut}$. Again, the MSLP differences could be attributed to the internal variability of the model.

Summarizing, the CRH seems to be an adequate parameter to reduce summer precipitation and to increase cloudiness. The use of a reduced value of 70% for $REMO_{cold}$ is therefore recommended for obtaining better results of simulated precipitation as well as cloud cover.

6 Conclusions

The objective of this work was the improvement of the simulation of clouds within the regional climate model REMO. Special focus has been given to the examination of processes connected to the ice phase of clouds. Changes have been applied to both the large-scale cloud scheme and to the sub-grid scale cloud scheme.

For the large-scale cloud scheme, a formulation for the prognostic treatment of cloud ice has been adopted from the global climate model ECHAM5 (Roeckner et al., 2003 [52]). The prognostic treatment of cloud ice allows for the inclusion of additional microphysical processes such as phase changes between liquid water and ice and the consideration of the *Bergeron-Findeisen* process in the microphysical cloud parameterization of the model. The former diagnosis of the cloud ice fraction, which was parameterized only in dependency of the grid mean temperature, has thus been replaced by a prognosis of the ice mixing ratio based on changes due to melting and evaporation of cloud ice, freezing of cloud water, sublimation of water vapor, sedimentation of ice crystals, accretion of ice crystals on snow and accretion of rain droplets on ice.

The sub-grid scale cloud scheme in REMO (the Tiedtke convection scheme (Tiedtke 1989, [68])) has been complemented by a 4th convection type, accounting for the properties of convection in cold air outbreaks connected to extratropical cyclones. For such cases, the original sub-grid scale cloud scheme in REMO decided for *shallow convection* as the driving force of the convection in this case is evaporation at the surface. The extended convection scheme now has the ability to separate between shallow convection in its primary sense (i.e. daytime convection over land or tradewind cumuli under a subsidence inversion) and convection, induced by strong surface fluxes of energy resulting from very cold air streaming over relatively warm surfaces. The second is also driven by surface evaporation, but is in its properties closer to penetrative convection than to shallow convection.

The modified cloud scheme has been applied to the case study of the North Atlantic

Cyclone *Caroline* and to two simulations of European climate from 1999 to 2003, one with $\frac{1}{2}^\circ$ horizontal grid resolution, the other with $\frac{1}{6}^\circ$ horizontal grid resolution. Main results for the cyclone *Caroline* are a higher percentage of postfrontal precipitation and therefore a better agreement of simulated precipitation rates to precipitation rates derived from SSMI/I satellite observations. For the European climate, the inclusion of the modified cloud microphysics resulted in slightly lower winter surface temperatures, less winter cloud cover, a reduction in winter precipitation and an increase in summer precipitation, accompanied by higher intensities of the convective component of the precipitation in summer. Additional changes are occurring in the simulation of cloud phase. The former diagnostic equation for cloud liquid and ice fraction used in *REMO_{standard}* produced, compared to observations as well as in comparison to diagnostic ice fractions used in other climate models, too much supercooled water at temperatures between -5°C and -25°C . With the new prognostic treatment of cloud ice, the ice fraction is simulated more realistically. The increase in summer precipitation led to a worsening in the simulated precipitation amounts with *REMO_{cold}* compared to *REMO_{standard}*, when comparing with precipitation observations from the *Global Precipitation Climatology Centre*. This can be reduced by imposing a lower value of the critical relative humidity, which controls the onset of condensation in the large-scale cloud scheme.

Considering the parameterization of clouds and cloud-associated processes in the regional climate model REMO, some general questions arose during this work, which should be briefly discussed in this section:

1. Is it possible to run one model with only one physical parameterization package on scales from 100 km down to 1 km horizontal resolution?

This question is important especially in the field of regional climate modeling, which indeed has to cope with the difficulty of a broad spectrum of resolutions. For REMO in its current state, the question can still be answered by *yes*, only because the finest resolutions are not (yet) possible. When advancing to a non-hydrostatic REMO version, this question has to be investigated in more detail. In this context, it should be examined whether it is possible to formulate all parameterizations independently of the model grid resolution or if grid resolution should be included as dependent variable.

2. Are the processes the same or should more physical processes be added when the resolution increases?

This question directly relates to the first question. Even if the processes could be formulated in an either grid-resolution-independent form or in a grid-resolution-incorporating form, is it then reasonable to consider all the same processes on all scales? Especially for the larger scales, including the integral impact of processes in a more statistical sense could be advantageous compared to including all the influences of small scale processes separately, thus allowing each process-formulation to bring in its uncertainties and (possible) tuning factors.

3. When should the separate convection parameterization be omitted?

In theory, the answer is: *for resolutions finer than approximately 2 km*. In practice, the question is if the existing cloud parameterizations in combination with the model dynamical scheme really are able to absorb the responsibilities of the convection parameterization, so that a pure on/off switch dependent from model resolution would be sufficient.

In this work those questions were touched at several occasions. The first question has on the one hand been addressed when comparing the simulations with $\frac{1}{2}^\circ$ and $\frac{1}{6}^\circ$ horizontal resolution, which resulted in a relatively coherent model-reaction to the changes in the model parameterizations, independent of model resolution. As mentioned above, this becomes more important when going to even smaller scales. On the other hand, question No. 1 has been discussed in the context of the *tuning* parameters that had been introduced in the global model ECHAM5, to adjust the small-scale based microphysical equations to the coarse resolution of the global model.

The second question has been dealt with when expanding the convection scheme to extratropical cold convection. Although it is not an additional process on the smaller scale, this type of convection obviously is not that important on the global scale. The question of scale-dependent processes here tends to be more a question of region-dependent processes, i.e. the transferability of physical parameterizations from one climatic zone to another. In an ideal model, which would cover all relevant physical processes and which would describe them in a physically perfect way, such

limitations do not exist. The physical principles underlying such a perfect model are globally valid. In reality, much of the model's parameterizations are unfortunately not perfect in the sense that simplifications and assumptions are incorporated. Many of those approximations to atmospheric processes are e.g. based on parameters derived from local measurement campaigns and are therefore biased to the climate of this specific region, which makes the transfer of the model to a different climatic region difficult.

Another part of this work, which strikes question No. 2 is the adoption of the cloud microphysical parameterizations from the global climate model ECHAM5. The question of the reasonability of including additional processes does not arise in cases those processes are explicitly needed, be it as model output parameter (e.g. the cloud droplet spectrum) or as essential processes for the coupling of the cloud scheme to other parts of the model (e.g. cloud-aerosol relation included via the formulation of precipitation processes).

The questions given above are also important in the context of global modeling approaches as e.g. ICON (ICOsahedral Non-hydrostatic General Circulation Model, developed by the Max Planck Institute for Meteorology in cooperation with the German Weather Service) or Arpège (an acronym for "Action de Recherche Petite Echelle Grande Echelle", i.e. "Research Project on Small and Large Scales", developed at Météo France), which have in common to simulate global climate with non-uniform grid resolutions. The concept of ICON is to include local refinement of the grid resolution, whereas Arpège uses a stretched grid, which has a resolution of approximately 50 km where it is best resolved. In the context of these approaches, the used model should be able to cope with varying grid scales, either with one single physical package or with the possibility to switch between different physical packages for different model resolutions.

7 Outlook

An important aspect of model development is model validation. Enabling the model to simulate as much physical processes as possible in an explicit way calls for the possibility of validating the model in terms of the single process simulation capability. If this is not possible, the validation of the integral effects of the parameterized processes (e.g. validation of the simulated precipitation to assess the quality of the cloud scheme) can be a first step of model validation. The improvement of the physical parameterizations based on such an *integral validation* becomes however difficult as the reasons of model deficiencies have to be identified in terms of the single physical processes that are parameterized. Generally, it has become quite evident in the last years that one of the key issues in cloud parameterization improvement is to bring together cloud modelers and the cloud observing community. This is especially true with cloud parameterizations including more and more processes explicitly. Even global climate models with coarse grid resolutions diagnose or calculate in their cloud schemes microphysical parameters as cloud phase, cloud droplet composition, cloud droplet size spectra, cloud optical thickness, etc. For the validation on the global scale, single extensive observational periods, delivering detailed observations but only for a few days and only for small regions are not sufficient. As discussed in section 5.3.1, a validation of cloud parameters and processes using satellite-derived observations available on longer time and space scales is highly desirable, but still only partially possible.

The modification of the convection scheme presented in this work is a kind of pragmatical solution to one of the problems arising in the context of convection parameterization in REMO. Although it is suitable for the application of the model in the mid-latitudes and although it - by definition - should not influence the simulation of convection in the tropics, the inclusion of a convection parameterization scheme following a different approach should be considered for the future. Especially in the context of regional climate modeling, the scale separation between the processes

simulated in the large-scale scheme and those related to the sub-grid scale scheme is a questionable approach (Kuo et al., 1997 [32], M. Bister, 1998 [7]). Although it is not yet possible to omit the convection scheme in REMO, as such fine resolutions are not applicable, an improvement would be to formulate the convection including the same prognostic variables as are used in the large-scale cloud scheme, e.g. cloud liquid water, cloud ice, etc. In this way, convective clouds formed in the convection scheme would be allowed to stay in the atmosphere for longer than a single timestep. The development of large-scale clouds initiated by and developing from convective activity would thus be simulated directly. The inclusion of cloud microphysics in the convection scheme currently is in work for the global climate model ECHAM. Doing the same for the regional climate model REMO should be considered.

Bibliography

- [1] **Albert, P., R. Bennartz, R. Preusker, R. Leinweber, J. Fischer, 2005:** Remote Sensing of Atmospheric Water Vapor using the Moderate Resolution Imaging Spectrometer. *Journal of Atmospheric and Oceanic Technology*, 22, 309-314.
- [2] **Arakawa, A., 1988:** Finite-Difference Methods in Climate Modeling. Proceedings of the NATO Advanced Study Institute on Physically-Based Modeling and Simulation of Climate and Climate Change (Part 1), Erice, Italy, 11-23 May 1986.
- [3] **Bauer, P., P. Schlüssel, 1993:** Rainfall, total water, ice water and water vapour over sea from polarized microwave simulations and Special Sensor Microwave/Imager data. *Journal of Geophysical Research*, 98 (D11), 20737-20759.
- [4] **Beheng, K.D., 1994:** A parameterization of warm cloud microphysical conversion processes. *Atmospheric Research*, 33, 193-206.
- [5] **Bigg, E.K., 1953:** The supercooling of water, *Proc. Phys. Soc. London*, vol 66, 688-694.
- [6] **Bigg, E.K., 1953:** The formation of atmospheric ice crystals by freezing of droplets. *Quart. J. Roy. Met. Soc.*, 79, 510-519.
- [7] **Bister, M., 1998:** Cumulus Parameterization in Regional Forecast Models: A Review. Hirlam Technical Report No. 35. Available at: <http://hirlam.knmi.nl/open/publications/TechReports/> (status May 2005).
- [8] **Bower, K.N., S.J. Moss, D.W. Johnson, T.W. Choullarton, J. Latham, P.R.A. Brown, A.M. Blyth, J. Cardwell, 1996:** A param-

- terization of the ice water content observed in frontal and convective clouds. *Quart. J. Roy. Met. Soc.*, 122, 1815-1844.
- [9] **Brenguier, J.-L., 2005:** Talk at the EGU General Assembly, Vienna 2005. Unpublished.
- [10] **Caya, D., S. Biner, 2004:** Internal variability of RCM simulations over an annual cycle. *Climate Dynamics*, 22, 33-46.
- [11] **CloudSat:** A NASA earthsystem science pathfinder mission. Information available at: <http://cloudsat.atmos.colostate.edu/> (status: January 2006)
- [12] **Cotton, W.R., G.J. Tripoli, R.M. Rauber, E.A. Mulvihill, 1986:** Numerical simulation of the effects of varying ice crystal nucleation rates and aggregation processes on orographic snowfall. *J. Climate Appl. Meteorology*, 25, 1658-1680.
- [13] **Davies, H.C., 1976:** A lateral boundary formulation for multi-level prediction models. *Quart. J. Roy. Met. Soc.*, 102, 403-418.
- [14] **DKRZ, 1994:** The ECHAM3 atmospheric general circulation model. Technical Report No.6.
- [15] **Global Energy and Watercycle Experiment (GEWEX):** GEWEX Cloud System Study (GCSS). <http://www.gewex.org/gcss.html> (status May 2005).
- [16] **Giorgi, F., L.O. Mearns, 1999:** Introduction to special section: Regional climate modeling revisited. *Journal of Geophysical Research*, 104 (D6), 6335-6352.
- [17] **Grabowski, W.W., 2001:** Coupling Cloud Processes with the Large-Scale Dynamics using the Cloud-Resolving Convection Parameterization (CRCP). *J. Atmos. Sci.*, 58, 978-997.
- [18] **Gregory, D., 1997:** The mass flux approach to the parameterization of deep convection. Meteorological Training Course Lectures Series, ECMWF, 2002. Available at http://www.ecmwf.int/newsevents/training/rcourse_notes/ (status May 2005).

-
- [19] **Gunn, K.L.S. and J.S. Marshall, 1958:** The distribution with size of aggregate snowflakes. *J. Meteor.*, 15, 452-651.
- [20] **Hagemann, S., B. Machenhauer, O.B. Christensen, M. Déqué, D. Jacob, R. Jones, P.L. Vidale, 2002:** Intercomparison of water and energy budgets simulated by regional climate models applied over Europe. Max-Planck-Institut für Meteorologie, Report No. 338.
- [21] **Hammarstrand, U., 1998:** Questions involving the use of traditional convection parameterization in NWP models with higher resolution. *Tellus*, 50a, 265-282.
- [22] **Heymsfield, A.J., 1977:** Precipitation development in stratiform ice clouds. A microphysical and dynamical study. *J. Atmos. Sci.*, 34, 367-381.
- [23] **Hogan, R.J., A.J. Illingworth, 2000:** Deriving cloud overlap statistics from radar. *Quart. J. Roy. Met. Soc.*, 126, October 2000 Part A, 2903-2909.
- [24] **The International Satellite Cloud Climatology Project (ISCCP)**
<http://isccp.giss.nasa.gov/ISCCP.html> (status May 2005).
- [25] **Jacob, D., 2001:** A note to the simulation of the annual and inter-annual variability of the water budget over the Baltic Sea drainage basin, *Meteor. Atm.*, 77, 61-73.
- [26] **Jacob, D., B.J.J.M. Van den Hurk, U. Andræ, G. Elgered, C. Fortelius, L.P. Graham, S.D. Jackson, U. Karstens, Chr. Köpken, R. Lindau, R. Podzun, B. Rockel, F. Rubel, B.H. Sass, R.N.B. Smith, X. Yang, 2001:** A comprehensive model inter-comparison study investigating the water budget during the BALTEX-PIDCAP period. *Meteorology and Atmospheric Physics*, 77, 19 - 43.
- [27] **Jacobson, M.Z., 1999:** *Fundamentals of Atmospheric Modeling*, Cambridge University Press, ISBN 0-521-63717-1, 656 pp.
- [28] **Jakob, C., 2002:** Cloud parametrization - Progress, Problems and Prospects. Proceedings of an ECMWF Seminar on Key Issues in Parametrization, ECMWF, November 2001, 327-338.

- [29] **Kershaw, R., D. Gregory, 1997:** Parameterization of momentum transport by convection. I: Theory and cloud modelling results. *Quart. J. Roy. Met. Soc.*, 123, 1133-1151.
- [30] **Keup-Thiel, E., Ch.-P. Klepp, E. Raschke, and B. Rockel, 2003:** Regional model simulation of the North Atlantic cyclone "Caroline" and comparison with satellite data, *Annales Geophysicae*, 21, 644-659.
- [31] **Klepp, Ch.-P., 2001:** Komponenten des Wasserkreislaufs in Zyklonen aus Satellitendaten - Niederschlagsfallstudien. PhD Thesis 82, Max-Planck-Institut für Meteorologie, Hamburg.
- [32] **Kuo, Y.-H., J.F. Bresch, M.-D. Cheng, J. Kain, D.B. Parsons, W.-K. Tao, D.-L. Zhang, 1997:** Summary of a mini workshop on cumulus parameterization for mesoscale models. *Bull. Amer. Soc.*, 78, 475-491.
- [33] **Krueger, S.K., 2000:** Cloud System Modeling. In: David A. Randall (Ed.), *General Circulation Model Development; Past, present, future* (pp. 605 - 640). Academic Press, International Geophysics Series, Vol 70.
- [34] **Leinweber, R., 2004:** Fernerkundung atmosphärischen Wasserdampfes für einen Vergleich mit dem regionalen Klimamodell REMO. Diploma thesis, Institut für Weltraumwissenschaften, *Freie Universität Berlin*.
- [35] **Levkov, L., B. Rockel, H. Kapitza, E. Raschke, 1992:** 3D Mesoscale Numerical Studies of Cirrus and Stratus Clouds by their time and space evolution. *Beitr. Phys. Atmosph.*, 65 (1), 35-58.
- [36] **Lohmann, U., E. Roeckner, 1995:** Introduction of a prognostic cloud ice scheme in the ECHAM general circulation model: Impact on climate and climate sensitivity. Max-Planck-Institut für Meteorologie, Report No. 179.
- [37] **Lin, Y.-L., R.D. Farley, H.D. Orville, 1983:** Bulk parameterization of the snow field in a cloud model. *J. Climate Appl. Meteor.*, 22, 1065-1092.
- [38] **Lin, J.W.-B., J.D. Neelin, 2002:** Considerations for stochastic convective parameterization, *J. Atmos. Sci.*, 59, 959-975.

- [39] **Molinari, J., M. Dudek, 1991:** Parameterization of Convective Precipitation in Mesoscale Numerical Models: A Critical Review. *Monthly Weather Review*, 120, 326-344.
- [40] **Morrissey, M.L., Y. Wang, 1995:** Verifying Satellite Microwave Rainfall Estimates over the Open Ocean. *Journal of Applied Meteorology*, 34, 794-804.
- [41] **Moss, S.J., D.W. Johnson, 1994:** Aircraft measurements to validate and improve numerical model parametrisations of ice to water ratios in clouds. *Atmos. Res.*, 34, 1-25.
- [42] **Müller, G., B. Brümmer, W. Alpers, 1999:** Roll Convection within an Arctic Cold-Air Outbreak: Interpretation of In Situ Aircraft Measurements and Spaceborne SAR Imagery by a Three-Dimensional Atmospheric Model. *Monthly Weather Review*, 127, 363-380.
- [43] **Murakami, M., 1990:** Numerical Modelling of microphysical and dynamical evolution of an isolated convective cloud – The 19 July 1981 CCOPE cloud. *J. Meteorol. Soc. Japan*, 68, 107-128.
- [44] **New, M., M. Hulme, P.D. Jones, 1999:** Representing twentieth century space-time climate variability. Part 1: development of a 1961-90 mean monthly terrestrial climatology. *Journal of Climate*, 12, 829-856.
- [45] **Nordeng, T.E., 1994:** Extended versions of the convective parametrization scheme at ECMWF and their impact on the mean and transient activity of the model in Tropics. ECMWF Tech. Memo. 206. Available from ECMWF, Shinfield Park, Reading, RG2 9AX, United Kingdom.
- [46] **Pincus, R., S.A. Klein, 2000:** Unresolved spatial variability and microphysical process rates in large-scale models. *Journal of Geophysical Research*, 105, 27059-27065.
- [47] **Pruppacher, H.R., J.D. Klett, 1997:** *Microphysics of Clouds and Precipitation*. Atmospheric & Oceanographic Sciences Library, ISBN 0-7923-4211-9. Kluwer Academic Publishers, Dordrecht, The Netherlands.

- [48] **Randall, D., M. Khairoutdinov, A. Arakawa, W. Grabowski, 2003:** Breaking the cloud parameterization deadlock, *Bull. Am. Meteorol. Soc.*, 84 (11), 1547-1564.
- [49] **Rasch, P.J., J.E. Kristjánsson, 1998:** A comparison of the CCM3 Model Climate Using Diagnosed and Predicted Condensate Parameterizations. *Journal of Climate*, 11 (7), 1587-1614.
- [50] **Rockel, B., E. Raschke, B. Weyres, 1991:** A parameterization of broad band radiative transfer properties of water, ice and mixed clouds. *Beitr. Phys. Atmos.*, 64, 1-12.
- [51] **Roeckner, E., K. Arpe, L. Bengtsson, M. Christoph, M. Claussen, L. Dümenil, M. Esch, U. Schlese, U. Schulzweida, 1996:** The atmospheric general circulation model ECHAM4: Model description and simulation of present-day climate. Max-Planck-Institut für Meteorologie, Report No. 218.
- [52] **Roeckner, E., G. Bäuml, L. Bonaventura, R. Brokopf, M. Esch, M. Giorgetta, S. Hagemann, I. Kirchner, L. Kornbluh, E. Manzini, A. Rhodin, U. Schlese, U. Schulzweida, A. Tompkins (2003):** The atmospheric general circulation model ECHAM 5. PART I: Model description. Max-Planck-Institut für Meteorologie, Report No. 349.
- [53] **Rogers, R.R., M.K. Yau, 1989:** *A Short Course in Cloud Physics* (3rd Edition). International Series in Natural Philosophy, Pergamon Press, Oxford, England. ISBN 0-08-034863-7, 304 pp.
- [54] **Rossow, W.B., A.W. Walker, L.C. Garder, 1993:** Comparison of ISCCP and other Cloud Amounts. *Journal of Climate*, 6 (12), 2394-2418.
- [55] **Rossow, W.B., R.A. Schiffer, 1999:** Advances in understanding clouds from ISCCP. *Bulletin of the American Meteorological Society*, 80, 2261-2287.
- [56] **Rotstajn, L.D., 1997:** A physically based scheme for the treatment of stratiform clouds and precipitation in large-scale models. I: Description and evaluation of the microphysical processes. *Quart. J. Roy. Met. Soc.*, 123, 1227-1282.

-
- [57] **Rotstajn, L.D., B.F. Ryand, J.J. Katzfey, 1999:** A scheme for Calculation of the Liquid Fraction in Mixed-Phase Stratiform Clouds in Large-Scale Models. *Mon. Wea. Review*, 128, 1070-1088.
- [58] **Rotstajn L.D., 2000:** On the "tuning" of autoconversion parameterizations in climate models, *Journal of Geophysical Research*, 105, 15495-15507.
- [59] **Rubel, F., M. Hantel, 2001:** BALTEX 1/6-degree daily precipitation climatology 1996-1998. *Meteorol. Atmos. Phys.*, 77, 155-166.
- [60] **Rudolf, B., T. Fuchs, U. Schneider, A. Meyer-Christoffer, 2003:** Introduction of the Global Precipitation Climatology Centre (GPCC), *Deutscher Wetterdienst, Offenbach a.M.*, pp. 16. Available at: <http://gpcc.dwd.de> (status August 2005).
- [61] **Schwarz, S.E., 1996:** Cloud droplet nucleation and its connection to aerosol properties. In: *Nucleation and Atmospheric Aerosols 1996. Proc. 14th Int. Conf. Nucleation and Atmospheric Aerosols (Helsinki, August 26-30, 1996)*, M. Kulmala and P.E. Wagner (Eds.), Elsevier Science, Ltd. Oxford, UK. pp 770-779.
- [62] **Smith, R.N.B., 1990:** A scheme for predicting layer clouds and their water content in a general circulation model. *Quart. J. Roy. Met. Soc.*, 116, 407-426.
- [63] **Sommerville, R.C.J., 2000:** Using single-column models to improve cloud-radiation Parameterizations. In: *David A. Randall (Ed.), General Circulation Model Development; Past, present, future (pp. 641 - 157)*. Academic Press, International Geophysics Series, Vol 70.
- [64] **Stickley, A.R., 1940:** An Evaluation of the Bergeron-Findeisen Precipitation Theory. *Mon. Wea. Rev.*, October 1940, 272-280.
- [65] **von Storch, H., S. Güss, M. Heimann, 1999:** *Das Klimasystem und seine Modellierung, Eine Einführung*. ISBN 3-540-65830-0, Springer Verlag Berlin Heidelberg New York. 255 pp.
- [66] **Sundqvist, H., 1978:** A parameterization scheme for non-convective condensation including prediction of cloud water content. *Quart. J. Met. Soc.*, 104, 677-690.

-
- [67] **Sundqvist, H., E. Berge, J.E. Kristjansson, 1989:** Condensation and cloud parameterization studies with a mesoscale numerical weather prediction model. *Mon. Wea. Rev.*, 177, 1641-1657.
- [68] **Tiedtke, M., 1989:** A comprehensive mass flux scheme for cumulus parametrisation in large-scale models. *Mon. Wea. Rev.*, 117, 1779-1800.
- [69] **Tiedtke, M., 1993:** Representation of Clouds in Large-Scale Models. *Mon. Wea. Rev.*, 121, 3040-3061.
- [70] **Undén, P., L. Rontu, H. Jarvinen, P. Lynch (Eds.), 2002:** HIRLAM-5 Scientific Documentation. Available from SMHI, S-601 Norrköping, Sweden.
- [71] **Wood, R., P.R. Field, W.R. Cotton, 2002:** Autoconversion rate bias in stratiform boundary layer cloud parameterizations. *Atmospheric Research*, 65, 109-128.

List of Abbreviations

Γ	Gamma function
$\langle P \rangle$	rain flux density at top of a cloud layer
ρ_0	reference density of air = $1.3 \frac{kg}{m^3}$
ρ_{air}	air density
ρ_{H_2O}	density of water = $1000 \frac{kg}{m^3}$
ρ_s	bulk density of snow = $100 \frac{kg}{m^3}$
d_{ar}	aerosol diffusivity = $1,4 \cdot 10^{-8} \frac{m^2}{s}$
D_s	Diameter of a snow particle
E_{ii}	collection efficiency between ice crystals = 0.1
E_{si}	collection efficiency of snow for cloud ice
E_{sl}	collection efficiency of snow for cloud droplets = 1
f_{ice}	diagnostic ice fraction
f_{liq}	diagnostic liquid water fraction
g	acceleration of gravity
G_p	precipitation rate for convective precipitation
M_d	convective downward mass flux
m_{io}	initial mass of a nucleated ice crystal = $10^{-12} kg$
$M_{u,base}$	convective upward mass flux at cloud base
M_u	convective upward mass flux
N_l	cloud droplet number concentration
q_{ci}	cloud ice
q_{cl}	cloud liquid water
q_c	total cloud water
r_{ei}	mean effective ice crystal radius
r_{s0}	smallest radius of a particle in the category <i>snow</i> = $10^{-4} m$
r_{snow}	mass mixing ratio of snow

r_{vi}	mean volume ice crystal radius
rad_i	mean volume cloud droplet radius
T_0	freezing point temperature
v_t	terminal velocity of ice crystals
X	dispersion of the fall velocity spectrum of cloud ice = 0.25
CAPE	Convective Available Potential Energy
CC	Cloud Cover (3-d)
CRU	Climate Research Unit
ECMWF	European Centre of Medium-Range Weather Forecasts
GPCC	Global Precipitation Climatology Centre
IWV	Integrated Water Vapor
MSLP	Mean Sea Level Pressure
SSM/I	Special Sensor Microwave/Imager
TCC	Total Cloud Cover (2-d)

Acknowledgments

I would like to thank my supervisor Dr. Daniela Jacob for offering me the opportunity to work on this topic and Prof. Dr. Graßl for agreeing to be second supervisor. I am also very grateful to Prof. Dr. Fischer, who accepted me to his working group, at the *Institut für Weltraumwissenschaften* at the *Freie Universität Berlin*. This cooperation greatly enhanced my insight in remote sensing techniques and in the possibilities and restrictions of the use of satellite data for model validation.

I would like to express special thanks to my colleagues at the Max Planck Institute in Hamburg and also to my colleagues at the *Institut für Weltraumwissenschaften* in Berlin for the excellent working climate, for fruitful discussions and for relieving and motivating work breaks.

Special thanks go to Philip Lorenz, who was always prepared to discuss arising questions and who gave me innumerable thought-provoking impulses to improve this work.

Many thanks go to my sister Sabine Pfeifer for the language correction.

I am also grateful to Dr. Svitlana Krakovska for having a look at the cloud-modeling chapters as well as to my friends Caroline Hoffmann and Florian Bartsch for the proofreading of selected chapters.

My sister Sabine Pfeifer as well as my friends Ralf Diener, Sandra Henne and Thorsten Busse made me feel at home in Hamburg by leaving to me their living room sofas for countless stays in Hamburg. Thanks for that.

Many thanks go to Max Reuter for scientific and programming support and for all the rest.

Last but not least, I would like to thank my parents Gudrun and Werner Pfeifer who always supported me in every possible way.

MPI-Examensarbeit-Referenz:

Examensarbeit Nr. 1-82 bei Bedarf bitte anfragen:
MPI für Meteorologie, Abtlg.: PR, Bundesstr. 53, 20146 Hamburg

MPI-Report-Referenz:

MPI-Report Nr. 1-351 bei Bedarf bitte anfragen:
MPI für Meteorologie, Abtlg.: PR, Bundesstr. 53, 20146 Hamburg

Beginn einer neuen Veröffentlichungsreihe des MPIM, welche die vorherigen Reihen "Reports" und "Examensarbeiten" weiterführt:

**„Berichte zur Erdsystemforschung“ , „*Reports on Earth System Science*“, ISSN 1614-1199
Sie enthält wissenschaftliche und technische Beiträge, inklusive Dissertationen.**

Berichte zur Erdsystemforschung Nr.1 Juli 2004	Simulation of Low-Frequency Climate Variability in the North Atlantic Ocean and the Arctic Helmuth Haak
Berichte zur Erdsystemforschung Nr.2 Juli 2004	Satellitenfernerkundung des Emissionsvermögens von Landoberflächen im Mikrowellenbereich Claudia Wunram
Berichte zur Erdsystemforschung Nr.3 Juli 2004	A Multi-Actor Dynamic Integrated Assessment Model (MADIAM) Michael Weber
Berichte zur Erdsystemforschung Nr.4 November 2004	The Impact of International Greenhouse Gas Emissions Reduction on Indonesia Armi Susandi
Berichte zur Erdsystemforschung Nr.5 Januar 2005	Proceedings of the first HyCARE meeting, Hamburg, 16-17 December 2004 Edited by Martin G. Schultz
Berichte zur Erdsystemforschung Nr.6 Januar 2005	Mechanisms and Predictability of North Atlantic - European Climate Holger Pohlmann
Berichte zur Erdsystemforschung Nr.7 November 2004	Interannual and Decadal Variability in the Air-Sea Exchange of CO₂ - a Model Study Patrick Wetzel
Berichte zur Erdsystemforschung Nr.8 Dezember 2004	Interannual Climate Variability in the Tropical Indian Ocean: A Study with a Hierarchy of Coupled General Circulation Models Astrid Baquero Bernal
Berichte zur Erdsystemforschung Nr.9 Februar 2005	Towards the Assessment of the Aerosol Radiative Effects, A Global Modelling Approach Philip Stier
Berichte zur Erdsystemforschung Nr.10 März 2005	Validation of the hydrological cycle of ERA40 Stefan Hagemann, Klaus Arpe and Lennart Bengtsson
Berichte zur Erdsystemforschung Nr.11 Februar 2005	Tropical Pacific/Atlantic Climate Variability and the Subtropical-Tropical Cells Katja Lohmann
Berichte zur Erdsystemforschung Nr.12 Juli 2005	Sea Ice Export through Fram Strait: Variability and Interactions with Climate- Torben Königk
Berichte zur Erdsystemforschung Nr.13 August 2005	Global oceanic heat and fresh water forcing datasets based on ERA-40 and ERA-15 Frank Röske

MPI-Examensarbeit-Referenz:

Examensarbeit Nr. 1-82 bei Bedarf bitte anfragen:
MPI für Meteorologie, Abtlg.: PR, Bundesstr. 53, 20146 Hamburg

MPI-Report-Referenz:

MPI-Report Nr. 1-351 bei Bedarf bitte anfragen:
MPI für Meteorologie, Abtlg.: PR, Bundesstr. 53, 20146 Hamburg

**Berichte zur
Erdsystemforschung Nr.14**
August 2005

**The Hamburg Ocean Carbon Cycle Model
HAMOCC5.1 - Technical Description Release 1.1**
Ernst Maier-Reimer, Iris Kriest, Joachim Segsneider,
Patrick Wetzel

**Berichte zur
Erdsystemforschung Nr.15**
Juli 2005

**Long-range Atmospheric Transport and Total
Environmental Fate of Persistent Organic Pollutants
- A Study using a General Circulation Model**
Semeena Valiyaveetil Shamsudheen

**Berichte zur
Erdsystemforschung Nr.16**
Oktober 2005

**Aerosol Indirect Effect in the Thermal Spectral
Range as Seen from Satellites**
Abhay Devasthale

**Berichte zur
Erdsystemforschung Nr.17**
Dezember 2005

**Interactions between Climate and Land Cover
Changes**
Xuefeng Cui

**Berichte zur
Erdsystemforschung Nr.18**
Januar 2006

**Rauchpartikel in der Atmosphäre: Modellstudien am
Beispiel indonesischer Brände**
Bärbel Langmann

**Berichte zur
Erdsystemforschung Nr.19**
Februar 2006

**DMS cycle in the ocean-atmosphere system and its
response to anthropogenic perturbations**
Silvia Kloster

**Berichte zur
Erdsystemforschung Nr.20**
Februar 2006

Held-Suarez Test with ECHAM5
Hui Wan, Marco A. Giorgetta, Luca Bonaventura

**Berichte zur
Erdsystemforschung Nr.21**
Februar 2006

**Assessing the Agricultural System and the Carbon
Cycle under Climate Change in Europe using a
Dynamic Global Vegetation Model**
Luca Criscuolo

**Berichte zur
Erdsystemforschung Nr.22**
März 2006

**More accurate areal precipitation over land and sea,
APOLAS Abschlussbericht**
K. Bumke, M. Clemens, H. Graßl, S. Pang, G. Peters,
J.E.E. Seltmann, T. Siebenborn, A. Wagner

